GENERATION AND EVALUATION OF DEMs DERIVED BY TERRASAR-X INSAR IMAGES

Umut Güneş SEFERCİK

Zonguldak Karaelmas University
Graduate School of Natural and Applied Sciences
Department of Geodesy and Photogrammetry Engineering
Ph.D Thesis

ZONGULDAK
June 2010

KABUL

Umut Güneş SEFERCİK tarafından hazırlanan "GENERATION AND EVALUATION OF DEMs DERIVED BY TERRASAR-X INSAR IMAGES" başlıklı bu çalışma jürimiz tarafından değerlendirilerek, Zonguldak Karaelmas Üniversitesi (ZKÜ) Fen Bilimleri Enstitüsü Jeodezi ve Fotogrametri Mühendisliği Anabilim Dalında Doktora Tezi olarak oybirliğiyle kabul edilmiştir. 14/06/2010

Başkan: Prof. Dr. Şenol KUŞÇU (ZKÜ) ....

Üye : Prof. Dr. Derya MAKTAV (İTÜ) ....

Üye : Doç. Dr. Naci YASTIKLI (YTÜ) ....

Üye : Doç. Dr. Yılmaz YILDIRIM (ZKÜ) ....

Üye : Yrd. Doç. Dr. Mehmet ALKAN (ZKÜ) ....

ONAY:

Yukarıdaki imzaların, adı geçen öğretim üyelerine ait olduğunu onaylarım. 15./.6../2010

Prof. Dr. Kemal BÜYÜKGÜZEL
Fen Bilimleri Enstitüsü Müdürü

"I assure that the present work was written independently and I have not used other than the stated sources and aids."

Umut Güneş SEFERCİK

ABSTRACT

Ph.D Thesis

GENERATION AND EVALUATION OF DEMs DERIVED BY TERRASAR-X INSAR IMAGES

Umut Güneş SEFERCİK

Zonguldak Karaelmas University
Graduate School of Natural and Applied Sciences
Department of Geodesy and Photogrammetry Engineering

Thesis Supervisor: Prof. Dr. Şenol KUŞÇU
June 2010, 175 pages

A Digital Elevation Model (DEM) is the digital cartographic representation of the elevation of the terrain at regularly spaced intervals in X and Y directions, using Z-values related to a common vertical datum. DEMs are required for several applications and in order to satisfy the need, various DEM generation techniques have been developed up to now. Remote sensing is one of those techniques and contains two main methods for DEM generation: optical imagery and interferometric synthetic aperture radar (InSAR). These methods have several advantages and disadvantages against each other. For example, object recognition is easier in optical imagery but it depends on weather conditions. On the other side, in contrast to optical imagery, object recognition is poor in InSAR but data collection is independent from weather conditions, clouds can be penetrated and cloudless large coverage up to global can be obtained at specific short times.

In the study, the comparison of high resolution InSAR and optical DSMs was aimed at the common test field to determine the quality of TerraSAR-X (TSX) data which is one of the

ABSTRACT (continued)

most advanced Synthetic Aperture Radar (SAR) satellites. TSX is German made and launched on June 15th, 2007. It offers high resolution (~1m by Spotlight mode) imagery which could not been achieved from radar technologies up to this time similar to high resolution optical imagery. In contrast to optical sensors, it can be operated under all weather conditions without being influenced by clouds and imaging can be possible in single, dual and quad-polarization. The data sets provided by TSX newly obtained by scientific community and evaluations are currently being performed.

According to the aims of the study, high resolution spotlight (HRS) and stripmap modes of TSX DSMs were generated sequentially with 3m and 10m grid intervals for two test fields in Istanbul, Turkey and evaluated using more accurate (10cm up to 1m) reference DEMs, generated by photogrammetry. In contrast to DEMs, DSMs do not determine a bare topography and describe a surface which passes over the top of ground objects like buildings, vegetation, forest etc. And it is not exactly possible to filter these models into bare ground in a healthy way. Therefore, the evaluated DSMs have not been reduced into DEMs. Only the blunders have been eliminated applying smoothing filters. Besides, all evaluated models are DSMs in the study and this situation causes an advantage for direct comparison of their analyse results against reference DEMs. For the comparison with TSX models, SRTM, IKONOS, SPOT and ASTER DEMs were obtained and evaluated on the common test fields. At the evaluation of the models, the absolute and relative accuracies were determined, frequency distributions of Z-differences and dependency up on the aspects (deal with ascending and descending orbits) were identified, influence of interpolation analysis and morphologic detail analysis were performed and the differential DEMs (DIFFDEMs) and shadings were generated to assess the qualities by visualization.

Keywords: TerraSAR-X (TSX), Interferometric Synthetic Aperture Radar (InSAR), Digital Elevation Model (DEM), Quality Assessment, Accuracy

Science Code: 616.02.04

ÖZET

Doktora Tezi

TERRASAR-X INSAR GÖRÜNTÜLERİNDEN SAYISAL YÜKSEKLİK MODELLERİNİN ÜRETİLMESİ VE DEĞERLENDİRİLMESİ

Umut Güneş SEFERCİK

Zonguldak Karaelmas Üniversitesi
Fen Bilimleri Enstitüsü
Jeodezi ve Fotogrametri Mühendisliği Anabilim Dalı

Tez Danışmanı: Prof. Dr. Şenol KUŞÇU
Haziran 2010, 175 sayfa

Dijital Yükseklik Modeli (DYM) ortak bir düşey datumla ilişkili Z değerlerini kullanarak X ve Y yönlerinde düzenli aralıklarda arazi yüksekliğinin sayısal kartoğrafik bir temsilidir. DYM'lere bir çok uygulama için ihtiyaç duyulmaktadır ve bu ihtiyacın karşılanması için bugüne dek çeşitli DYM yaratım teknikleri geliştirilmiştir. Uzaktan algılama bu tekniklerden birisidir ve DYM üretimi için optik görüntüleme ve interferometrik yapay açıklıklı radar (InSAR) olmak üzere iki ana metot içermektedir. Bu metotlar birbirlerine kıyasla bir çok avantaj ve dezavantajlara sahiptir. Örneğin, obje tanıma optik görüntüleme ile daha kolaydır fakat bu durum hava koşullarının elverişli oluşuna bağlıdır. Diğer yandan, optik görüntülemenin tersine InSAR'da obje tanıma zayıftır fakat veri toplama hava şartlarından bağımsızdır, bulutlar ayırt edilebilir ve bulutsuz global ölçeğe dek geniş kaplama alanı spesifik kısa zamanlarda elde edilebilir.

Bu çalışmada, en gelişmiş yapay açıklıklı radar uydularından biri olan TerraSAR-X (TSX)'in veri kalitesinin belirlenmesi için ortak test alanlarında yüksek çözünürlüklü InSAR ve optik

ÖZET (devam ediyor)

Dijital Yüzey Modellerinin karşılaştırılması amaçlanmıştır. TSX Alman yapımı olup 15 Haziran 2007 tarihinde fırlatılmıştır. Uydu, yüksek çözünürlüklü optik görüntülemeye benzer olarak bu güne dek radar teknolojilerinden elde edilememiş düzeyde yüksek çözünürlük (~1m, Spotlight mod) sunmaktadır. Optik sensörlerin aksine, bulutlardan etkilenmeksizin tüm hava şartlarında işletilebilir ve görüntüleme tek, çift ve dörtlü polarizasyonlarla yapılabilir. TSX tarafından sağlanan veri setleri bilim camiası tarafından yeni elde edilmektedir ve değerlendirmeler şuan itibariyle gerçekleştirilmektedir.

Çalışmanın amaçları doğrultusunda, yüksek çözünürlüklü spotlight (HRS) ve stripmap mode TSX Dijital Yüzey Modelleri, İstanbul, Türkiye'de iki test alanında sırasıyla 3m ve 10m grid aralıklarında üretilmiş ve fotogrametrik yöntemle elde edilmiş daha yüksek doğrulukta (10cm-1m) referans DYM'ler kullanılarak değerlendirilmiştir. Dijital Yüzey Modelleri, DYM'lerden farklı olarak çıplak yeryüzünü değil, bina, bitki örtüsü, orman gibi objelerin üstünden geçen bir yüzeyi tanımlamaktadır. Bu modellerin sağlıklı şekilde filtrelenerek çıplak yeryüzüne indirgenmesi tam olarak mümkün değildir. Bu nedenle değerlendirilen Dijital Yüzey Modelleri, DYM'lere indirgenmemiştir. Yalnızca bir takım yumuşaklaştırıcı filtrelemeler uygulanarak kaba noktalar elemine edilmiştir. Ayrıca çalışmada kullanılan yöntem kıyaslama olduğundan değerlendirilen tüm modellerin Dijital Yüzey Modeli olması da referans DYM'lerle yapılan analiz sonuçlarının direkt olarak karşılaştırılabilmesi açısından bir avantaj oluşturmuştur. Çalışmada, TSX modelleri ile karşılaştırma yapmak için SRTM, IKONOS, SPOT ve ASTER Dijital Yüzey Modelleri ortak test alanlarında elde edilmiş ve değerlendirilmiştir. Modellerin değerlendirilmesinde, kesin ve relatif doğruluklar belirlenmiş, Z farklarının frekans dağılımları ve yöne (yükseliş ve alçalış yörüngelerine bağlı) bağımlılıklar tanımlanmış, enterpolasyon etki analizleri ve morfolojik detay analizleri gerçekleştirilmiş ve görselleştirmeyle kalite değerlendirme yapmak amacıyla fark yükseklik modelleri (DIFFDEMs) ve gölge görünümler yaratılmıştır.

Anahtar Sözcükler: TerraSAR-X (TSX), İnterferometrik Yapay Açıklıklı Radar (InSAR), Dijital Yükseklik Modeli (DYM), Kalite Değerlendirmesi, Doğruluk

Bilim Kodu: 616.02.04

ACKNOWLEDGEMENTS

I would like to thank Prof. Dr. –Ing. Uwe Sörgel, Dr. –Ing. Karsten Jacobsen, Dr. –Ing. Peter Lohmann, Dipl. -Ing. Abdalla Alobeid, Dipl. -Ing. Alexander Schnuert, Dipl. -Ing. Jan Dirk Wegner and Dipl. -Ing. Uwe Bolte from the Institute of Photogrammetry and Geoinformation (IPI), Leibniz University Hannover, Germany, Prof. Dr. Şenol Kuşçu, Assoc. Prof. Dr. Yılmaz Yıldırım and Assoc. Prof. Dr. Mehmet Alkan from the Department of Geodesy and Photogrammetry Engineering and Deparment of Environmental Engineering, Faculty of Engineering, Zonguldak Karaelmas University, Prof. Dr. Derya Maktav from the Department of Geomatic Engineering, Istanbul Technical University and Assoc. Prof. Dr. Naci Yastıklı from the Department of Map Engineering, Yıldız Technical University, Istanbul, Turkey for their supports and advices. And also I would like to thank Turkish Scientific and Technical Research Institute (TÜBİTAK) for the financial support of this study by Oversea Research Scholarship Programme.

CONTENTS

CONTENTS (continued)

CONTENTS (continued)

Page

CONTENTS (continued)

LIST OF FIGURES

LIST OF FIGURES (continued)

LIST OF FIGURES (continued)

No Page

LIST OF FIGURES (continued)

LIST OF FIGURES (continued)

LIST OF FIGURES (continued)

LIST OF FIGURES (continued)

LIST OF TABLES

LIST OF TABLES (continued)

LIST OF TABLES (continued)

LIST OF APPENDICES

SYMBOLS AND ACRONYMS

λ : Wavelength

B : Antenna beam

AL : Antenna length

GHz : Giga hertz = 1000 mega hertz

F : Frequency

m : Meter

cm : Centimeter

H : Altitude

B : Baseline

θ : View angle

ξ : Baseline declination

$\Delta\varphi$: Phase difference

π : Pi number ~ 3.1416

R_1, r_2 : Slope distances between target point and SAR antennas

° : Degree

arcsecond : Nearly 30 meters (1/60 arcminute)

km : Kilometer

SZ : Accuracy

A : Slope

% : Percent

Nm : Nanometer

Rg : Range

SYMBOLS AND ACRONYMS (continued)

Az : Azimuth

Bit : Binary digit

T : Time

Hz : Hertz

pixel : Picture element (it is a single point in a raster image)

fringe : 2π cycle

f_D : Doppler centroid difference (processed doppler frequency)

γ : Coherence

s_M, s_S : Coregistered master and slave images

w_k, w_h : Estimate of local slopes

$H(u,v)$: Filter response (the spectrum of the filtered interferogram)

$S\{\}$: Smoothing operator

u, v : Spatial frequencies

A : Filter parameter

Ψ : Wrapped phase or principal interferometric phase ($-\pi \leq \Psi < +\pi$)

Φ : Unwrapped phase or full cycle interferometric phase

k : 0,......, n

h : Ellipsoidal height

H : Orthometric height

N : Geoidal height (undulation)

C : Geopotential number

W , W_0 : Potentials of gravity of a point and the geoid

G : Gravity

d_n : levelling increment

SYMBOLS AND ACRONYMS (continued)

R_s : Slant range

S, P : Spacecraft and backscatter element position

v_p, v_s : Spacecraft and backscatter element velocity

f_0 : Carrier frequency

c : Speed of light

ΔD : Horizontal shift

ΔZ, DZ : Height difference

p : Point

P : Factor for single or repeat-pass InSAR

SZ : Standard deviation of Z

d : Distance between points

dl : Lower distance limit

Du : Upper distance limit of the distance

R : Distance between antenna and object

Res_{range} : Range resolution

$Res_{azimuth}$: Azimuth resolution

Bs : Synthetic beamwidth

ΔLs : Azimuth resolution

ϕ : Off-nadir angle

ΔX, ΔY : Coordinate differences in X and Y directions

ACRONYMS

AATSR : Advanced along track scanning radiometer

ALOS : Advanced Land Observing Satellite

AMI : Active Microwave Instrument

SYMBOLS AND ACRONYMS (continued)

ASAR	: Advanced Synthetic Aperture Radar
ASCII	: American standard code for information interchange
ASI	: Italian Space Agency
ASTER	: Advanced spaceborne thermal emission and reflection radiometer
ATSR	: Along Track Scanning Radiometer
AVNIR-II	: Advanced visible and near infrared radiometer- type two
BLUH	: Bundle block adjustment Leibniz University Hannover
BMBF	: German ministry of education and science
CCD	: Charge coupled device
CE90	: Circular Error of 90%
CSA	: Canadian Space Agency
CT	: Coherence threshold
CTS	: Conventional terrestrial system
DEM	: Digital Elevation Model
DHM	: Digital Height Model
DIFFDEM	: Differential DEM
DLR	: German Aerospace Center
DORIS	: Doppler orbitography and radio-positioning integrated by satellite
DSM	: Digital Surface Model
DTM	: Digital Terrain Model
ENVISAT	: Environmental Satellite
ERS	: Europen Remote Sensing satellite
ESA	: European Space Agency
GCP	: Ground control point
Geocoding	: Geographic coding

SYMBOLS AND ACRONYMS (continued)

GIS	: Geographical information system
GOME	: Global Ozone Measuring Equipment
GOMOS	: Global ozone monitoring by occultation of stars
GPF	: Gravity Re-Packed File
GPS	: Global positioning system
GSD	: Ground sampling distance
h/b	: Height-to-base
HH	: Horizontal horizontal
HP/GL	: Hewlett-Packard Graphics Language (printer control language)
HRG	: High resolution geometric
HRS	: High resolution stereo
HV	: Horizontal vertical
Id	: Identification
IKONOS	: Image (in Greece Mythology)
IMU	: Inertial measurement units
INS	: Inertial navigation system
InSAR	: Interferometric synthetic aperture radar
IPI	: Institute of Photogrammetry and GeoInformation
ITT VIS	: International Telephone & Telegraph Visual Information Solutions
JAROS	: Japan Resources Observation System Organization
JAXA	: Japan Aerospace Exploration Agency
JERS	: Japanese Earth Resources Satellite
JST	: Japan Science and Technology Agency
LE90	: Linear Error of 90%
LED	: Light emitting diode

SYMBOLS AND ACRONYMS (continued)

LIDAR : Light detection and ranging

LPDAAC : Land Processes Distributed Active Archive Center

LRR : Laser Retro-Reflector

MDA : Macdonald, Dettwiler and Associates Ltd.

MERIS : Medium-spectral Resolution Imaging Spectrometer Insturement

MIPAS : Michelson interferometer for passive atmospheric sounding

MITI : Ministry of International Trade and Industry

MS : Multispectral

MTP : Microwave Temperature Profiler

MWR : Microwave radiometer

NAP : Not accepted point

NASA : American National Aeronautics Space Administration

NASDA : Japanese National Space Development Agency

NIMA : National Imagery and Mapping Agency

NIR : Near infrared

NOAA : National Oceanic and Atmospheric Administration

OPS : Optical Sensors

PALSAR : Phased array type L-band synthetic aperture radar

PAN : Panchromatic

PFR : Pulse repetition frequency

PPI : Plan position indicator

PPP : Public private partnership

PRISM : Panchromatic remote sensing instrument for stereo mapping

PRARE : Precise Range and Range-rate Equipment

RA : Radar altimeter

SYMBOLS AND ACRONYMS (continued)

RADAR : Radio detection and ranging

RAR : Real aperture radar

RA-2 : Radar altimeter 2

REFDEM : Reference DEM

RMS : Root mean square

RMSE : Root mean square error

RMSZ : Root mean square of height (Z-component)

RSX : Relative standard deviation

RTK : Real time kinematic

SAR : Synthetic aperture radar

SRTM : Shuttle Radar Topography Mission

SCIAMACHY : SCanning Imaging Absorption spectroMeter for Atmospheric CartograpHY

SLR : Satellite Laser Ranging

SLR : Side looking radar

.SML : Simplified Markup Language

SNR : Signal to noise ratio

SPOT : Satellite Pour l'Observation de la Terre

SWIR : Short wave infrared

TSX : TerraSAR-X

TSX SL : TerraSAR-X Spotlight mode

TSX SM : TerraSAR-X Stripmap mode

UK : United Kingdom

USA : United States of America

USGS : U.S. Geological Survey

UTM : Universal transverse Mercator

SYMBOLS AND ACRONYMS (continued)

VNIR : Visible near infrared

VV : Vertical vertical

WS : Wind scatterometer

.XML : Extensible Markup Language

2D : Two dimensional (planimetric)

3D : Three dimensional

PART 1

INTRODUCTION

1.1 MOTIVATION

As well known, currently, the remote sensing technologies make progress with high acceleration and improve permanently. Annually new satellites are launched into space containing different types of operation principles and data collection configurations. They provide and present actual information about Earth to the users from several kinds of occupation groups of different disciplines. The remote sensing satellites and corresponding imaging systems can be separated into two main groups: optical satellites with optical sensors and radar satellites with radar sensors. The operation principle of optical imagery is; filling the image pixels according to reflection values from the ground objects in specific intervals of electromagnetic spectrum (visible and near-infrared) by means of CCD (charge-coupled device) sensors hereby generating digital images. Some high and very high resolution optical satellites are; GeoEye-1 (40cm GSD), WorldView-1 (50cm GSD), Quickbird (60cm GSD), IKONOS (1m GSD), OrbView-3 (1m GSD), Spot (5m GSD) and ASTER (15m GSD). As distinct from the optical imagery, logic of radar imagery can be summarized as; transmitting and receiving microwave signals to the interest area using interior transmitter and receiver antennas; thus recording the reflections from ground objects at the field of view and determining the distance of these objects to the system.

The radar systems consist of three main groups with respect to their application. These are; Doppler radar which is especially constructed for detecting the velocity of objects, Plan Position Indicator (PPI) radar generates the permanent actual displays of the objects which turn around its spinning antenna and Side Looking radar (SLR). However, Doppler and PPI radars are not used in most of the remote sensing applications because of their coarser spatial resolution. The preferred radar systems in remote sensing are SLR systems. SLR systems are separated into two groups as Real Aperture radars (RAR) and Synthetic Aperture Radars

(SAR) according to control of the antenna beam width. Because of the resolution problem RAR systems are just operational for short distance, short wavelength and low altitude operational conditions. These operational circumstances restrict the covered area as well as short wavelength causes atmospheric attenuation and scattering of the signal. All these defects of RAR systems were passed over with the development of SAR systems. SAR systems operate the short antennas along with various data recording and operating techniques enabling to extend synthetically the antenna length. As a result, even distant objects can be sensed using short antenna beam length not requiring lengthy antennas. Besides these advantages, SAR systems are able to use interferometry.

SAR Interferometry (InSAR) is a technique to derive Digital Elevation Model (DEM) from at least two complex SAR images. The data are either taken simultaneously (single-pass mode) or sequentially (repeat-pass mode) by airborne or space-born sensors (carriers: plane, satellite, shuttle etc.). To date, one of the most important single-pass interferometry measurement campaigns is the Shuttle Radar Topography Mission (SRTM) completing its mission successfully after 11 days of operation between 11th and 22nd of February 2000.

On the other hand, several satellite systems like ENVISAT, ERS 1-2, RADARSAT 1-2, ALOS, JERS-1 etc. (see section 2.3 for detailed information about these systems) have acquired SAR images by repeat-pass. One of the most advanced systems is the German TerraSAR-X (TSX) satellite launched on June 15th, 2007 (see section 2.3 for detailed information). It is expected that TSX will be one of the leader of a new revolution for SAR technologies. It offers high resolution (~1m by Spotlight mode) imagery which could not been achieved from radar technologies up to this time similar to high resolution optical imagery. In contrast to optical sensors, TSX can be operated under all weather conditions without being influenced by clouds. The data sets, provided by TSX newly obtained by scientific community and evaluations are currently being performed.

As mentioned above, utilizing the advantages of SAR technology, indeed the planimetric locations of target ground objects, elevations of them can be determined using interferometry. Through the interferometric data, interferograms (fringe maps) can be generated and applying interferometric processing steps height models can be created for large coverage interest areas.

The main targets of this investigation can be summarized as; generation of height models derived from TSX SAR image-pairs and evaluation by comparison with more accurate reference height models as well as height models based on high resolution optical satellite images. Absolute and relative accuracy, stability, homogeneity and dependency upon various parameters are determined. The approach will be demonstrated using TSX data covering Istanbul area, Turkey.

1.2 STATE OF THE ART

Digital Elevation Models (DEMs) are used for several purposes by different working groups from various disciplines. They are applied in such distinct fields like terrain determination (such as point elevation, slope, distance, aspect), environmental analysis, cartography, civil applications, geographical information systems (GIS), urban planning, disaster management (forest fires, erosion, flood, earthquake), forestry, agriculture, modeling of hydrologic functions, contour line generation etc.

Caused by the varying use and requirement several methods are used for DEM generation. These methods can be divided into four main groups as ground survey, aerial photogrammetry, laser scanning and remote sensing (see section 4.1 for detailed information). As distinct from ground survey, photogrammetry and laser scanning, remote sensing offers faster data acquisition and processing moreover large area coverage for DEM generation. Satellite remote sensing aiming at DEM generation can be separated into stereo-optical satellite imagery and interferometric synthetic aperture radar (InSAR). These techniques have advantages and disadvantages in comparison against each other. The InSAR technique applied in this study has several advantages against stereo-optical satellite imagery. Data collection is independent from weather conditions, clouds can be penetrated, global coverage can be obtained fast at specific times, imaging at reduced look angles is possible, and thus results in remarkable different perspectives than common vertical images, enabling resolutions to be independent from distance to the object; polarization effects can be used etc. Furthermore, besides the advantages of interferometry, the evaluated satellite TSX is able to operate different imaging modes (spotlight, stripmap and scansar). The spotlight mode offers high geometric ground resolution (1m) similar to the resolution acquired from very high resolution optical satellites.

By means of these advantages especially filling the gaps which arise from the problem of cloud coverage in DEM generation by optical imagery InSAR became operational in recent years and DEMs became the most demanded interferometric products. Accordingly, there is an increasing need for quality measures for these products to know whether they are suitable and reliable for the applications. From this point of view, this study focuses on the generation and evaluation of InSAR DEMs to contribute the satisfaction of this need. Up to date, some of researches have been performed on this subject. For example, a study about the quality assessment of SAR interferometric data was carried out by Rüdiger Gens (Gens 1998) in Hannover, Germany.

The quality of a DEM can be assessed by various procedures. One of the common procedures, for example, is the comparison with a reference DEM (Lin et al. 1994). This is one of the powerful ways to understand the quality of a DEM and has been applied in this study. The most critical point on this method is that the reference DEM have to be more accurate than evaluated DEM and has no distorsion on the comparison area. To estimate the accuracies of DEMs according to generation techniques and the required height accuracies for cartographic mapping, some standards like proposed by United States Geological Survey (USGS) can be used as a reference (see part 4.2 for detailed information). For example, while the accuracy of a DEM, derived by space-borne SAR interferometry or optical imagery should be 0.5m-20m, the accuracy of a DEM, derived by aerial photogrammetry should be 10cm-1m. That mean's a photogrammetric DEM may be a reference for the quality assessment of DEMs derived from space-borne InSAR or optical imagery. Also in this study, photogrammetric DEMs have been used as references for the evaluation of space-borne InSAR and optical DEMs. In another example, for an interferometrically derived DEM based on satellite data, which has on average a standard deviation of about 5m in the vertical direction, a reference DEM with an accuracy of approximately 50cm is required (Zebker et al. 1994b).

1.3 TOPICS OF THE STUDY

As mentioned before, TSX is one of the latest satellites gathering SAR images that can be used for InSAR. To evaluate the quality of its data sets and to determine the possible applications, several groups of scientists are analyzing TSX-products (URL 1). One of them is this project about the generation and evaluation of TSX DEMs.

As well known, different accuracy levels are required for different types of application. For example, while forestry or agriculture do not need high accurate DEMs, disaster management applications may need. The essence objective of this project is the determination of precise, stable, homogeneous TSX DEMs and analysis by comparing with reference DEMs and by this way interpretation of their possible applications for different fields. For this reason after generation of DSMs based on TSX several evaluation analysis have been performed.

1.4 STRUCTURE OF THE STUDY

The targets of this study can be supposed as two main items. One is the generation of DEMs using TSX SAR image-pairs and the second one is the evaluation of them. Towards these items, the structure of the study is separated into six main chapters.

As usual, the first chapter is *introduction* in where general information are given. It contains, the motivation (section 1.1), state of art (section 1.2), topics of the study (section 1.3) and the structure of the study (section 1.4).

The second chapter is identified as *Basics of Spaceborne Remote Sensing*. In this chapter the basic information about optical remote sensing (section 2.1) and radar remote sensing (section 2.2) are summarized and the main satellite SAR sensors used for interferometry (section 2.3) are explained.

The third chapter; *Interferometric Processing and DEM Generation* is one of the most important chapters in the study. The InSAR data sets (section 3.1), the programs for radar image processing and DEM generation (section 3.2) and interferometric processing steps of DEM generation (section 3.3) are described in this chapter.

At the fourth chapter of the report, *DEM Evaluation* is explained. The concepts of DEM and DEM generation techniques (section 4.1), DEM evaluation overview (section 4.2), DEM evaluation and visualization programs (section 4.3) are particularly described in this chapter.

The fifth and the vital chapter of the report is *Data, Results and Discussion*. In this chapter; at first the test fields and data sets used in the project (section 5.1) are introduced followed by the analysis for the evaluation. These sections are; shift of DSMs and preparations (section

5.2), accuracy analysis of DSMs (section 5.3), influence of interpolation (section 5.4), morphology (section 5.5), the differential DEMs (section 5.6) and shading (section 5.7). This chapter also contains the results achieved after each analysis.

The general conclusions considering the results and future targets exist at the sixth and the last chapter of this report titled as *Conclusion and Future Targets*.

In total six DEMs were used for analysis of the geometric property. Three of them are optical DEMs derived from IKONOS, SPOT-5 HRS, ASTER, the other three are InSAR DEMs derived from SRTM C-band, TSX Spotlight and TSX Stripmap. The analysis gave detailed information about these six DEMs in comparison with two accurate reference DEMs acquired by aerial photogrammetry (see section 5 for detailed information).

PART 2

BASICS OF SPACEBORNE REMOTE SENSING

Remote Sensing is the measurement or acquisition of information of some property of an object or phenomenon, by a recording device that is not in physical or close contact with them under study (Colwell 1997). It can be divided into airborne and spaceborne applications. At the airborne remote sensing, information is collected about an object or phenomenon by photography from an aircraft. In spaceborne remote sensing, a spacecraft carries sensors on-board and images from its orbit more or less permanent. Spaceborne remote sensing technique has lower resolution against aerial imaging but the resolution level improves annually with higher resolution satellite sensors (50cm-1m)(Worldview, Quickbird, IKONOS, etc.). This technique provides advantages compared to aerial photography: it offers global coverage frequently and repetitively at relatively low cost, radiometric calibrated sensors enable quantitative measurements of ground features and semi automated computerized processing and analysis are possible.

According to their imaging principles spaceborne remote sensing devices may be separated into two classed: optical and radar sensors. While optical imagery uses visible and near infrared spectrum, radar imagery uses microwaves for imaging (Figure 2.1).

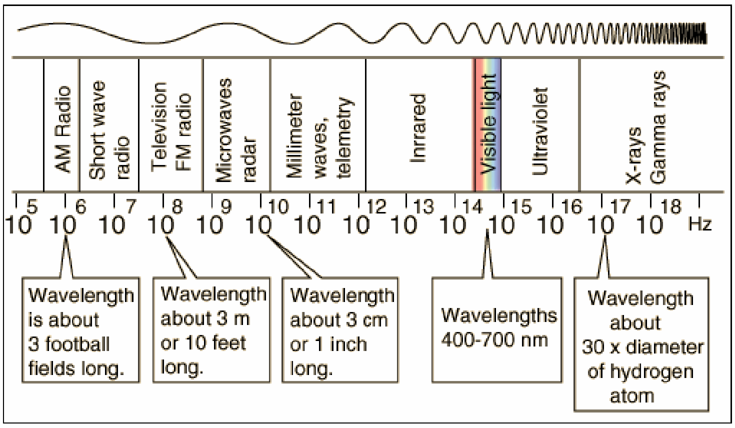

Figure 2.1 Electromagnetic spectrum (URL 2).

2.1 OPTICAL REMOTE SENSING

As known, sun is the most powerful illumination source for the Earth and emits solar radiation. By different ground objects, this solar radiation is reflected depending upon the wavelengths. The interaction of the incoming radiance with matter depends on chemical and physical surface properties of the object. Chemical: incoming signal may cause molecular resonance (i.e., those signal parts are absorbed, whereas the rest is reflected that this gives the colors we observe). Physical: roughness with respect to wavelength determines degree of directivity of reflection: like a mirror (smooth, brightness depends on position of observer) or a Lambertian surface (same brightness observed from any position) or something in between.

Optical images generate grey values by quantifying the solar radiation reflected from target ground objects using visible and near infrared CCD (charge-coupled device) sensors or other sensors. By this way, the targets can be differentiated by their spectral reflectance signatures in the remotely sensed images. Figure 2.2 shows the imaging system of optical remote sensing.

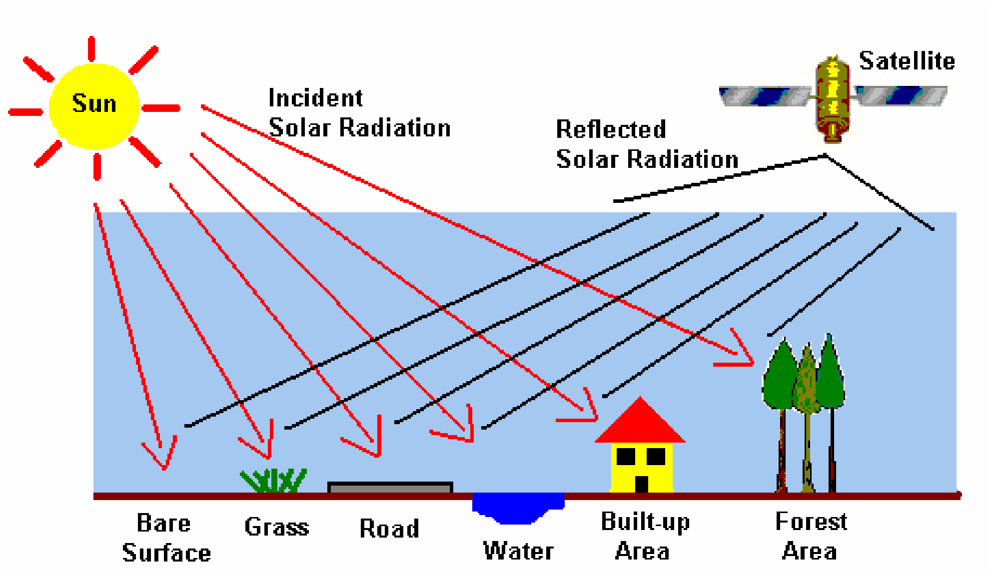

Figure 2.2 Imaging system of optical remote sensing.

In optical remote sensing, there are many kinds of imaging systems depending on visualization characteristics and they will be explained separately in this section.

2.1.1 Optical Imaging Systems

Passive optical sensors detect natural or non-natural (i.e., artifical radiance like in laser-based optical sensors) radiation which is emitted or reflected by the ground objects. Reflected sunlight is the source of radiation measured by these sensors. This radiation, emitted by the sun is named as solar radiation and it is captured by optical imaging sensors for Earth observation in the visible and near-infrared spectrum. The ground materials transmit, absorb or reflect the solar radiation. A ground object can be identified from its spectral reflectance signature. For example, vegetation has a unique spectral signature compared with other types of land cover in an optical image. Because of the absorption by chlorophyll for photosynthesis the reflectance is low in both the blue and red regions of the spectrum. It has a peak at the green region which gives rise to the green color of vegetation. In the near infrared (NIR) region, the reflectance is much higher than that in the visible band due to the cellular structure in the leaves. Hence, vegetation can be identified by the high NIR but generally low visible reflectance. In case of environmental and agricultural applications several optical sensors use near-infrared spectrum (e.g. LANDSAT satellite).

Depending upon radiometry (brightness, tone, intensity etc.), imaging geometry, spectral bands (color, hue etc.), textural and contextual information in the imaging process optical remote sensing imaging systems are classified into five groups; these are monochromatic, panchromatic, multispectral, super spectral and hyper spectral imaging systems.

Monochromatic Imaging Systems

Monochromatic imaging systems refer to light of only one wavelength. They consist of only a single color, including its tints, tones and shades. A hue modified by the addition of black, gray (black + white) and white. One of the main monochromatic imaging systems is Orbview-1.

Panchromatic Imaging Systems (PAN)

In panchromatic imaging systems, the sensor is a single channel detector sensitive to radiation within a broad wavelength range and the images occur from only one band. They don’t separate spectral information of the targets, they are displayed with grey-scale and look like black-and-white aerial images. Radiometry is the most important information for the interpretation of panchromatic images. One of the main panchromatic imaging systems is Worldview-1.

Multispectral Imaging Systems (MS)

In multispectral imaging systems, the sensor is a multichannel detector with few spectral bands. Each channel is sensitive to radiation within a narrow wavelength band and the images include spectral information and the brightness of the targeted ground objects. Multispectral imaging systems are Worldview-2, Orbview-2, IKONOS MS, Quickbird MS, LANDSAT MSS, LANDSAT TM and SPOT HRV-XS. These systems have also panchromatic bands and the ground resolutions of the images obtained from these bands are approximately fourfold better than the images derived from multispectral bands of same systems. For this reason, to achieve both the best resolution and hued image, a special technique have been developed titled as *pan-sharpening*. In this technique, fourfold high resolution PAN and hued MS images of common test field are combined and high resolution (equals to resolution of PAN) hued pan-sharpened image is obtained. Figure 2.3 shows the difference between monochromatic Orbview-1 and pan-sharpened Quickbird images of Zonguldak Turkey.

Super Spectral Imaging Systems

In super spectral imaging systems, the sensor has many spectral channels (typically >10). The bands have narrower bandwidths, enabling the finer spectral characteristics of the targets to be captured by the sensor. Examples of super spectral imaging systems are: MODIS and MERIS.

Hyper Spectral Imaging Systems

A hyper spectral imaging system is also known as an "imaging spectrometer". It acquires images in about a hundred or more contiguous spectral bands. The high spectral resolution contained in a hyper spectral image enables better characterization and identification of targets. Hyper spectral images have potential applications in such fields as precision agriculture (e.g. monitoring the types, health, moisture status and maturity of crops), coastal management (e.g. monitoring of phytoplankton’s, pollution, bathymetry changes). But due to technical limitations (e.g. sensors scan rate of 10 to 25 Hz) hyper spectral sensors are not able to deliver a spatial resolution of better than 2-3m across flight track even at lower operating altitudes (Wilson and Cocks 2003). One of the main hyper spectral imaging systems is Hyperion EO1 satellite.

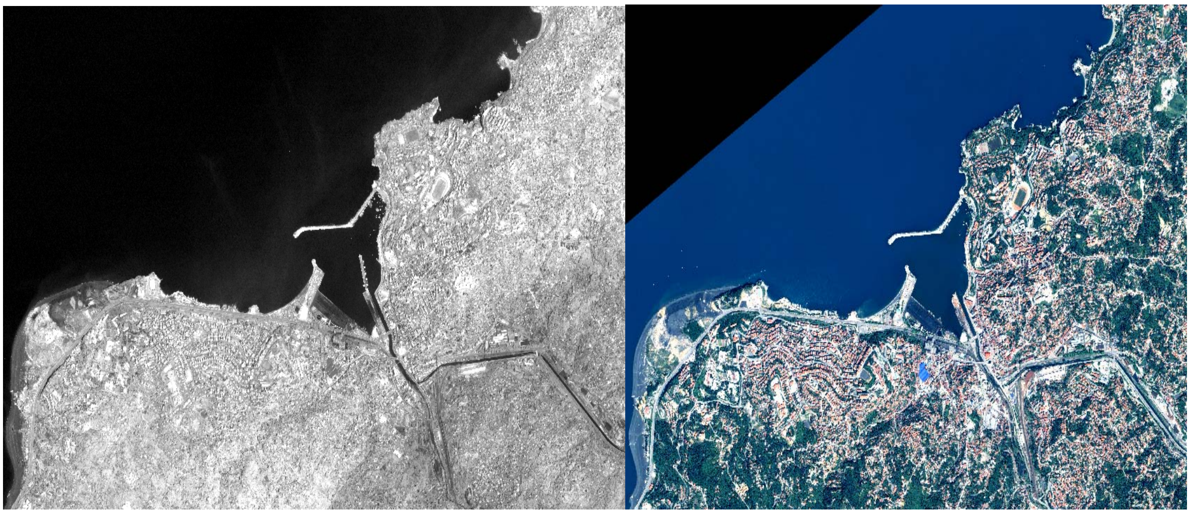

Figure 2.3 Monochromatic Orbview-1 and pan-sharpened Quickbird images of Zonguldak (Turkey).

Table 2.1 and 2.2 illustrate the existing and proposed high and very high resolution optical satellites available for civilian use (Jacobsen 2008).

2.2 RADAR REMOTE SENSING

In this section, radar system, SAR sensor characteristics and image formation and SAR Interferometry will be explained for understanding the radar remote sensing, differences from optical imagery, interferometric processing and DSM generation from SAR images.

2.2.1 Radar System

RAdio Detection and Ranging (RADAR) technology was invented for detecting and tracking of target objects during World War II for military reconnaissance purposes especially to support nighttime bombing.

Table 2.1 The existing high and very high resolution optical satellites available for civilian use.

Sensor	**Country**	**GSD (nadir) [m]** **PAN / MS**	**Swath [km]** **PAN / MS**
SPOT 1-4	France	10 / 20	60
SPOT 5	France	5 (2.5) / 10	60
SPOT 5 HRS	France	5 x 10	120
MOMS-02 / -P	Germany	5.8 / 16.5	37 / 78
IRS-1C/1D	India	5.8 / 23.5	70 / 142
Resourcesat	India	- / 5.8	70
KOMPSAT	S. Korea	6.6	17
Terra ASTER	Japan	15/ (30, 90)	60
IKONOS	USA	0.82 / 3.2	11.3
EROS A	Israel	1.8	12.6
QuickBird	USA	0.61 / 2.44	16.4
OrbView 3	USA	1 / 4	8
EROS B	Israel	0.7	14
FORMOSAT 2	Taiwan	2 / 8	24
IRS-P5 Cartosat-1	India	2.5	30
TopSat	UK	2.5 / 5	15 / 10
Beijing-1	China	4 / 32	/ 600
ALOS	Japan	2.5	35 (70)
KOMPSAT-2	S. Korea	1 / 4	15
Resource DK1	Russia	1 / 3	28
IRS Cartosat-2	India	<1	9.6
WorldView-1	USA	0.45	15.8
CBERS-2B	China/Brasil	2.5 / 20	27 / 120
IRS Cartosat-2A	India	1	10
GeoEye-1	USA	0.41, 0.5, 0.59/ 1.65	15.2
RapidEye	Germany	- / 6.5	77
WorldView-2 spectral	USA	0.46/ 1.84	16.4
THEOS	Thailand	2 / 15	22 / 90

Table 2.2 The proposed high and very high resolution optical satellites available for civilian use.

Sensor	**Country**	**Proposed launch**	**GSD(nadir) [m] PAN / MS**	**Swath [km] PAN / MS**
Resourcesat-2	India	2010	5.8 / (23.5)	70/140
NigeriaSat-2	Nigeria	2010	2.5 / 5	-
EROS C	Israel	2010	0.7 / 2.8	11
Pleiades	France	Begin 2010 + 11	0.7 / 2.8	20
Cartosat-3	India	2011	0.35 / -	-
ResourceSat-3	India	2011	2.5 / 5.8	25
GeoEye-2	USA	-	0.25 /	-

The imaging systems of optics and radar are totally different, while the object reflection of the spectral range used by optical images is mainly depending upon chemical features of the object; radar is mainly depending upon the physical situation of the surface. The principle of radar system relies upon emitting electromagnetic pulses in the radio and microwave spectrum and detects the reflections of these pulses from targets at the interest area by aid of its transmitting and receiving antennas. Radar system can be divided into three groups concerned with different usage purposes. First group of radar systems are Doppler radars. The radar beam reflected from the objects towards or away from the radar antenna and the radial motion velocity can be inferred from the measurement of Doppler shift. They are not capable for imaging and using for only determining the object velocity in the direction of the radar antenna’s beam. Doppler radars are used in air defense, air traffic control, sounding satellites, police speed guns, and radiology. The second group of radars are the plan position indicators (PPI). The PPI radars produce continuously updated displays of objects around its turning antenna. By this way, the distance of objects and the heights above ground can be drawn as concentric circles. The PPI radars are used in meteorology, air traffic control, on board ships and aircrafts for many applications. Figure 2.4 shows the examples of Doppler and PPI radar mechanisms.

The third and most preferential radar systems in remote sensing are Side Looking Radars (SLR) were improved for terrain surveillance after World War II.

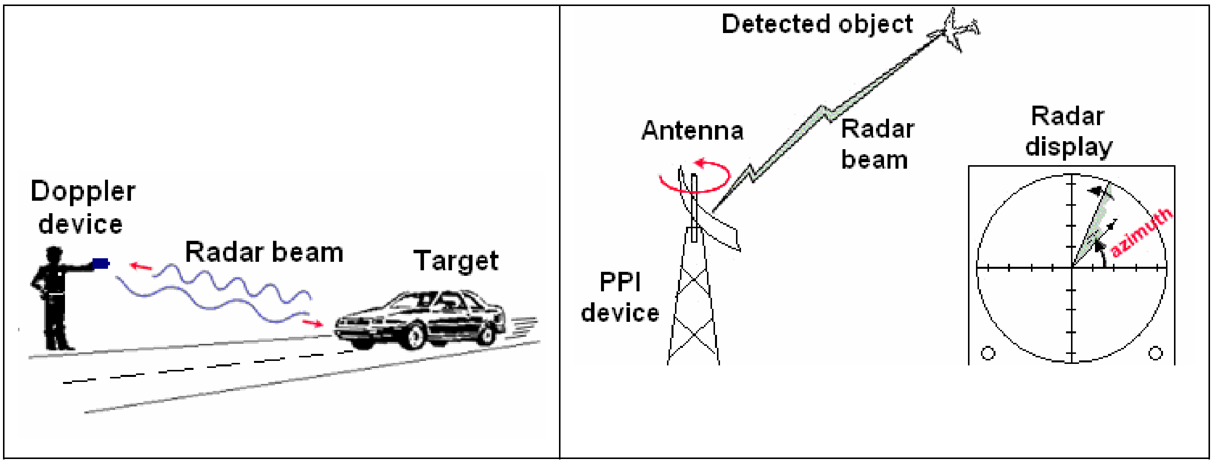

Figure 2.4 Doppler and PPI radar mechanisms.

In SLR systems, radar illuminates a strip of terrain parallel to flight direction. Figure 2.5 shows the SLR geometry.

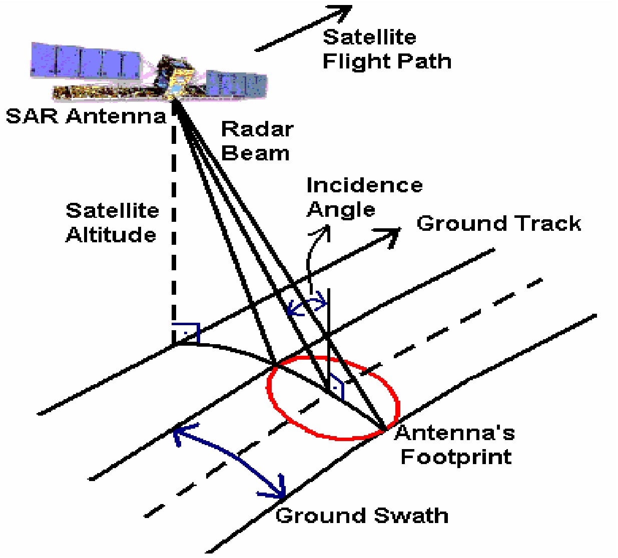

Figure 2.5 Side Looking Radar geometry.

For data display and recording a cathode ray tube and film was used, today it is based on digital recording. At the first applications with SLR, permanently cloud-covered areas in the tropics were mapped and the success of the system had been clearly seen. The antenna beam width (β) of SLR system is directly proportional with the wavelength (λ) of emitting pulse and inverse proportional with antenna length (AL). That means:

$$\beta = \lambda / AL \tag{2.1}$$

SLR systems are divided into two groups concerned with controlling the beam width of antenna. The antenna beam width is controlled by physical antenna length in Real Aperture Radar (RAR) and the spatial resolution of RAR is primarily determined by the size of the antenna used: the larger antenna means better spatial resolution. Other determining factors include the pulse duration (t) and the antenna beamwidth (β). Radar has two main resolution components named as *range* and *azimuth resolution*. Range resolution of RAR sytems is defined as:

$$\mathrm{Re}\, s_{range} = c\, t / 2 \qquad \text{(c is the speed of light)} \tag{2.2}$$

On the other hand, the azimuth resolution of RAR sytems is defined as:

$$\mathrm{Re}\, s_{azimuth} = \lambda \times R / AL = \beta \times R \quad \text{(R, the distance antenna-object)} \tag{2.3}$$

For systems where the antenna beamwidth is controlled by the physical length of the antenna, typical resolutions are in the order of several kilometers (Sarmap 2008). For example, to provide 0.01 mrad antenna beam width with 3cm wavelength radar pulse, it has to be used 3km long antenna:

$$AL = \left(3 \times 10^{-2}\, m / 1 \times 10^{-5}\, rad\right) = 3\, km \tag{2.4}$$

It can be easily seen from equation 2.4, in order to achieve short beam width for a high azimuth (flight direction) resolution in the image, the antenna must be impracticably long. By the reason of this problem, RAR system usage is limited in short distance, short wavelengths and low height operation conditions. And these conditions limit the achieved land-cover area and the short wavelength causes atmospheric attenuation by scattering at aerosols, dust etc.. All these problems of RAR, caused by unrealistic antenna length are solved by a new radar technology, called Synthetic Aperture Radar (SAR).

The range resolution of a pulsed radar system is limited fundamentally by the bandwidth of the transmitted pulse. A wide bandwidth can be achieved by a short duration pulse. However, the shorter the pulse, the lower the transmitted energy and the poorer the radiometric resolution. To preserve the radiometric resolution, SAR systems generate a long pulse with a linear frequency modulation (or chirp). After the received signal has been compressed, the range resolution is optimised without loss of radiometric resolution.

Compared to RAR, SAR synthetically increases the antenna's size to increase the azimuth resolution though the same pulse compression technique as adopted for range direction. Synthetic aperture processing is a complicated data processing of received signals and phases from moving targets with a short antenna. It theoretically converts the short antenna effect into the effect of a large antenna by synthetic aperture length, i.e. the beam width by range which a RAR of the same length, can project in the azimuth direction. The resulting azimuth resolution is given by half of RAR as shown in Figure 2.6 and as follows:

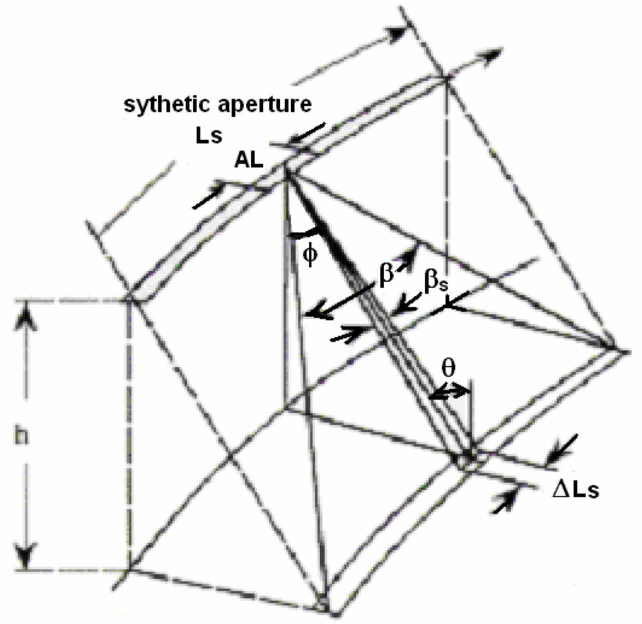

Figure 2.6 Relation between real aperture and synthetic aperture radar.

βs = synthetic beam width

ΔLs = azimuth resolution

h = height

ϕ = off nadir angle

- Real beam width: $\beta = \lambda / AL$ (again 2.1)

- Real resolution: $\Delta L = \beta \times R = L_s$ (synthetic aperture length) (2.5)

- Synthetic beam width: $\beta_s = \lambda / 2 \times Ls = AL / (2R)$ (2.6)

- Synthetic resolution: $\Delta L_s = \beta_s \times R = AL / 2$ (2.7)

This is the reason why SAR has a high azimuth resolution with a small size of antenna regardless of the slant range, or very high altitude of a satellite (Sarmap 2008).

2.2.2 SAR Sensor Characteristics and Image Formation

SAR is also a side-looking instrument like SLR, but it employs a more sophisticated digital signal processing technique (Santitamnont 1998). It is a remote sensing imaging system whose primary output product is a two-dimensional mapping of the radar brightness of a scene. Radar brightness is an expression of the scene's reflectivity in response to oblique illumination by microwave electromagnetic emissions. By definiton, a SAR must be mounted on a moving platform, such as an aircraft or a satellite, and illumination is directed to the side (and downward) to the surface. Its images are formed by scanning the area in two dimensions: range and azimuth. Range scanning is essentially at the speed of light, as radar pulses are transmitted and their reflections (backscatter) are received and recorded. Azimuth scanning is accomplished by the forward motion of the radar (Schwartz 2005).

SAR sensors can provide superior information compared with optical sensors operating in the visible and infrared regions of the electromagnetic spectrum. They provide their own source of illumination and able to obtain data all times of the day not to be worried about cloud cover using longer wavelength of the radar. In coherent radar the phase of the transmitted signal is retained and used as reference against the returned signal (Hanssen 2001). The sensors produce directed beam pulses which illuminate the terrain where the incoming radar-frequency energy is reflected. This reflection depends on physical characteristics of the surface features (geometric structure, roughness and orientation), the electrical characteristics of the ground objects (dielectric constant, moisture content, and conductivity) and the radar frequency of the sensor. According to these characteristics high-resolution reflected returns generate SAR data.

A SAR sensor has some characteristics as centre frequency, spatial resolution, altitude range, sensitivity range, swath width, bandwidth, channels, main antenna, ambiguity ratio, azimuth ambiguity ratio, azimuth scan, image polarizations, calibration, and image processing and operational modes. The radar sensor frequencies are usually between 0.225-36.0 GHz which translates the wavelengths between 133.0-0.83cm. Nevertheless, lower or higher frequency radar sensors exist for particular applications. Table 2.3 shows the radar sensor's frequency bands.

Table 2.3 Radar sensor's bands, frequencies and wavelengths.

Band	**Frequency Interval (f) (GHz)**	**Wavelength (λ) (cm)**	**Used by**
P	0.225-0.390	133-76.9	AIRSAR
L	0.390-1.550	76.9-19.3	JERS-1 SAR, ALOS PALSAR
S	1.550-4.200	19.3-7.10	Almaz-1
C	4.200-5.750	7.10-5.20	ERS-1/2 SAR, RADARSAT-1/2, ENVISAT ASAR, RISAT-1, SRTM
X	5.750-10.90	5.20-2.70	TerraSAR-X, COSMO-SkyMed, SRTM
K_u	10.90-22.00	2.70-1.36	Military Domain
K_a	22.00-36.00	1.36-0.83	Military Domain
Q	36.00-46.00	0.83-0.65	-
V	46.00-56.00	0.65-0.53	-
W	56.00-100.00	0.53-0.30	-

The spatial resolution and the other sensor characteristics correspond with SAR sensor type. The study issue TerraSAR-X SAR sensor and other main satellite SAR sensors used for interferometry are described in section 2.3 separately.

SAR allows the high resolution space-borne imaging but it is a highly computation intensive application field, both for the SAR image formation and for any post processing aimed at improving or analyzing the images. As mentioned above, the SAR image formation involves a double integration of the raw data, known as *range and azimuth* compressions, aimed to invert the physical process of SAR imaging (Appiani et al. 1996). On the other hand, the SAR image post processing attempts to improve the quality of the whole images, strongly impressed by speckle effects, intrinsically inherent to the imaging process.

Speckle is the signal of distributed targets. Due to the coherent nature of the signal we deal with interference (same in case of laser). Many scatterers are inside each resolution cell which can not be observed directly, instead the complex sum of all those small signals (sum of complex phasors) are measured. Since the individual blades of grass of a meadow are distributed different for every single resolution cell, the mapping of such natural soil type can be modelled as random process (exponential distribution in case of intensity image, Rayleigh for amplitude image): such area appears like salt and pepper in the image. This is why some authors refer to speckle as noise like effect. In case of intensity image it acts like a multiplicative noise (Soergel 2010).

In terms of geometry, SAR imagery is different from optical imagery. The geometric differences between the two imaging techniques will be explained utilizing Figure 2.7. A slight mountain with the points A, B, C and D is taken once with an optical device and once with an active radar; both from the same viewing direction. On the figure, while the geometric optics measures the viewing angles, from where the points A to D are seen, radar measures the distance of these points from the sensor. For the optical imager, points C and D seem closely together, while the radar measures a great distance between them. The image of the optical sensor seems to give an inverse presentation of the range distances of the radar sensor (Schreier 1993).

The data acquisition by SAR is based on the direction perpendicular to the orbit and the distance and SAR image geometry can be more complicated according to terrain inclination. The determination of the location based on distances is causing three main distortions in steep terrain. These distortions are named as Foreshortening, Layover and Shadow can be seen in Figure 2.8.

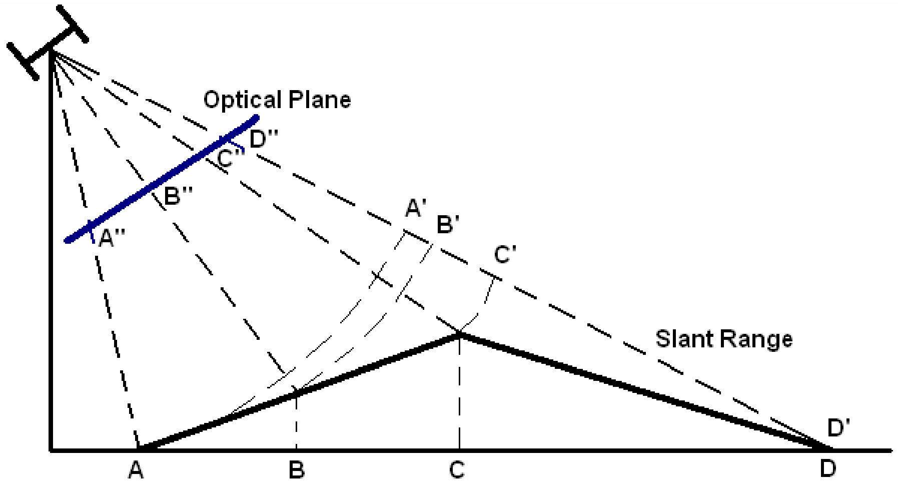

Figure 2.7 Comparison between optical imagery and radar imagery.

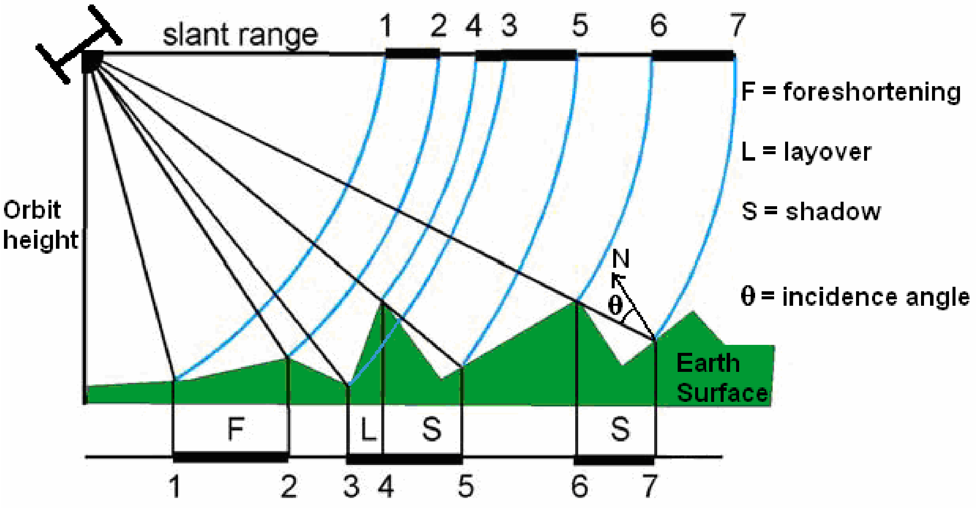

Figure 2.8 Main distortions in location determination by SAR.

If the radar wave front interacts with the local ground near to parallel (the incidence angle is near 0º), the entire area of this near-parallel interaction is imaged only with short time delay. This distortion is named as *foreshortening* and it can clearly be identified in SAR images. They occur as bright fringes on the sensor-side of mountains and give SAR images of hilly terrain their typical plastic appearance (Schreier 1993). An example of this distortion can be seen in figure 2.8 between point 1 and 2.

If the terrain inclination is exceeding the incidence angle, the position of a higher elevated point is shown before the position of a lower point even if this is reverse in the object space (point 4 in figure 2.8 is located in the slant range image before point 3). This so called *layover* is mixing the radar signals and there is no possibility of a correct reconstruction in such steep parts. The incidence angle refers to the object, the viewing angle to the sensor. In case of flat terrain they are approximately the same. Caused by the higher incidence angle of SAR, the viewing *shadows* (areas with no information) are larger like usually in optical images. The compression of the information by the foreshortening is reducing the information in these parts. Corresponding to this, in the radar view direction different height accuracy based on interferometric SAR than across to it can be expected, that means a dependency upon the aspects is possible (Sefercik and Jacobsen 2007).

In this study, two different modes of SAR image-pairs of TSX have been used for DSM generation. First image-pair are TSX Stripmap mode (TSX SM) and have 3m resolution and 30km swath width. The second image-pair are TSX High Resolution Spotlight mode (TSX SL) and have 1m resolution and 10km swath width. These data sets will be explained separately in section (3.1), but for the first impression and visualization the differences between a SAR image and an optical image, the figures below can be considered. Sequentially, TSX SM (Figure 2.9) image, high resolution TSX SL (Figure 2.10) image and a high resolution optical counterpart image (1m IKONOS) (Figure 2.11) are presented. For the clear comparison, an interest area which contains buildings, roads and intersections is selected from Historical Peninsula (test field 2 in this project will be described in part 5.1) of Istanbul, Turkey.

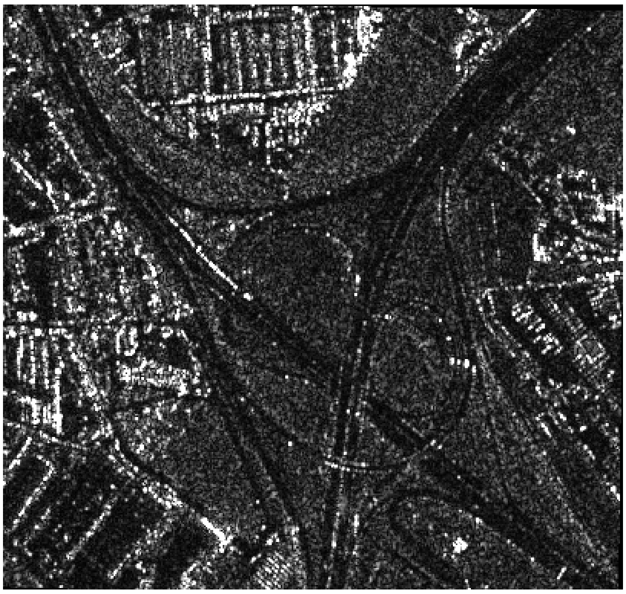

Figure 2.9 TSX SM SAR image(3m).

Figure 2.10 High resolution TSX SL (1m).

Figure 2.11 High resolution IKONOS (1m).

Against optical images, SAR images have some speckle effects which can be reduced by filtering but at the same time this causes a loss of information. On the other hand some special objects like railroads with the metallic rails can be seen clearer like in optical images. The information contents of SAR images can be improved by multi polarization like shown in Figure 2.12. By the combination of HH and VV polarization the image interpretation is improved (Jacobsen 2008).

Figure 2.12 Multi-polarization (HH/VV) TSX SL image reduced by factor 2 from the city of Dresden.

2.2.3 SAR Interferometry

As mentioned before, unlike RAR technique SAR synthetically increases the antenna's size or aperture enhancing the azimuth resolution though the same pulse compression technique as adopted for range direction. In synthetic aperture processing signals and phases are received from targets using a small antenna than this effect is converted to effect of a large antenna with synthetic aperture length.

In SAR Interferometry (InSAR), basically two SAR images are used for obtaining elevation data in addition to planimetric location information. These SAR images can be acquired in specific time intervals -can be taken as multiple of repeat cycle- or simultaneously from different view angles on the same interest area. In this manner, InSAR technique is divided into two items as single-pass InSAR and repeat-pass (double-pass) InSAR.

In single-pass InSAR, carrier has two independent SAR instruments and they simultaneously collect data from the different look angles on the same interest area. Shuttle Radar Topography Mission (SRTM) was an important radar application which used this technique. On the other hand, in repeat-pass InSAR, one SAR instrument is used and it passes two times from the same interest area between specific time intervals (a multiple of repeat cycle) and collects data from different looking angles like in single-pass InSAR. The main differences from single-pass InSAR are occurred due to the changes of the atmospheric conditions and climates. The structure of vegetations, forests etc. may change at the period between two data collection times. But actually, in conclusion both two techniques use two SAR instruments simultaneously or intermittently and constitute same geometry for the mathematical calculation of elevations using synthetic antenna effect. Figure 2.13 presents the geometry and the contents of SAR interferometry and following formulas shows the mathematic calculation of elevations using synthetic antenna effect.

According to the Figure 2.13, mathematical formulas to achieve ΔZ (Sörgel 2008):

$$r_2 = r_1 - \Delta r \tag{2.8}$$

$$\Delta r = r_2 - r_1 \tag{2.9}$$

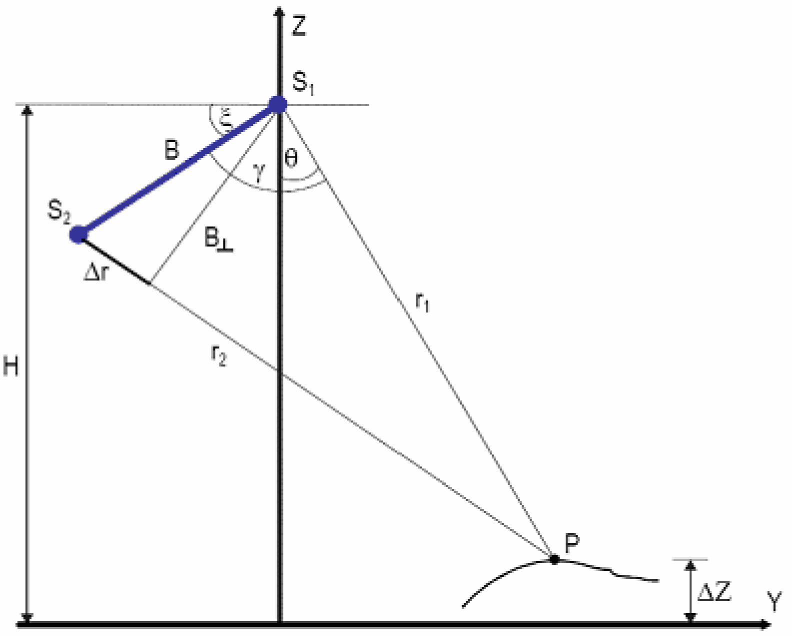

Figure 2.13 InSAR geometry (Sörgel 2008).

$$\Delta\varphi = \varphi_1 - \varphi_2 = (2\pi / \lambda) \times \Delta r \tag{2.10}$$

$$r_2^2 = r_1^2 + B^2 - 2r_1 \times B \times \cos\gamma \,. \quad \text{(cosine law)} \tag{2.11}$$

$$= r_1^2 + B^2 + 2r_1 \times B \times \sin(\theta - \xi) \,. \tag{2.12}$$

$$\sin(\theta - \xi) = (r_2^2 - r_1^2 - B^2)/(2r_1 \times B) \tag{2.13}$$

$$= (r_2 - r_1)(r_2 + r_1)/(2r_1 \times B) - (B^2/(2r_1 \times B)) \tag{2.14}$$

If it is considered that: $B << r_1$, $2r_1 + \Delta r \approx 2r_1$ can be written. (2.15)

In this case: $(r_2 - r_1)(r_2 + r_1)/(2r_1 \times B) \approx \Delta r \times (2r_1 + \Delta r)/(2r_1 \times B)$ (2.16)

$$\approx (\Delta r \times 2r_1)/(2r_1 \times B) \tag{2.17}$$

$$\approx \Delta r / B \tag{2.18}$$

Using formula 2.10: $\Delta r = (\Delta\varphi \times \lambda)/2\pi$ (2.19)

In that case: $\sin(\theta - \xi) \approx \Delta r / B \approx (\Delta\varphi \times \lambda)/(2\pi \times B \times P)$ (2.20)

$$\theta = \xi + \arcsin((\Delta\varphi \times \lambda)/(2\pi \times B \times P)) \quad (2.21)$$

$$\Delta Z = H - r_1 \times \cos\theta \quad (2.22)$$

In conclusion ΔZ is obtained by:

$$\Delta Z = H - r_1 \times \cos[\xi + \arcsin((\Delta\varphi \times \lambda)/(2\pi \times B \times P))] \quad (2.23)$$

The meaning of contents in formulas;

H = altitude from S_1

B = baseline between two SAR antennas

θ = view angle from S_1

ξ = baseline declination

λ = wavelength

$\Delta\varphi$ = phase difference

π = pi ~ 3.1416

r_1, r_2 = slope distances between target point and SAR antennas

P = 1, 2 (single-pass or repeat-pass InSAR)

ΔZ = Height of target point

2.3 MAIN SATELLITE SAR SENSORS USED FOR INTERFEROMETRY

By this time, several space-borne SAR sensors have been used for interferometry as SRTM, ENVISAT ASAR, ERS, RADARSAT, JERS and ALOS PALSAR. One of the most actual space-borne SAR sensors is TerraSAR-X (TSX) which is the main topic of this study. The space-borne SAR sensors have different operation modes and data collection characteristics. They will be described in this section separately.

2.3.1 TerraSAR-X (TSX)

In these days, TSX is one of the most modern SAR satellites and its data will be evaluated in this study. The satellite has been launched on June 15th 2007 from oldest Russia's space launch facility, Baikonur Cosmodrome in Kazakhstan. It is built in German; the lifetime will be at least 5 years on the space.

The mission is a joint project in a public private partnership (PPP) between the German Ministry of Education and Science (BMBF), the German Aerospace Center (DLR) and the Astrium GmbH. Under DLR contract Astrium constructed and built the satellite while DLR is responsible for the development of the ground segment, instrument calibration and scientific use of satellite at its lifetime (URL 3).

TSX is one of the most advanced SAR satellites using interferometry until this day and offers the highest quality spatial data that were not available from space before using high frequency X-band SAR sensor which can be operated in different imaging and polarization modes. Figure 2.14 shows the system components of satellite TSX.

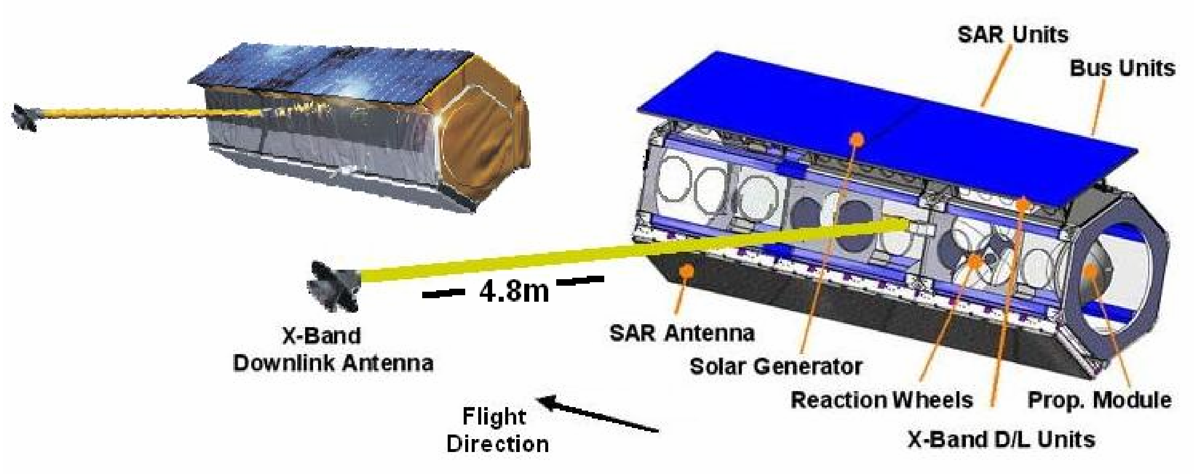

Figure 2.14 System components of TSX (URL 3).

The system compontents of TSX are listed in Table 2.4 below:

Table 2.4 System components of TSX (URL 3).

Launch date	15 June 2007
Launch site	Baikonur, Kazakhstan (Russia)
Carrier	Dnepr-1
Satellite mass	1230 kilogram
Satellite size	5 m height x 2,4 m diameter
Orbit characteristics	514 km altitute, 11 days repetition, 97.44º inclination
Antenna	4.8 m active array, multi-pol, steerable in elevation and azimuth
Radar frequency	9.65 GHz
Power consumption	800 W in average
Data reception, Mission operation	DLR, Neustrelitz, Oberpfaffenhofen, Weilheim
Bandwidth	150 MHz (300 MHz experimental)
Memory	256 Gbit (end of life)
Downlink	300 Mbit/s
Lifetime	At least 5 years
Imaging modes	Stripmap, Spotlight, and ScanSAR

As it can be seen from Table 2.4, TSX uses 3 different operation modes as Stripmap, Spotlight, and ScanSAR. These operation modes contain different imaging contents and properties, explained in detail below.

- **Stripmap Mode (SM)**

Operating Stripmap mode, TSX acquires long strips up to 1650km length with 30km swath width. In order to achieve an azimuth resolution similar to the range resolution on the order of 3 meters, the antenna length in azimuth has to be short. This in turn requires a high pulse repetition frequency (PRF) of typically 6 kHz that limits the range extension of the swath to about 30km (Eineder et al. 2003). The ground swath is illuminated with a continuous sequence of pulses while the antenna beam is fixed in elevation and azimuth. This results in an image strip with continuous image quality in azimuth (Roth 2003). The resolution of this imaging mode is lower than Spotlight and around 3-6m. The single look complex data are also available for this imaging mode. Figure 2.15 shows the imaging geometry and the following Table 2.5 presents the characteristics of TSX Stripmap mode.

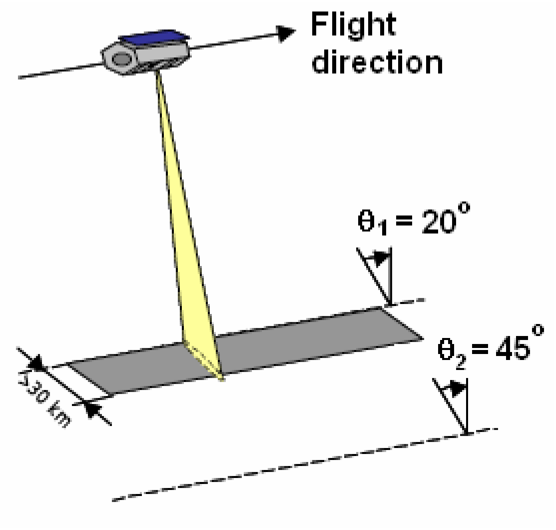

Figure 2.15 Geometry of TSX Stripmap mode.

Table 2.5 Characteristics of TSX Stripmap mode.

Swath width	30km (polarimetric mode, 15-30km)
Acquisition length	≤1650km
Azimuth resolution	3-6m
Full performance incidence angle range	20º-45º
Ground range resolution (45º-20º incidence angle)	1,7-3,5m

- **Spotlight Mode (SL)**

TSX is capable to operate two types of Spotlight modes. The first type purely named as Spotlight mode the scenes of interest area can be obtained for an area of 10kmx10km (length and width) and recorded with 2m resolution. At the second type, the lengths of the scenes are shorter by 5kmx10km but offer higher resolution. This type is named as high resolution Spotlight mode and the scenes have 1m azimuth resolution. Between these two types of Spotlight mode just the geometric azimuth resolution is different in order to increase the azimuth scene coverage of Spotlight mode.

During the observation of a particular ground scene the radar beam is steered like a spotlight so that the area of interest is illuminated longer and hence the synthetic aperture becomes larger. The Maximum azimuth steering angle range is ±0.75º (Roth 2003). The single look complex data is available for TSX Spotlight mode. Figure 2.16 shows the imaging geometry and the following Table 2.6 presents the characteristics of TSX Spotlight mode.

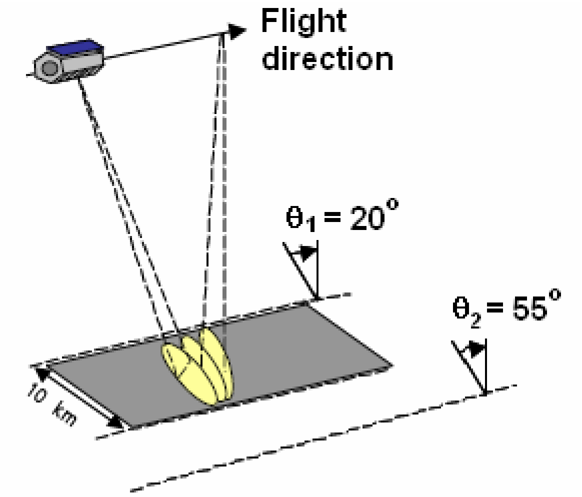

Figure 2.16 Geometry of TSX Spotlight mode.

Table 2.6 Characteristics of TSX Spotlight mode.

Swath width	10km
Acquisition length	10km or 5km (in high resolution Spotlight mode)
Azimuth resolution	1-2m
Full performance incidence angle range	20º-55º
Ground range resolution (55º-20º incidence angle)	1,5-3,5m

- **ScanSAR Mode**

This mode of TSX is not suitable for mapping purposes which need high precision. Because of the reduced azimuth bandwidth, the azimuth resolution of this mode is 16-30m. However, in comparison with Spotlight and Stripmap it provides larger area coverage (100km width and acquisition length up to 1650km) by scanning several adjacent ground sub-swaths with simultaneous beams, each with a different incidence angle. This mode may be useful for the projects which need wide interest areas like forestry, oceanography (ship surveillance, vessel detection), disaster monitoring (the motions of ice shelves, floods, volcanoes etc.), land use, agriculture and so on. Figure 2.17 shows the imaging geometry and the following Table 2.7 presents the characteristics of TSX ScanSAR mode.

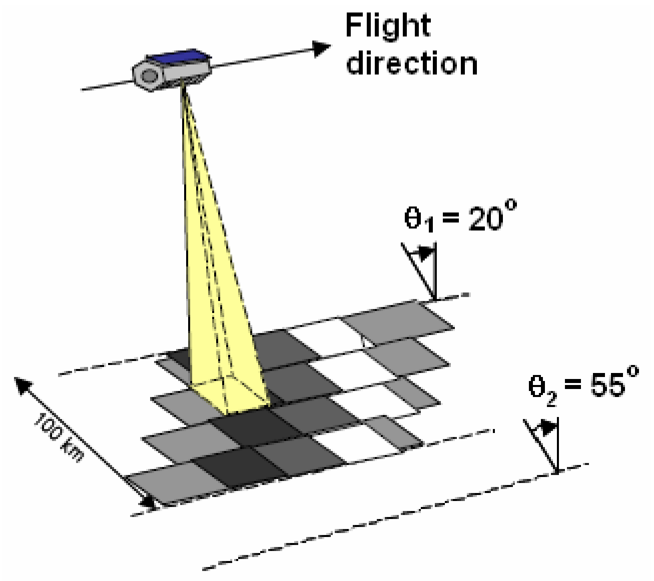

Figure 2.17 Geometry of TSX ScanSAR mode.

In this project, the ScanSAR mode of TSX was not used. Because of lower resolution, this mode is not suitable for the purposes and TSX Spotlight and Stripmap modes were preferred.

These modes provide high resolution images for detailed analysis as well as width swath data whenever a larger coverage is required and imaging can be possible in single, dual and quad-polarization. Besides, TSX data can be used for interferometry by this way the digital surface model (DSM) generation is possible. And this property of its data consists the essence of this project.

Table 2.7 Characteristics of TSX ScanSAR mode.

Swath width	100km
Number of sub-swaths	4
Acquisition length	≤1650km
Azimuth resolution	16-30m
Full performance incidence angle range	20º-45º
Ground range resolution (45º-20º incidence angle)	1,7-3,5m

As a summary of the advantages of TSX;

- Very high spatial and temporal resolution with 11 days repeat period
- Single look complex is available (for Spotlight and Stripmap modes)
- Large area coverage by ScanSAR mode (100km)
- The detected images can be ordered as ground range and geocoded products
- Doubled bandwidth (300 MHz experimental)
- The redundancy concept in the satellite receiving chain and the front-end design offer the possibility to use the second spare receiving channel in parallel to the main receiving channel, raw data from two antenna halves can be acquired independently and simultaneously by this way
- Dual receive antenna mode enables the acquisition of full polarimetric data as well as along track interferometry
- A number of images with different content will be acquired and analyzed with respect to resolution, radiometry and geometric accuracy
- The ground segment is optimized for flexible response to user requests and fast image product turnaround time

In conclusion, particularly the use of TSX data shall help to extend the range of parameters observed and therewith to increase the knowledge of the factors determining the behavior of the environment. Furthermore the system shall support the management and monitoring of the Earth's resources and to beter under-stand the solid Earth processes. New and innovative technological features of the TSX enable the improvement of existing and the development of new technologies and applications (Roth 2004).

2.3.2 Shuttle Radar Topography Mission (SRTM)

Shuttle Radar Topography Mission (SRTM) had been launched to generate high resolution, near-global (60.25° northern and 56° southern latitude) and homogenous Digital Elevation Model (DEM) of the Earth at 11 February 2000. It was flown on board the space shuttle Endeavour for 11 days. SRTM was a joint project between American National Aeronautics Space Administration (NASA), the National Imagery and Mapping Agency (NIMA) and the cooperation of German Aerospace Centre DLR and Italian Space Agency. The data acquisition system of the shuttle was single-pass interferometric SAR technique. SRTM carried two different types of antennas. One of them, the main antenna was located at the cargo bay of the shuttle having a length of 12m, transmitting and receiving. The other one, outboard antenna was located at the end of a 60m long mast and was only receiving. American C-band and German/Italian X-band were used at the mission. The shuttle had 233 km orbital height and 57° inclination. Figure 2.18 shows the system components of SRTM.

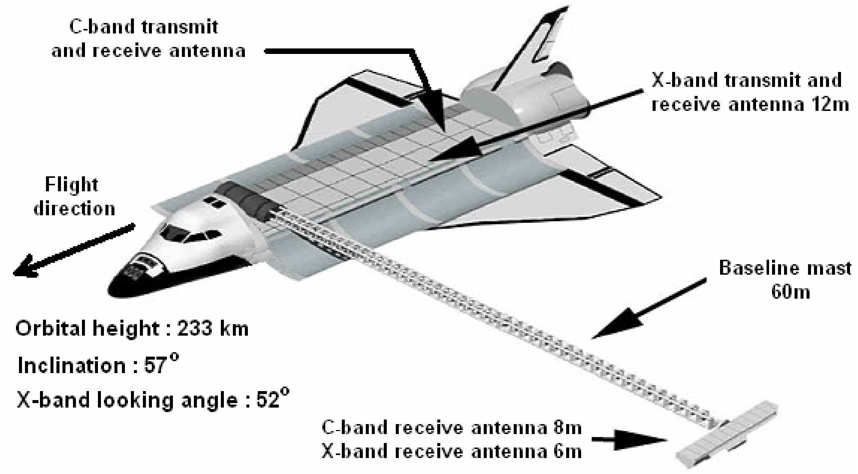

Figure 2.18 System components of SRTM.

The American C-band operated with a wavelength of 5.6cm and was able for Scansar mode. With C-band, using 225 km wide swath, 119.51 million square km were imaged corresponding to 99.97% of the target area with 1 arcsecond (nearly 31m at the equator) point-spacing. The generated height models are available only inside the USA with 1 arcsec spacing and outside the USA reduced to 3 arcsec point spacing free of charge. 8.6 Terabyte of data were recorded on 208 high density digital data tapes and stored on the shuttle. The C-band had nearly a complete coverage of Earth between 60.25° northern and 56° southern latitude. 94.6% of the mapped area was covered at least twice and approximately 50% at least three times.

German/Italian X-band operated with a wavelength of 3cm and depending on this shorter wavelength its relative vertical accuracy by theory is higher than for the C-band. X-band provided 1 arcsecond (nearly 30m at the equator) spacing data, but not free of charge. This smaller point-spacing has several benefits. For example, the difference in spacing can be seen by the interpolation in mountainous areas. The interpolation may cause a loss of accuracy nearly by the factor of 2.0 for 3 arcsec point spacing but for the smaller spacing of the X-band data only a loss of accuracy in the range of 20% (Sefercik and Jacobsen 2007). The smaller point spacing includes more morphologic details. Beside of these advantages of smaller point spacing, X-band has some disadvantages against C-band. It was not capable for Scansar mode and was limited with 45km swath width. By these reasons, X-band has large gaps between the strips. Because of just single coverage the X-band DSM shows an accuracy depending upon the aspects, for the C-band data this could not be seen because of the averaging of the height models based on different orbits.

At the imaging technique of SRTM, some sensors are responsible for measuring and controlling the proper alignment of the secondary antenna with respect to the main antenna and the attitude and position of the interferometric system in orbit. A star tracker measured the orientation of the interferometric system in orbit, which was supported by an inertial reference unit consisting of three 2-axis gyros. An optical tracker of the secondary antenna which is a video camera and LED targets, allowed a relative 3-axis measurement of the beam antennas. Additionally, two GPS antennas, one on the main antenna structure the other one on the secondary, provided 0.8m orbital position accuracy determination and furthermore, a time reference for the radar with an accuracy of 100 microseconds (Sefercik 2006).

For evaluate the SRTM DSMs at mountainous topography and forest region, a study titled "Accuracy Assessment of DEMs Derived from Shuttle Radar Topography Mission (SRTM)" had been made in 2006 by Zonguldak Karaelmas University (Sefercik 2006). A high accurate photogrammetric DEM was used as reference for the accuracy analysis of SRTM C-band and X-band DSMs and the results at the Table 2.8 below were achieved for open and forest areas separately.

Table 2.8 Results of analysis for SRTM X-band and C-band (SZ= root mean square error, α = slope; % = covered areas) (Sefercik 2006).

REF DEM	**SRTM X-band**		**SRTM C-band**	
	1st iteration (SZ)	2nd iteration (SZ)(without bias)	1st iteration (SZ)	2nd iteration (SZ)(without bias)
Open area	4.55m +10.6 m*tan(α) 74.76%	4.01m +7.9m*tan(α) 74.76%	5.92m +5.7m*tan(α) 77.02%	4.35m +6.7m*tan(α) 77.02%
Forest	5.73m +13.0m*tan(α) 25.24%	4.47m +10.8m*tan(α) 25.24%	6.32m +6.5m*tan(α) 22.98%	5.74m +2.6m*tan(α) 22.98%

SRTM data have several advantages like near-global coverage, homogeneity, wide overlap from ascending and descending paths, extensive availability and for C-band free of charge. That’s why its data are used in several applications by science community, commercial providers and operational users.

2.3.3 Environmental Satellite (ENVISAT)

Environmental satellite (ENVISAT) is one of the most powerful Earth observation satellite of Europe, operated by European Space Agency (ESA). The satellite was launched on March 1st 2002 by Ariane rocket and fitted its orbit successfully. ENVISAT is an advanced observation satellite and its data are used for atmosphere, ocean, land, ice measurements, enable geological investigations and climatologically and environmental change monitoring. For example, the changes of the terrain height caused by the Aquila earthquake in Italy at April 6th, 2009 was determined by this satellite InSAR application (Figure 2.19).

ENVISAT is the biggest observation satellite of Europe. The system characteristics of satellite are listed in Table 2.9.

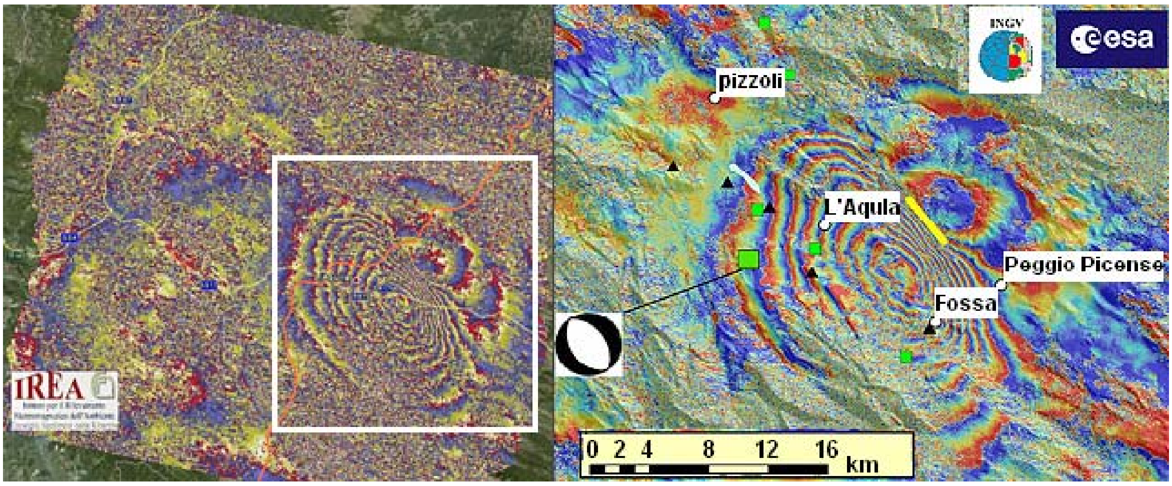

Figure 2.19 Italy earthquake, April 6th, 2009 (URL 4).

Table 2.9 ENVISAT system characteristics (continues at the next page).

Lifetime of satellite	5 years
Total Mass	8200 kg
Length	25 m
Orbital characteristics	Sun-synchronous, 800km altitude, 98º inclination, 10 a.m descending node, 35 day repeat cycle, period 100.6 minutes
Data transmission speed	2 × 100 Mbit/s
Sensors	Advanced Synthetic Aperture Radar (ASAR) Medium-spectral Resolution Imaging Spectrometer Instrument (MERIS)

ENVISAT has other instruments beside sensors for imaging: AATSR (advanced along track scanning radiometer), RA-2 (radar altimeter 2), MWR (microwave radiometer), GOMOS (global ozone monitoring by occultation of stars) for measuring atmospheric constituents, MIPAS (Michelson interferometer for passive atmospheric sounding), SCIAMACHY (scanning imaging absorption spectrometer for atmospheric cartography), DORIS (Doppler orbitography and radio-positioning integrated by satellite) and a passive device LRR (Laser Retro-Reflector) which is used as a reflector by ground-based SLR (Satellite Laser Ranging) stations using high-power pulsed lasers. Figure 2.20 illustrates the structure of ENVISAT.

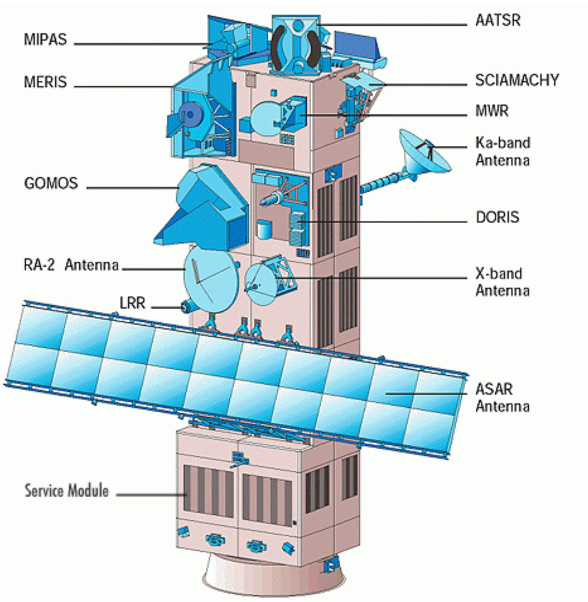

Figure 2.20 Structure of ENVISAT (URL 5).

As it can be seen in Table 2.9, ENVISAT has two types of sensors. ASAR is operated in C-band and provides continuity with wave mode and imaging mode of ERS-1/2 AMI (Active Microwave Instrument). ASAR offers features like polarization. Incidence angle range and coverage area of ASAR are shown in Table 2.10.

Table 2.10 Characteristics of ASAR.

Mode	**Spatial resolution**	**Swath width**	**Polarization combinations**
Imaging mode	30m	100km	VV/HH
Variable polarization mode	30m	100km	HH/VV, HH/HV, VV/VH
Wide swath area	150m	400km	HH/VV

MERIS has several spectral bands, used for measuring the color of water surfaces for regulation of fishery and coastal zone, determining thermal regime of ocean and carbon conversion. MERIS sensor also enables to measure cloud heights, water vapor and fume over land-cover. The bands of MERIS have 290 m x 260 m full and 1.2 km x 1.04 km reduced ground resolution.

2.3.4 Europen Remote Sensing Satellite- 1/2 (ERS- 1/2)

ERS-1

The first European radar altimeter carrier satellite European Remote Sensing satellite (ERS-1) was launched to space by ESA on July 17th, 1991 from Kourou Space Center in French Guiana by Ariane launch vehicle. ERS-1 has the components below (Figure 2.21) and used for collecting SAR data from the Earth's land surfaces, oceans, polar caps and monitoring natural disasters as earthquakes and floods.

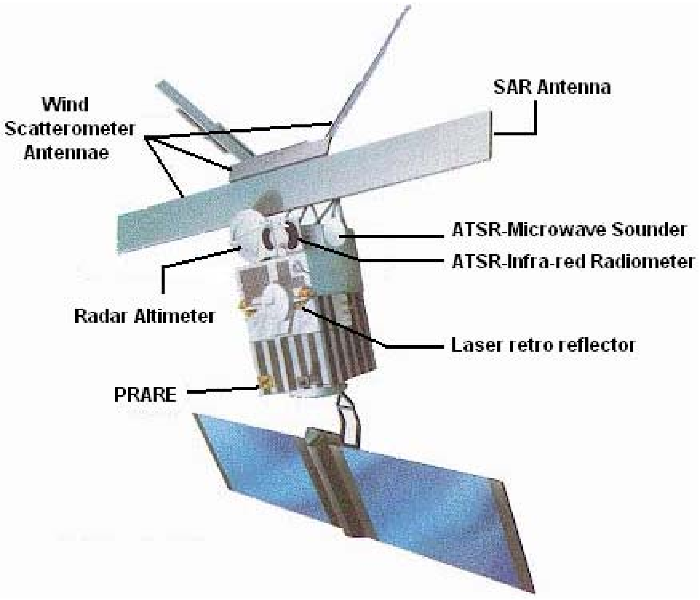

Figure 2.21 Components of ERS-1 (URL 4).

ERS-1 C-band (6cm wavelength) data were used in several topographic terrain mapping applications. The VV polarization SAR instrument has high sensitivity to terrain surface features. This SAR instrument was a part of AMI with a windscatterometer. ERS-1 AMI-SAR are divided into two modes; imaging and wave. The data collection types of these modes are shown in Figure 2.22 and the characteristics of ERS-1 satellite are shown in Table 2.11.

The PRARE positioning system of the satellite broke down shortly after launch and ERS-1 precise orbits were determined by Satellite Laser Ranging (SLR) technique which is used to calibrate the radar altimeter.

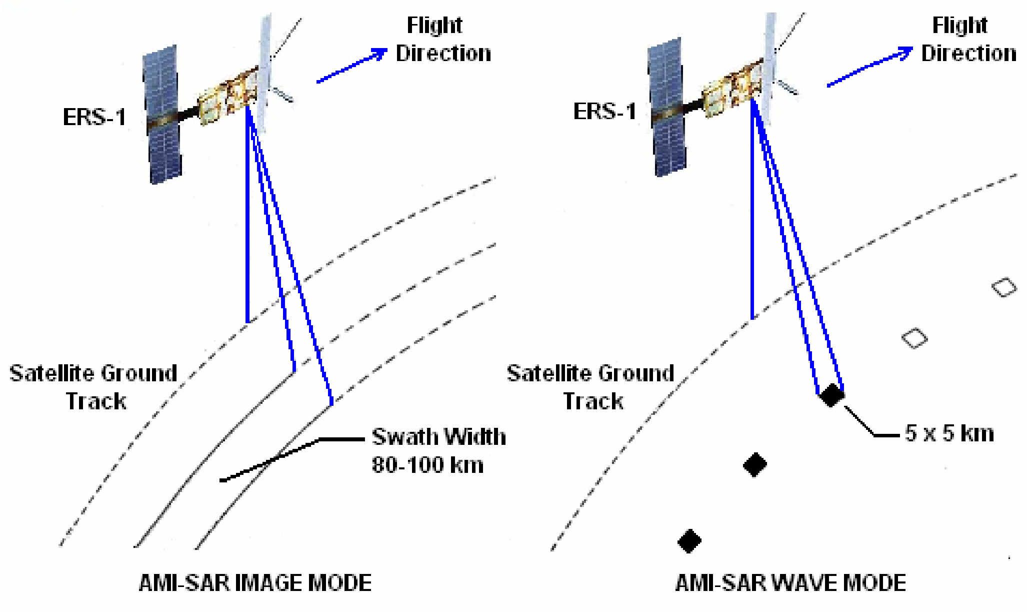

Figure 2.22 Data collection types of ERS-1 AMI-SAR.

Table 2.11 Characteristics of ERS-1 and AMI-SAR sensor modes.

Mass	2157 kg	
Orbital characteristics	Sun-synchronous near-circular polar, 785 km altitude, Inclination: 98.52° , 100 minutes period, 14.3 orbits per day, 3 day, 35 day and 176 day repeat cycle	
Instruments	AMI; SAR and Wind Scatterometer (WS); Radar Altimeter (RA), Along Track Scanning Radiometer (ATSR), Precise Range and Range-rate Equipment (PRARE) and LRR	
Characteristics of AMI-SAR sensor modes		
Parameters	**Image mode**	**Image mode**
Frequency	5.3 GHz	5.3 GHz
Swath wide	80-100km	80-100km
Spatial resolution	below 30m	below 30m
Incidence angle	23°	23°
Initial repeat cycle	3 days	3 days
Polarization	VV	VV

After obtaining more than 1.5 million individual SAR images have been captured. The mission was terminated at March 10th, 2000 by a failure in the on board attitude control system.

ERS-2

ERS-2 was launched on April 21st, 1995 by ESA from Kourou Space Center in French Guiana with Ariane launch vehicle like ERS-1. The satellite is the successor of ERS-1 and has the same group of instruments with the addition of the Global Ozone Measuring Equipment (GOME) which measured ozone distribution in the outer atmosphere. The system components of ERS-2 are shown in Figure 2.23 As with ERS-1, the satellite data are used for the observations of land surface, ocean, ice and atmosphere (climate changing, air-pollution, assessment of ozone layer etc.).

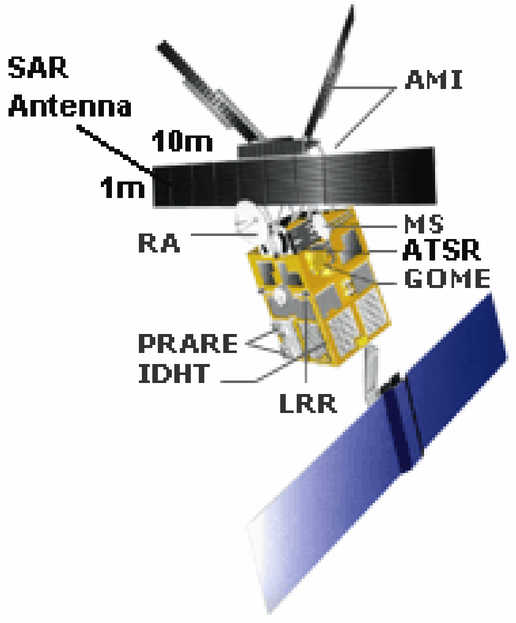

Figure 2.23 System components of ERS-2.

ERS-2 has nearly same system characteristics (orbital, sensor etc.) with ERS-1, just 360 kg heavier. The satellite has been producing useful results for more than 13 years. Both ERS-1 and ERS-2 operated TanDEM during nine months in 1995-1996 and provided 3-D digital map of the Earth for scientific use.

2.3.5 RADARSAT-1/2

RADARSAT-1

RADARSAT-1 is Canada's first commercial Earth observation satellite and a project of Canadian Space Agency (CSA). It was launched at November 4th, 1995 from Vandenberg AFB in California, USA its expected lifetime was 5.25 years. The purpose of satellite was producing data for environmental change monitoring and support natural resources sustainability. The RADARSAT-1 data are useful in agriculture, geology, forestry, cartography, hydrology, oceanography, ice and ocean monitoring etc. The system components of the satellite are shown in Figure 2.24.

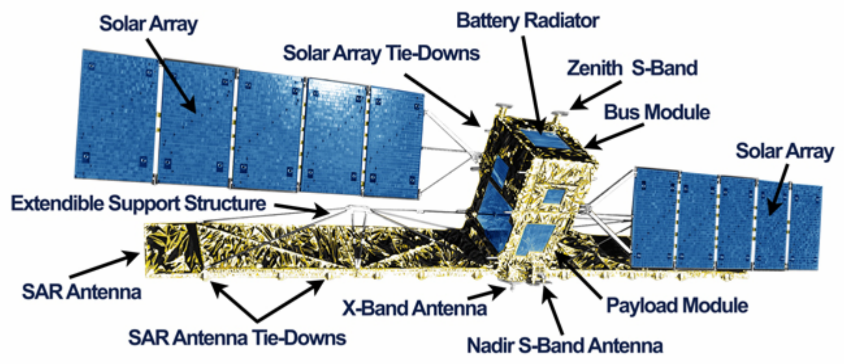

Figure 2.24 System components of RADARSAT-1 (URL 6).

RADARSAT-1 has an active microwave C-band SAR sensor on board which enables imaging in all times of a day and all weather conditions and provides image data of the Earth with 50 to 500km swath width and 8-100m ground resolution depending upon the 7 modes and 35 beam positions. The C-band SAR characteristics of the satellite can be seen at the Table 2.12.

Table 2.12 RADARSAT-1 SAR characteristics.

Radar frequency	5.3 GHz
RF band width	11.6, 17.3 or 30.0 MHz
Wavelength	5.6 cm
Incidence angle	10-59°
Polarization	HH

Figure 2.25 shows the swath widths and resolutions of 7 beam modes according to their elevation angles and profiles.

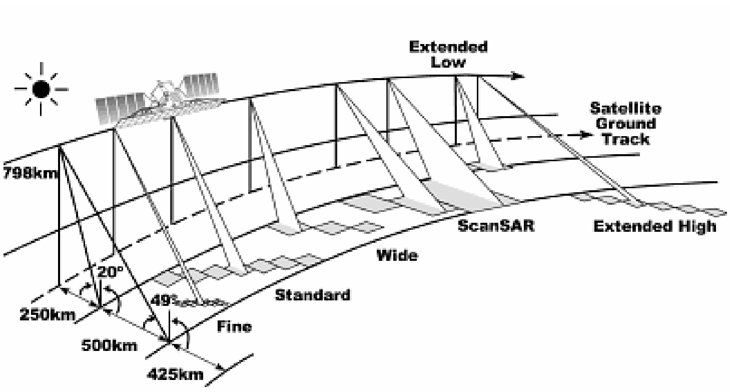

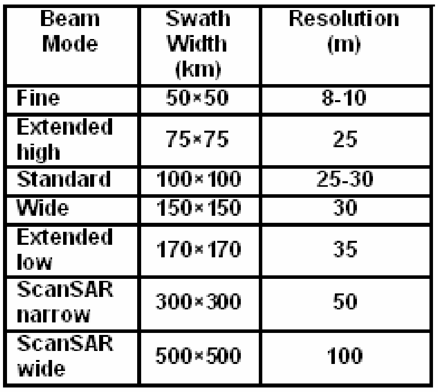

Beam Mode	Swath Width (km)	Resolution (m)
Fine	50×50	8-10
Extended high	75×75	25
Standard	100×100	25-30
Wide	150×150	30
Extended low	170×170	35
ScanSAR narrow	300×300	50
ScanSAR wide	500×500	100

Figure 2.25 RADARSAT-1 SAR beam modes (URL 7).

RADARSAT-2

RADARSAT-2, Canadian second commercial satellite was launched on December 14th, 2007 on a Soyuz vehicle from Russia's space launch facility, Baikonur Cosmodrome in Kazakhstan. Its expected lifetime is at least 7 years. It is a joint project between CSA, Macdonald, Dettwiler and Associates Ltd. (MDA). RADARSAT-2 has some advantages against RADARSAT-1 in terms of technical specification. Be different than RADARSAT-1, the satellite offers 3m high resolution left-right selectable looking imaging, several polarization modes, superior data storage etc. The system components of RADARSAT-2 are shown in Figure 2.26 and the characteristics of the satellite can been seen in Table 2.13.

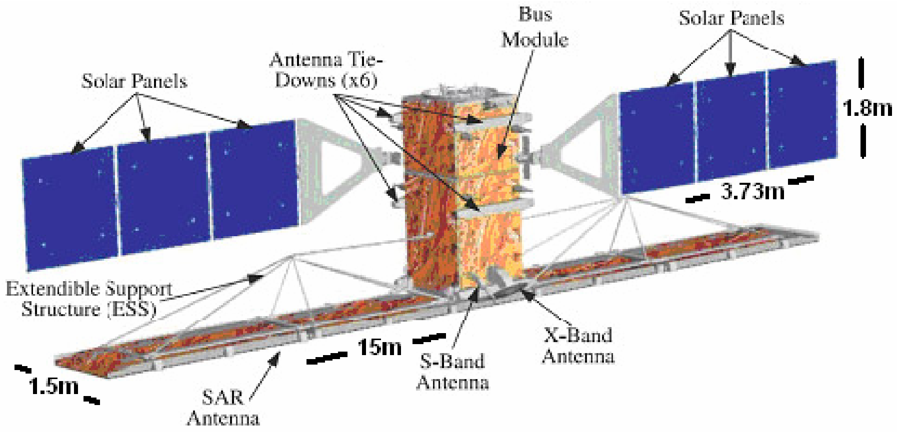

Figure 2.26 System components of RADARSAT-2 (URL 7).

Table 2.13 Characteristics of RADARSAT-2.

Weight	2200 kg
Orbital characteristics	Sun-synchronous near-polar, 798km altitude, 98.6° inclination, 100.7 minutes period, 24 days repeat cycle and 14 orbits per day
Repeat cycle	With 500km swath north of 70° (daily), north of 48° (every 1-2 days), equator (every 2-3 days)
Sensors	C-band SAR (1.5m×15m)
SAR sensor characteristics	
Frequency	5.405 GHz
Bandwidth	11.6, 17.3, 30, 50 or 100 MHz
Polarization	HH, HV, VH, VV

RADARSAT-2 has in total 12 imaging modes and 5 imaging modes in addition to RADARSAT-1. The satellite offers 3m resolution in ultra-fine modes in 30-40° incidence angle and 10-20km swath width. The imaging modes are shown in Figure 2.27.

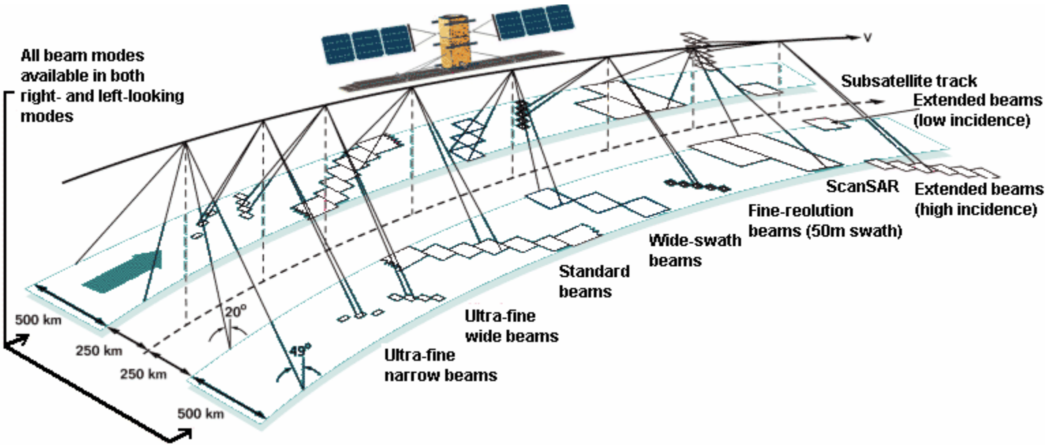

Figure 2.27 Imaging modes of RADARSAT-2.

The characteristics of these imaging modes are arranged according to their approximate resolution in Table 2.14.

Like RADARSAT-1, RADARSAT-2 is constructed for environmental monitoring application and sustainability of natural resources of the Earth. The satellite data are used for agriculture, forestry, geology, hydrology, ice and marine surveillance, mapping and disaster management.

Table 2.14 Imaging modes of RADARSAT-2.

Beam Mode	**Nominal Swath width (km)**	**Swath Coverage to left or right of ground track (km)**	**Approximate Ground Resolution Rg x Az (m)**
Ultra-Fine Narrow	10	400 - 550	3 x 3
Ultra-Fine Wide	20	400 - 550	3 x 3
Fine	50	525 - 750	10 x 9
Fine Quad-Pol	25 - 50	400 - 600	11 x 9
Triple Fine	50	400 - 750	11 x 9
High inc.	70	750 - 1000	20 x 28
Standard	100	250 - 750	25 x 28
Standard Quad-Pol	25 - 50	250 - 600	25 x 28
Wide	150	250 - 650	25 x 28
Low inc.	170	125 - 300	40 x 28
ScanSAR Narrow	300	250 - 600	50 x 50
ScanSAR Wide	500	250 - 720	100 x 100

2.3.6 Japanese Earth Resources Satellite-1 (JERS-1)

The Japanese Earth Resources Satellite-1 (JERS-1) was launched on February 11th, 1992 build by Japanese National Space Development Agency (NASDA) which was responsible for the spacecraft, by the Ministry of International Trade and Industry (MITI), which developed the measuring instruments, and by the Science and Technology Agency (JST) for purposes of mapping topography and geological characteristics of Earth's surface, environmental protection, forestry, fishery, disaster observation and coastal line monitoring. But unfortunately after obtaining data during 6 years, a malfunction occurred at the satellite on October 11, 1998. The satellite structure is shown in Figure 2.28.

JERS-1 used a high-performance HH-polarization L-band (23cm) SAR and two Optical Sensors (OPS). OPS comprised 3-band CCD, collected information from eight spectral bands at the visible, near infrared (VNIR) and short wave infrared (SWIR) and has stereoscopically observation capability for determining stones, rocks and minerals. Characteristics of JERS-1, its SAR sensor and OPS can be seen in Table 2.15 below.

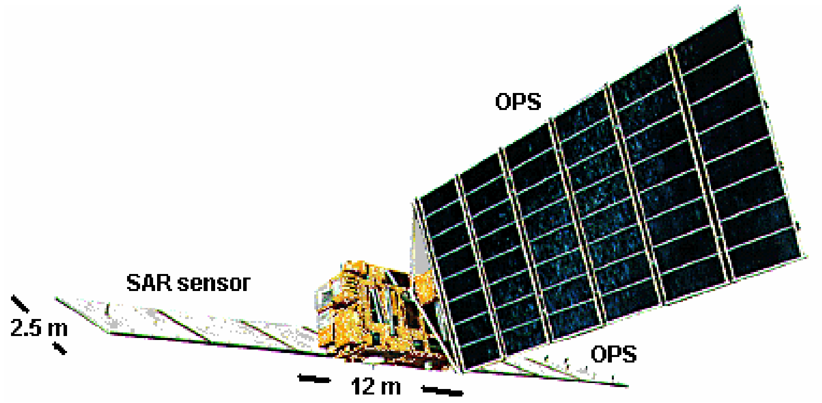

Figure 2.28 Structure of JERS-1 (URL 8).

Table 2.15 Characteristics of JERS-1 and its sensors.

Weight		1340 kg	
Launch site and vehicle		Tanegashima Space Center (Japan), H-I vehicle	
Orbital characteristics		Sun-synchronous solar, altitude 568km, inclination 98.5 °, repeat period 44 days	
Sensors		SAR, OPS	
SAR (12m×2.5m)		**OPS**	
Resolution	18m	**Resolution**	18m
Swath width	75km	**Swath width**	75km
Band name	L-band	**Band name**	L-band
Radar freq.	1,275 GHz	**Radar freq.**	1,275 GHz
Band width	15 MHz	**Band width**	15 MHz
Wavelength	235 mm	**Wavelength**	235 mm
Polarization	HH	**Polarization**	HH

2.3.7 Advanced Land Observing Satellite (ALOS)

The Advanced Land Observing Satellite (ALOS) was built by Japan Aerospace Exploration Agency (JAXA) and launched on January 24th, 2006 from Tanegashima Space Center, Japan.

The satellite has three basic components for data acquisition. These are; panchromatic remote sensing instrument for stereo mapping (PRISM), advanced visible and near infrared radiometer- type two (AVNIR-II) and phased array type L-band synthetic aperture radar (PALSAR). The configuration of ALOS is shown in Figure 2.29.

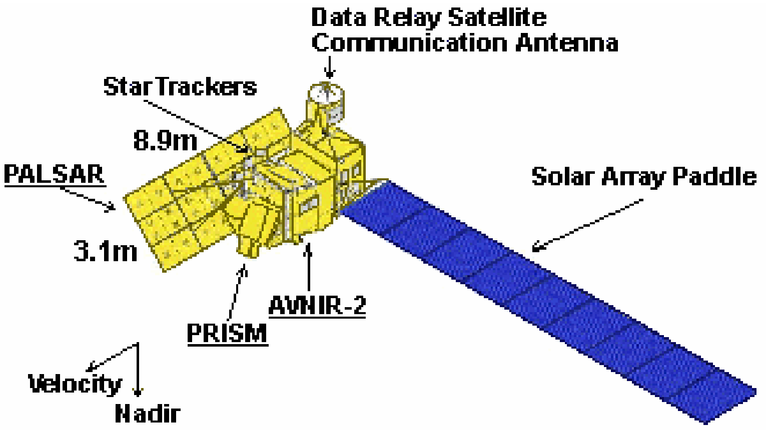

Figure 2.29 Configuration of ALOS (URL 8).

The characteristics of the satellite are shown in the Table 2.16.

Table 2.16 Characteristics of ALOS.

<table>
<tr><td colspan="2">Weight</td><td colspan="2">≈ 4000 kg</td></tr>
<tr><td colspan="2">Launch site and vehicle</td><td colspan="2">Tanegashima Space Center (Japan),
H-II A vehicle</td></tr>
<tr><td colspan="2">Orbital characteristics</td><td colspan="2">Sun-synchronous orbit, altitude 691.65km, inclination 98.16^o, repeat period 46 days, sub cycle 2 days</td></tr>
<tr><td colspan="2">Lifetime</td><td colspan="2">3-5 years</td></tr>
<tr><td colspan="2">On-board instruments</td><td colspan="2">PRISM, AVNIR II, PALSAR</td></tr>
<tr><td></td><td>PRISM</td><td></td><td>PRISM</td></tr>
<tr><td>Spatial resolution</td><td>2.5 m</td><td>Spatial resolution</td><td>2.5 m</td></tr>
<tr><td>Swath width</td><td>35 km (triple mode)
70 km (nadir only)</td><td>Swath width</td><td>35 km (triple mode)
70 km (nadir only)</td></tr>
</table>

For the PALSAR generation, the Japan Resources Observation System Organization (JAROS) of MITI cooperated with JAXA. JAXA started to antenna deployment operation for PALSAR on ALOS satellite on January 26th, 2006. PALSAR uses repeat-pass Interferometry. It is an active microwave sensor which enables data acquisition in whole day independent on cloud coverage and offers higher performance against JERS-1 SAR. PALSAR cannot achieve data from the areas beyond 87.8º north latitude and 75.9º south latitude when the off-nadir angle is 41.5º.

The PALSAR data are used for atmospheric temperature, snow and ice determination, forestry, agriculture and disaster monitoring.

PART 3

INTERFEROMETRIC PROCESSING AND DSM GENERATION

Interferometric processing and related DSM generation using TerraSAR-X InSAR images is one of the main topic of this study. DSM generation from SAR images is not a simple manner like generation from optical imagery. Interferometric processing has several complicate steps for the production of a DSM. The quality of the data set and used software package are important for the stability of the generated DSM. In this section, at first the InSAR data sets, later on software packages and interferometric processing steps for DSM generation are explained.

3.1 INSAR DATA SETS

As mentioned before, TSX InSAR images are used for DSM generation. Istanbul, Turkey is chosen as test area because of its location, importance for Turkey and topographic characteristics (rolling, hilly mountainous, forest etc.). The test field should contain steep areas and forest besides flat regions to show the InSAR capability. The radar satellite TSX has single look complex data type and uses repeat-pass interferometry for the DSM generation.

In this study, two different operation modes of TSX (SM and high resolution SL) and two SAR image-pairs (four SAR images) corresponding with them have been used for the DSM generations for Istanbul. Firstly, two TSX SM InSAR images taken in one month interval are used for interferometric processing. The images and their characteristics are shown in following Figure 3.1 and Table 3.1.

Secondly, two high resolution TSX SL InSAR images taken with five months interval are used for interferometric processing. The images and their characteristics are shown in Figure 3.2 and Table 3.2.

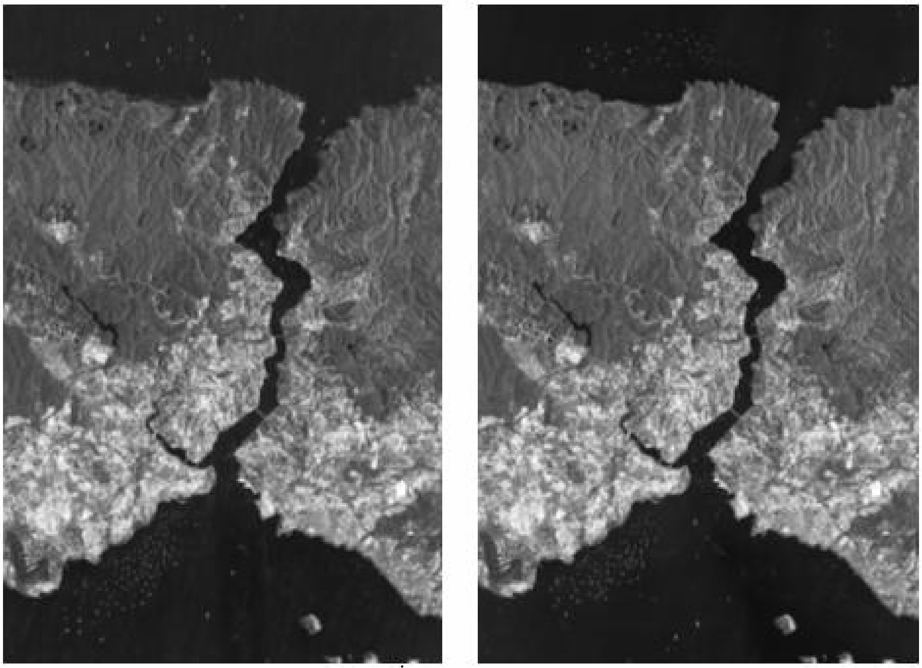

Figure 3.1 Istanbul TSX SM InSAR images.

Table 3.1 Characteristics of TSX SM InSAR images.

Characteristics	**TSX SM Image 1**	**TSX SM Image 2**
Sensor Id	SAR	SAR
Sensor mode	Stripmap	Stripmap
Start date	2008-02-11T04:10:31,531	2008-03-15T04:10:31,957
End date	2008-02-11T04:10:38,077	2008-03-15T04:10:38,504
Polarization mode	Single polarization	Single polarization
Polarization channel	HH	HH
Looking direction	Right looking	Right looking
Pass direction	Descending pass	Descending pass
Centre incidence angle	41.0967077832301	41.0932590666749
Length and width of scene	40km×30km	40km×30km

From the theoretical point of view, the InSAR technique is assumed to generate DEMs with an accuracy in the order of a few meters (Coulson 1993) depending upon the quality of SAR data sets. The most actual, latest technology and high quality InSAR images acquired by SM and high resolution SL modes of TSX were used in this study. Especially 1m azimuth resolution offered by high resolution TSX SL mode could not be seen before in SAR applications.

Figure 3.2 High resolution TSX SL InSAR images.

Table 3.2 Characteristics of high resolution TSX SL InSAR images.

Characteristics	**HR TSX SL Image 1**	**HR TSX SL Image 2**
Sensor Id	SAR	SAR
Sensor mode	High resolution Spotlight	High resolution Spotlight
Start date	2008-05-05T15:57:33,985	2008-10-06T15:57:42,522
End date	2008-05-05T15:57:34,738	2008-10-06T15:57:43,262
Polarization mode	Single polarization	Single polarization
Polarization channel	HH	HH
Looking direction	Right looking	Right looking
Pass direction	Ascending pass	Ascending pass
Centre incidence angle	40.9752891207	41.0898290780
Length and width of scene	5km×10km	5km×10km

During the study, the TSX SM InSAR image which was acquired in 11/02/2008 will be named as TSX SM image 1 and second TSX SM InSAR image acquired in 15/03/2008 will be named as TSX SM image 2. Likewise, the higher resolution TSX SL InSAR image which was acquired in 05/05/2008 will be named as TSX SL image 1 and second high resolution TSX SL InSAR image acquired in 06/10/2008 will be named as TSX SL image 2.

3.2 PROGRAMS FOR RADAR IMAGE PROCESSING AND DEM GENERATION

In the study, interferometric processing steps of the SARscape module included by the common remote sensing software package ENVI version 4.6 has been preferred for the registration of TSX SAR image-pairs and generation of interferograms and height models derived from them.

3.2.1 ENVI Version 4.6

The remote sensing software package ENVI version 4.6 is created by International Telephone & Telegraph Visual Information Solutions (ITT VIS) in 2008. ENVI is the premier software solution for processing and analyzing geospatial imagery and combines the latest spectral image processing and image analysis technology (URL 9). ENVI has several tools for remote sensing applications shown in Figure 3.3.

Figure 3.3 General tools of program ENVI.

Besides SARscape, most of modules of ENVI 4.6 were used for the interferometric processing and DEM generation as basic tools, map tool, topographic tool, radar tool etc.

3.2.2 SARscape

In this project the SARscape module of ENVI version 4.6 was used for whole interferometric processing and DSM generation. It is a powerful module that allows processing and analysis of SAR data using several sub-modules.

When starting interferometric processing, first two InSAR images are imported by definition of data formats, sensors, data types and reference extensible markup language (xml) parameter files to the program using basic sub-module and the application steps below were applied in sequentially up to DSM generation.

3.3 PROCESSING STEPS OF DSM GENERATION

As mentioned before, interferometric processing steps of DSM generation are not as simple as DSM generation with optical imagery. The operator has to apply several complex steps and assign threshold application values depending up on quality and characteristics of the SAR images which are used for DSM generation (e.g. co-registration settings, best choice of azimuth and range looks etc.). In this section, sequentially, image registration, baseline estimation, interferogram generation along with co-registered single look complex (SLC) generation, flattening, filtering and coherence generation, phase unwrapping, orbital refinement, phase to height conversion and geocoding steps are performed step by step and DSMs of TSX SAR image-pairs are obtained.

3.3.1 Baseline Estimation and Co-registration

Co-registration is one of the main mandatory issues of the whole interferometric processing. It includes several settings important for satisfying co-registration. The operator has to be careful because it is one of the most critical and time consuming processing steps.

.

Co-registration is in the question when at least two SAR images have similar acquisition geometry. Like the process of superimposing, in the slant range geometry, for getting a correspondence with sub-pixel accuracy, the fitting of the slave image to the reference master image is required for further interferometric processing. The co-registration consist of two steps: the change of the location of each pixel in the slave image with respect to the master image, and the recalculation of the amplitude and phase information of the phasor by interpolation for each pixel of the slave image (Gens 1998).

In this study the co-registration was automatically done during interferogram generation after the determination of master and slave images. During the processing with TSX SM, the TSX SM image 1 was preferred as master and TSX SM image 2 was used as slave image and according, for the processing with TSX SL, the TSX SL image 1 was preferred as master and TSX SL image 2 as slave image. Before co-registered of single look complex, the baseline between master and slave image and relevant parameters has to be estimated. For this application the baseline estimation tool was used in the SARscape interferometry module. The results of TSX SM and TSX SL image-pairs are shown in the Tables 3.3 and 3.4.

Table 3.3 Baseline estimation between TSX SM master and slave images.

Baseline estimation Parameters	**Values**
Normal baseline (m)	44.71
Critical baseline (m)	5256.24
2 PI (π) ambiguity height (m)	139.97
Range Shift (pixels)	-50.76
Azimuth Shift (pixels)	3.85
Doppler centroid difference (Hz) (Critical : 3514.78)	-5.376

Table 3.4 Baseline estimation between TSX SL master and slave images.

Baseline estimation Parameters	**Values**
Normal baseline (m)	136.21
Critical baseline (m)	15770.57
2 PI (π) ambiguity height (m)	45.95
Range Shift (pixels)	-2030.48
Azimuth Shift (pixels)	618.91
Doppler centroid difference (Hz) (Critical : 8300.00)	154.00

The normal baseline is the perpendicular baseline between the master and slave orbit, this value is important for further interferometric processing. When the magnitude of normal baseline exceeds the changeable threshold values corresponding to the master and slave images, it evokes increased noise at the interferogram proportional to normal baseline value, complicating the description of the topography and DSM generation. Consequently the optimal normal baseline has a serious effect at the final interferometric product. In any case the critical baseline should not be exceeded otherwise interferometric processing is impossible. The 2π ambiguity height represents the height difference concerned with an interferometric fringe (2π cycle) and increase of this value obstructs the definition of small height changes. The range and azimuth shifts will be applied in range and azimuth direction during the master-slave coarse co-registration. Figure 3.4 illustrates the range and azimuth shifts between master and slave images.

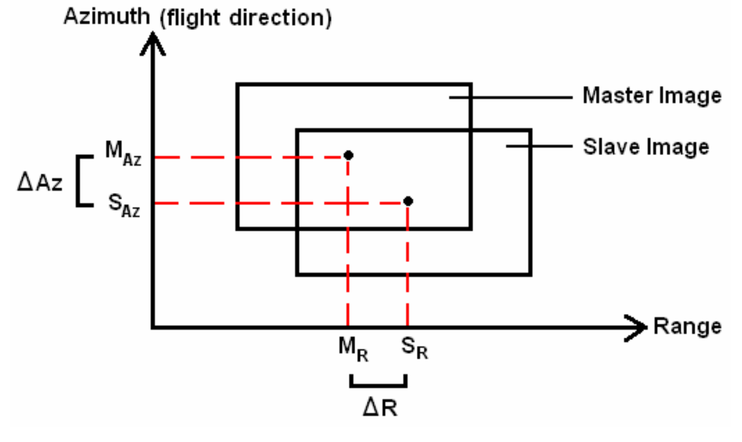

ΔAz= Shift in azimuth direction between master and slave images

ΔR= Shift in range direction between master and slave images

Figure 3.4 The range and azimuth shifts between master and slave images.

The difference between master and slave Doppler centroids is named as Doppler centroid difference (f_D). This value equals to 0 (zero) when the side look is 90º during the satellite travels on its flight direction (azimuth). Apart from that situation f_D continually has a value different from 0 and this value cannot exceed the pulse repetition frequency (critical value).

After baseline estimation process, at the co-registration step of ENVI SARscape module; master, slave images and an old DEM of test area (see part 3.3.2 for detailed information) are inserted besides the arrangement of co-registration settings. And co-registered single look complex generation and resembling process are performed along with interferogram generation. At this step, before interferogram generation, it is essential to chose optimal values for the co-registration settings azimuth and range look. At the co-registration, these settings have to be calibrated; dependencies, grid positions and window numbers of range and azimuth, initialization from orbit, orbit accuracy and orbit interpolation value. For cross correlation central window, window sizes and central positions of range and azimuth have to be defined. For cross correlation grid, window sizes of range and azimuth and cross correlation threshold value have to be defined. Eventually, fine shift parameters; window sizes and window numbers of range and azimuth, cross correlation oversampling value, coherence oversampling value, reject threshold value and SNR (signal to noise ratio) threshold value have to be defined. The equation between SNR and coherence value is;

$$SNR = \gamma^2 / 1 - \gamma^2 \qquad (\gamma = \text{coherence}) \tag{3.1}$$

The relation between coherence and SNR will be explained more detailed in the coherence and filtering section.

3.3.2 Interferogram Generation

In single-pass or double-pass (repeat-pass) interferometry, two SAR data sets are achieved simultaneously or at different time using different look angles for the same interest area on ground. These data sets contain the phase as well as the magnitude of the backscattered radiation. Phase differences of two co-registered complex-valued SAR data sets of the same interest area are computed on a pixel-by-pixel base and an interferometric product is generated with the combination of them. This product is called an interferogram or a fringe map. Interferograms provide three dimensional visualization and topographic information be derived from fringes like contour lines. They are used for example, for disaster monitoring. Figure 3.5 illustrates the subsidence of approximately 20cm at L'aquila town, Italy after the magnitude 6.3 earthquake on April 6th, 2009. Two images from TSX were used, taken before and after the earthquake and the interferogram was created by combination of them.

In the study, besides master and slave images, DEMs derived from SPOT-5 HRS were used for the interferogram generation. Using a DEM (optional process) supporting the interferogram generation simplifies the fixation of a base cartographic system to the created interferogram. The azimuth and range look ratio is preferred as 3 after the evaluation of all contingent values for both TSX SM and TSX SL image-pairs.

During interferogram generation, spectral shift and common Doppler bandwidth filtering are performed. Spectral shift is needed due to the range spectra shift caused by the variable SAR viewing angle on distributed targets. The Doppler bandwidth filtering is required to compensate for different Doppler (squint angles), which produce shifted azimuth spectra. The azimuth filter applied during the interferogram generation enables to capture the scene's potential coherence (Sarmap 2008).

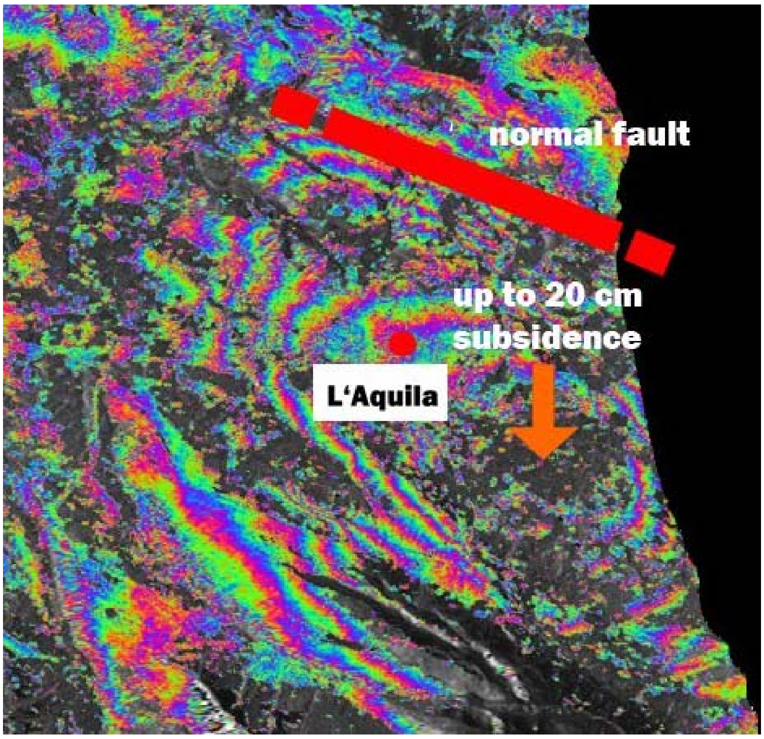

Figure 3.5 Interferogram of L'aquila earthquake by TSX images (URL 3).

After these applications, the generated interferogram from TSX SL SAR image-pair can be seen in Figure 3.6 with its color presentation to improve the visualization.

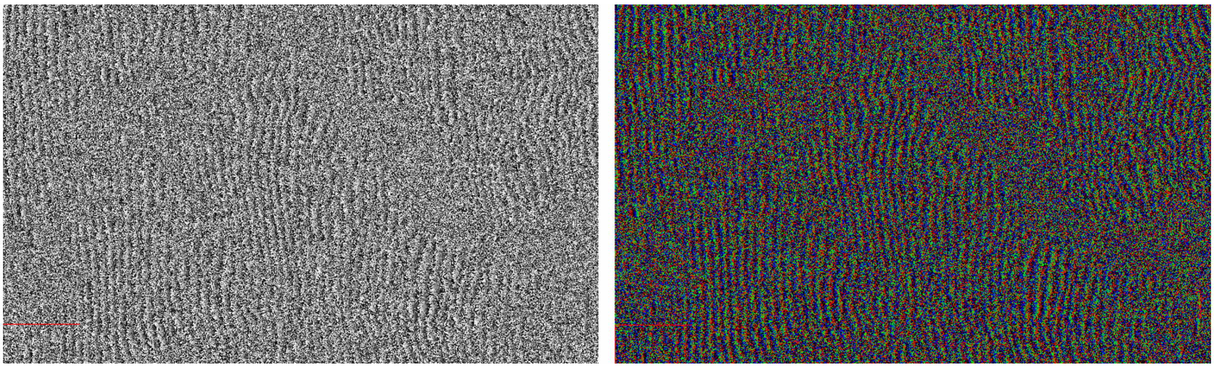

Figure 3.6 Interferogram of TSX SL image-pair.

3.3.3 Interferogram Flattening

After interferogram generation, before interferogram filtering several low frequent components can be removed using interferogram flattening which is the differential phase between the constant phase and the phase expected for a flat or a known topography. During this process can be supported by a coarse DEM. If a coarse DEM is used, flattening is performed by transforming this input DEM into the master slant range image geometry and synthetic fringes are generated from it, otherwise the shape of the Earth is assumed as an ellipsoid and ellipsoidal height is used as constant height. As mentioned before, in this study, SPOT-5 HRS DEM was used as coarse DEM at the interferometric processing steps. The interferogram flattening step is not a main step in DEM generation, it is just used to support the phase unwrapping process that's why at the end of interferogram flattening, the numbers of fringes are reduced. This process is executed fully automatic if the orbit and the input DEM is accurate. Figure 3.7 shows the flattened interferogram of TSX SM image-pair as an example after interferogram flattening.

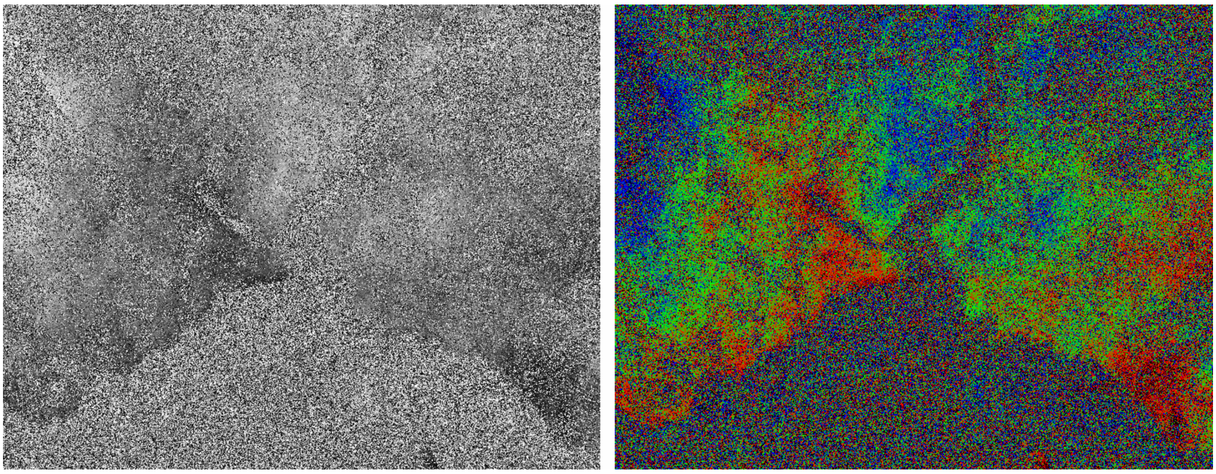

Figure 3.7 Flattened interferogram of TSX SM image-pair.

3.3.4 Coherence and Filtering

The interferometric coherence represents the stability of the backscattered SAR signal over an area of interest (Parcharidis et al. 2005). It can be summarized as a ratio between coherent and incoherent synopsis. Coherence maps are achieved via measuring pixel-to-pixel SNR and they expose the quality and reliability of an interferogram. Coherence maps are acquired by iterating the sampled estimator below for each pixel (k, h) of the co-registered master and slave images (s_M, s_s, respectively), after compensating for the estimate of local slopes (w_k, w_h) (Guarnieri et al. 2003).

$$\gamma(k,h) = \frac{\sum_{ij} S_M(k-i,h-j) S_S^{*}(k-i,h-j)\exp(j(W_k i + W_h j))}{\sqrt{\sum_{ij} \left|S_M(k-i,h-j)\right|^2 \left|S_S(k-i,h-j)\right|^2}} \tag{3.2}$$

The coherence ranges between 0 and 1 depending upon systematic spatial de-correlation and temporal de-correlation between master and slave image data and is a value for describing the quality of the DSM and thematic information extraction about the ground objects according to backscattering coefficient. The most important factor for coherence is time interval between master and slave images and changes of the imaged objects. Coherence is inversely proportional with time interval, that means, if the time interval between master and slave images increases, the coherence decreases depending upon the changes at the objects caused by season, climate etc. at the interest area.

For the generation of a coherence map, an interferogram or the filtered version of it can be used. The use of a filtered interferogram may be useful for higher coherence. Filters do not necessarily enhance or recover the radar signal but a powerful filter reduces noise, caused by temporal or baseline related de-correlation, changes the structure of the interferogram and improves fringe visibility.

In this study, an adaptive window and Goldstein filtering methods were used. Both filters were applied to the interferograms of TSX SM and TSX SL image-pairs. Figures 3.8 and 3.9 show the final TSX SM interferograms after adaptive and Goldstein filtering and Figures 3.10 and 3.11 illustrate the final TSX SL interferograms after adaptive and Goldstein filtering.

It can be seen clearly that the Goldstein filter is more powerful as the adaptive window filter for the interferograms generated here. It eliminates more noise and improves the interferogram interpretation. Therefore, the interferograms with Goldstein filtering are further used.

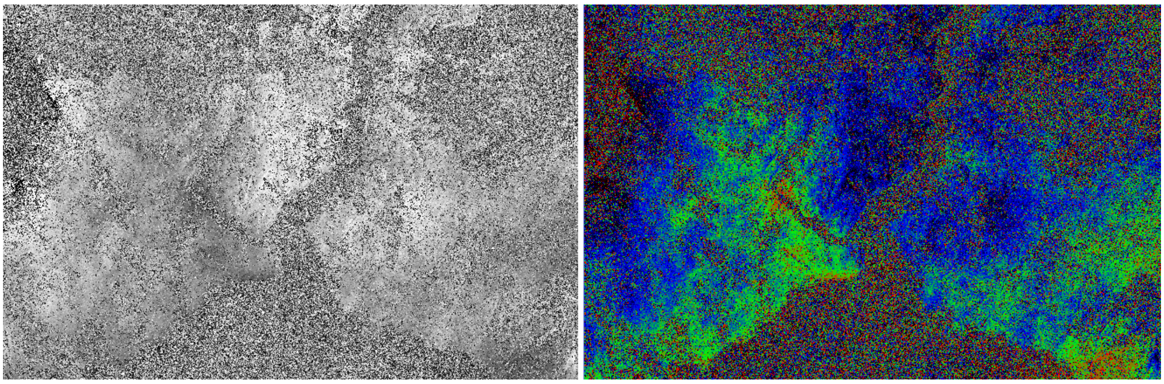

Figure 3.8 Final interferogram after adaptive filtering (TSX SM).

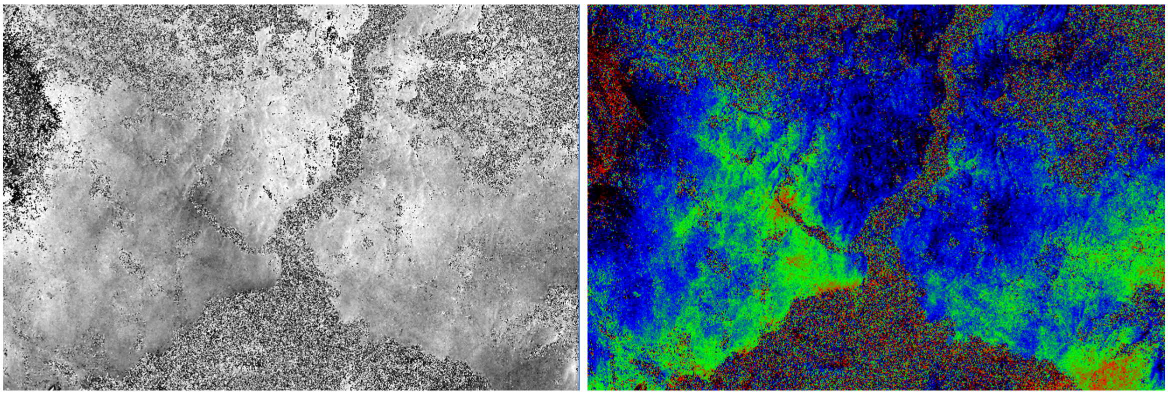

Figure 3.9 Final interferogram after Goldstein filtering (TSX SM).

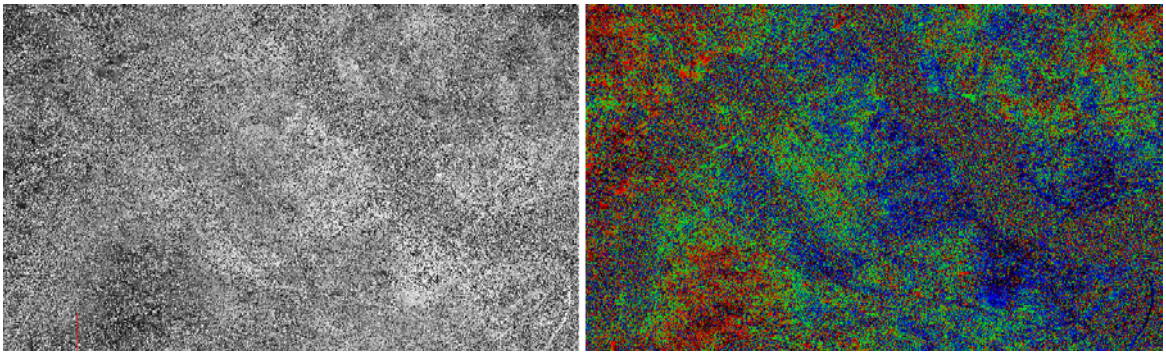

Figure 3.10 Final interferogram after adaptive filtering (TSX SL).

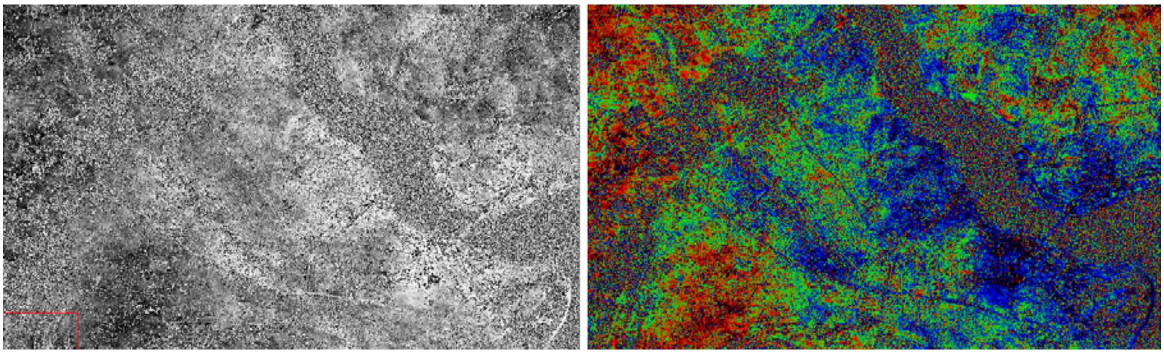

Figure 3.11 Final interferogram after Goldstein filtering (TSX SL).

The Goldstein filter was developed by R. M. Goldstein and C. L. Werner. It is an adaptive radar interferogram filter based on the concept of multiplication of the Fourier spectrum *Z(u,v)* of a small interferogram patch by its smoothed absolute value *S*{|*Z(u,v)*|} to the power of an exponent α:

$$H(u,v) = S\{|Z(u,v)|\}^{a} \times Z(u,v) \tag{3.3}$$

Where *H(u,v)* is the filter response (the spectrum of the filtered interferogram); *S*{ } is a smoothing operator; *u* and *v* are spatial frequencies; and 'a' is the filter parameter. Patches of the interferofram are defined and overlapped to prevent discontinuities at the boundaries. The filter parameter "a" is an arbitrarily chosen value between zero and one and has the largest impact on the filter performance. For the value of a = 0, the multiplication factor becomes one, and no filtering occurs. However, for large values of a , the filtering is significant (Baran et al. 2003).

After the selection of filtering method, coherence maps and spatial profiles concerning with filtered interferograms were generated. Figures 3.12 and 3.13 show the coherence maps of filtered TSX SM and TSX SL interferograms.

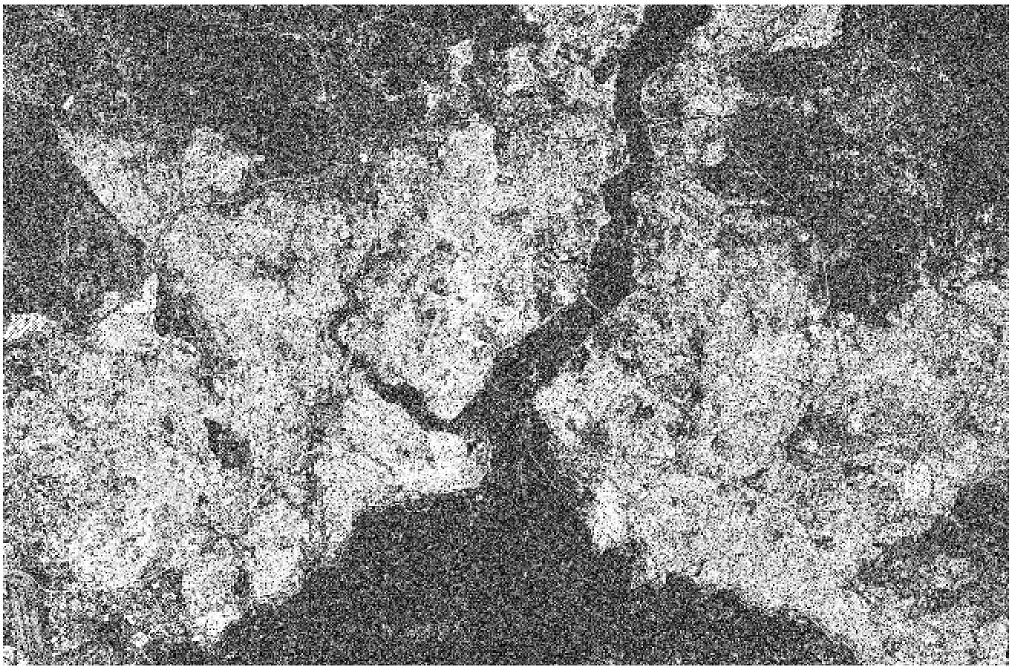

Figure 3.12 Coherence map of filtered TSX SM interferogram.

Figure 3.13 Coherence map of filtered TSX SL interferogram.

In preceding figures, the bright parts indicate the areas with higher coherence like flat areas and dark parts indicate the regions with lower coherence like sea, forest etc.

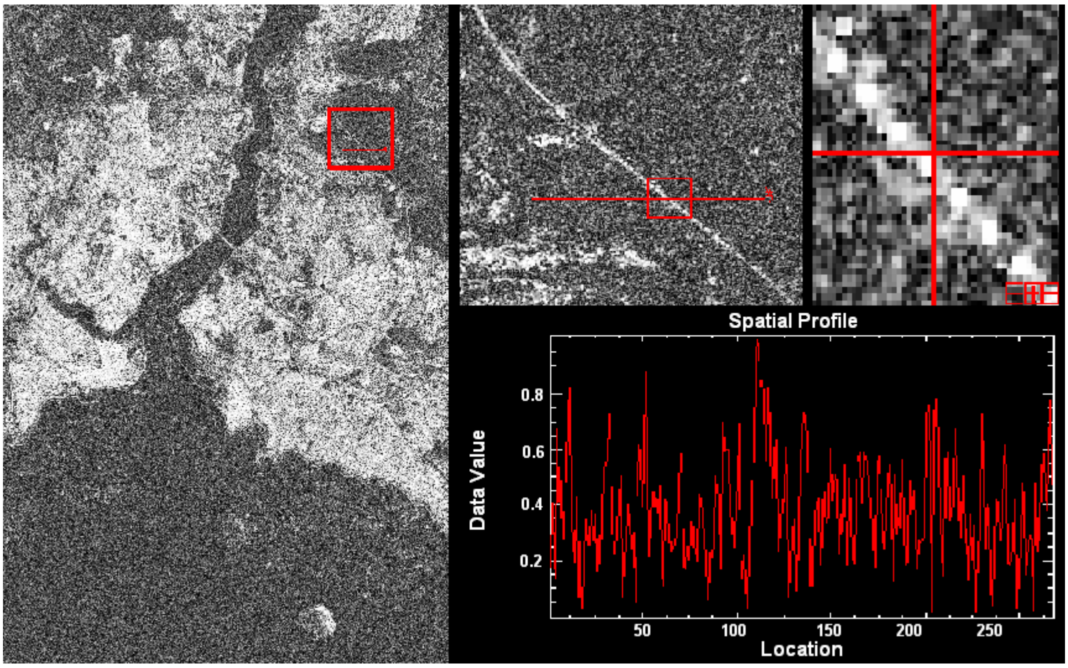

Figure 3.14 Zoom and spatial profile abilites on coherence map.

As it can be seen in Figure 3.14, a profile is selected as an example which passes over a road. In addition two separate zoom windows present details.

3.3.5 Phase Unwrapping

As known, SAR interferometry uses the phase differences of the microwave signals reflected from target objects to determine the surface topography. An interferometric phase value is unequivocal for 2π and as soon as passes every 2π value phase starts again and the cycle repeats itself. Because of this loop, a 2π ambiguity occurs. Accordingly, for the solution of this ambiguity, phase unwrapping process is used for the extraction of the absolute phase from the measured interferometric phase. Figure 3.15 shows the difference between wrapped phase and absolute phase.

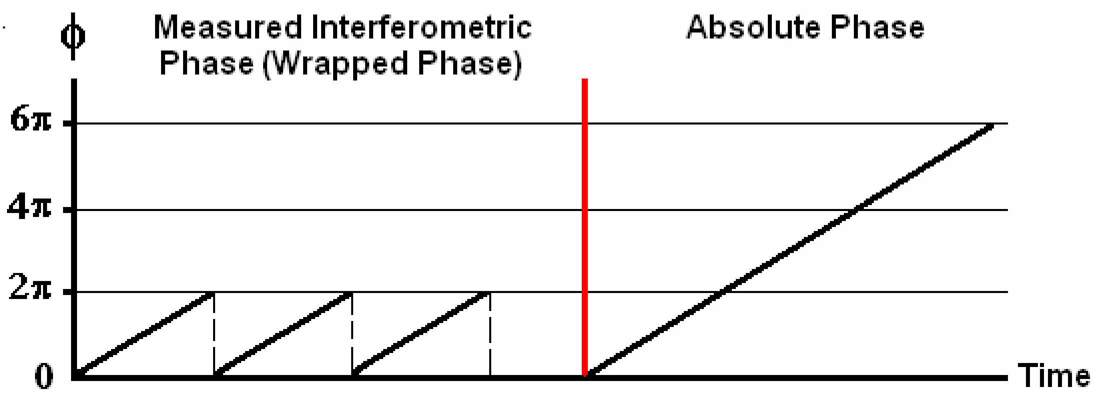

Figure 3.15 Difference between wrapped phase and absolute phase.

A simple formula can be written to show the relation between wrapped and unwrapped phase:

$$\psi = \phi \pm 2\pi k \tag{3.4}$$

Ψ = wrapped phase or principal interferometric phase ($-\pi \leq \Psi < +\pi$)

Φ = unwrapped phase or full cycle interferometric phase

k = 0,......, n

Phase unwrapping problems occur from aliasing errors due to phase noise by low coherence and under sampling phenomena because of locally high fringe rates (Reigber and Moreira

1997). For the solution of this problems several algorithms; region growing, minimum cost flow, multi-baseline, minimum least squares, etc. have been developed.

In this study, at the phase unwrapping step of interferometric processing, region growing and minimum cost flow algorithms were used with different decomposition level values. Based on the comparison of the different methods, the region growing method was selected with decomposition level 3. The region-growing method can be described in terms of two primitive operations: the translate operation, which adds/subtracts 2π to all points of a region, and the connect operation, which merges two areas. Starting from a condition of maximum fragmentation -each point constitutes a region- these two operations are executed iteratively on the active areas until no more joins can be done (Baldi 2003).

The phase unwrapping is one of the most important steps of interferometric processing and has a strong influence on the generated DSM. The operator can define a coherence threshold value for excluding lower coherence value by the program nevertheless several details may be lost and the operation might get illogical that's why the operator should be careful at the definitions for this step. Figure 3.16 shows an example for three different coherence threshold values applied to same interest area and their effects on the results of phase unwrapping process.

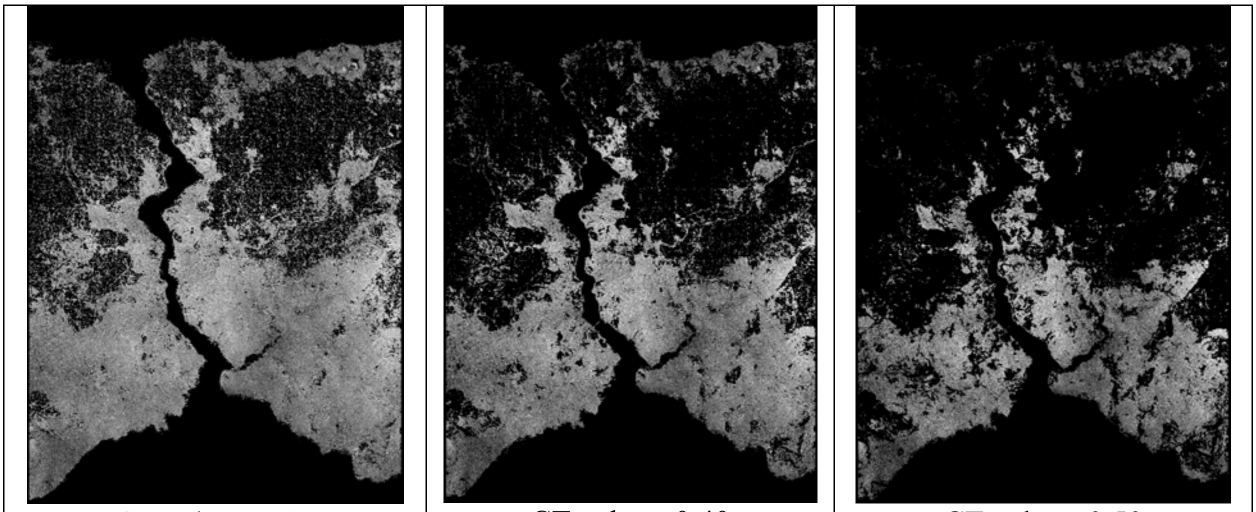

CT value= 0.35

CT value= 0.40

CT value= 0.50

Figure 3.16 Effect of coherence threshold (CT) value in phase unwrapping.

The resulting interferograms of TSX SM and TSX SL after phase unwrapping step can be seen together with their color coded results in Figures 3.17 and 3.18.

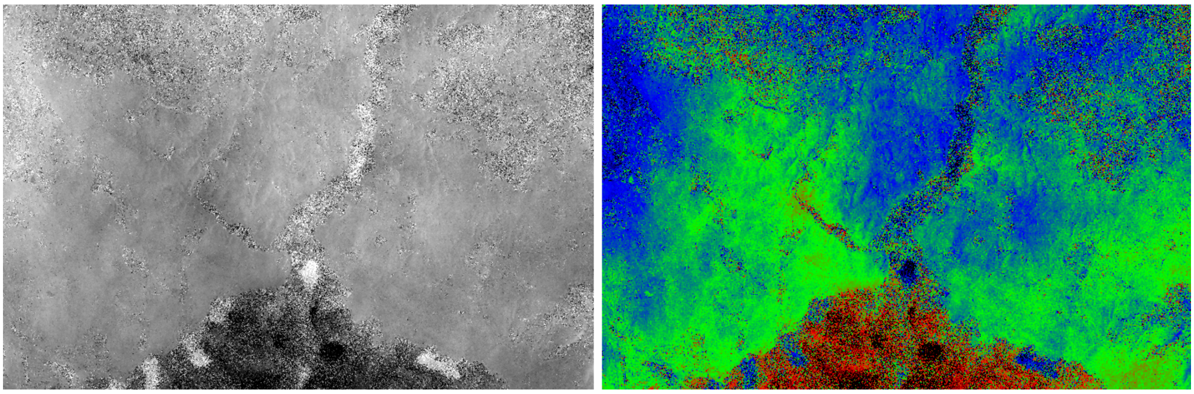

Figure 3.17 Interferogram of TSX SM after phase unwrapping.

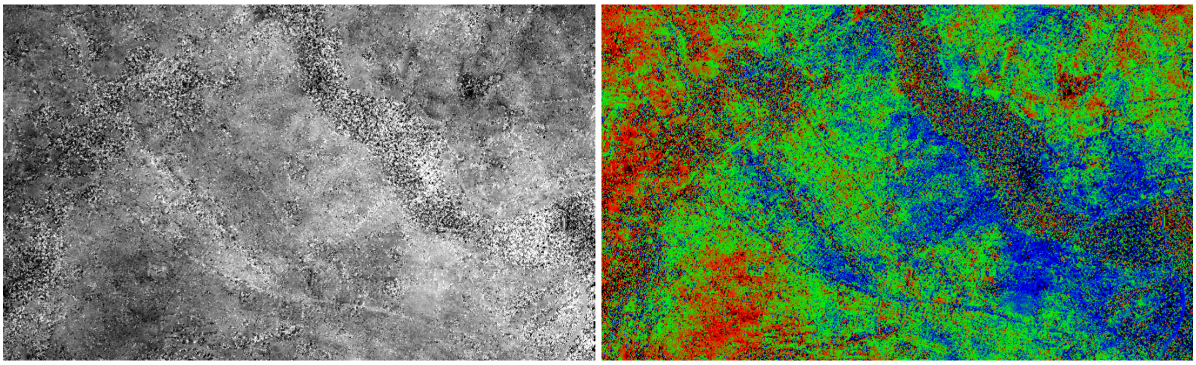

Figure 3.18 Interferogram of TSX SL after phase unwrapping.

3.3.6 Orbital Refinement

After phase unwrapping, orbital refinement should be performed before phase to height conversion. This step is essential for DEM generation. In fact the relation between the phase difference and the elevation is a function of the baseline and an accurate baseline is demanded for an accurate DEM. The baseline is initially estimated using the orbit information of the image header file and the orbital refinement improves the accuracy of the baseline value. In this process, besides refining of orbits, phase compensation is calculated using ground control points (GCPs) therefore it enables the absolute phase calculation. GCPs are compulsory for orbital refinement and have to be used for this step.

GCPs should be determined precisely. They should be located on flat and highly correlated areas (original DEM and correlation map can be used for this process) and if present the residual orbital fringes. According to the 7 parameter transformation, at least 7 GCPs are required but at least 10-12 GCPs should be used for a satisfying over determination. In this project, 12 GCPs were used for the orbital refinement of TSX SM and TSX SL interferograms. Figure 3.19 and 3.20 shows the GCP distribution.

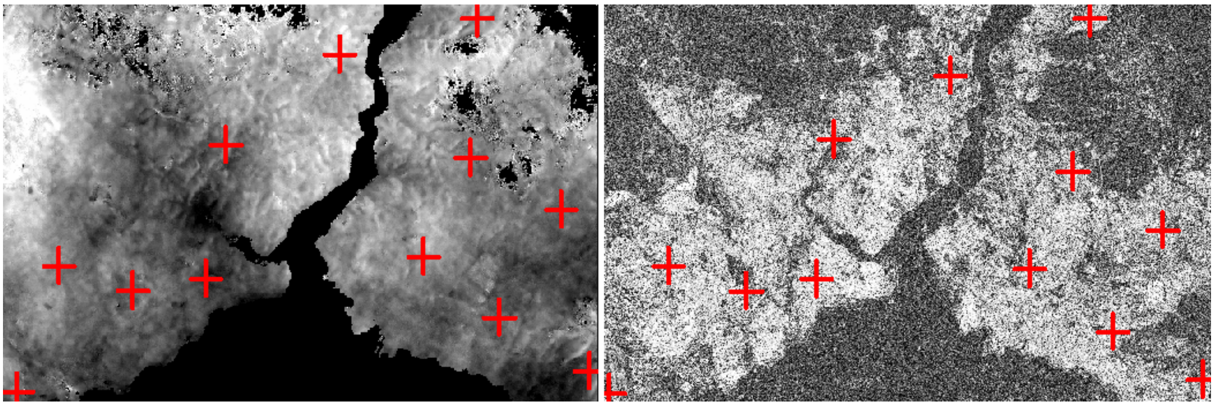

Figure 3.19 GCP distribution on TSX SM interferogram and coherence map.

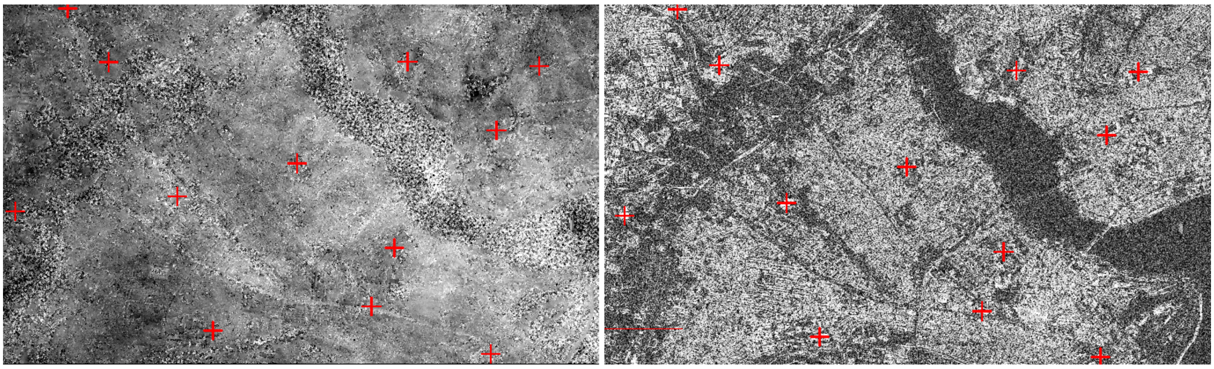

Figure 3.20 GCP distribution on TSX SM interferogram and coherence map.

As result of this orbital refinement, no new output file is generated because this is just a modification of the existing phase unwrapping header file (.sml) and this file is re-registered in itself. For checking the correction of the GCPs, in the modified phase unwrapping header file, 'BFRMSERROR' value can be examined. This value should be less than '10' after orbital refinement process. If not, it means GCPs are not well distributed and/or not accurate enough and have to be generated again.

3.3.7 Phase to Height Conversion and Geocoding

In this step, the generated phase values after phase unwrapping and orbital refinement are transformed into height values by phase to height conversion and the gridded DSM of the SAR data set is obtained. By the geocoding (geographic coding), the positions of geographical features relative to the reference is computed, the imagery is corrected for all source-dependent errors and geometric transformed into the requested map projection. At the end of this interferometric processing step, for all measured points, planimetric coordinates and height information from the InSAR geometry are achieved and transformed into a suitable reference system for topographic mapping. The detailed explanation of phase to height conversion and geocoding will be given in this section.

Phase to Height Conversion

As known, generally three reference height basis are used for the scientific applications, these are ellipsoid, geoids and topography. Topography can be summarized as the physical surface of the Earth. Ellipsoid is the mathematical description of the Earth's surface and ellipsoidal height is the vertical distance between reference ellipsoid and the point on topography along the ellipsoidal normal. The geoids is defined as level surface of the gravity field with the best fit to the mean sea level which may extend inside the solid body of the Earth (Torge 1991). And the vertical distance between geoids and interested point on topography along the plumb line is named orthometric height. Figure 3.21 shows the relations between three reference height bases.

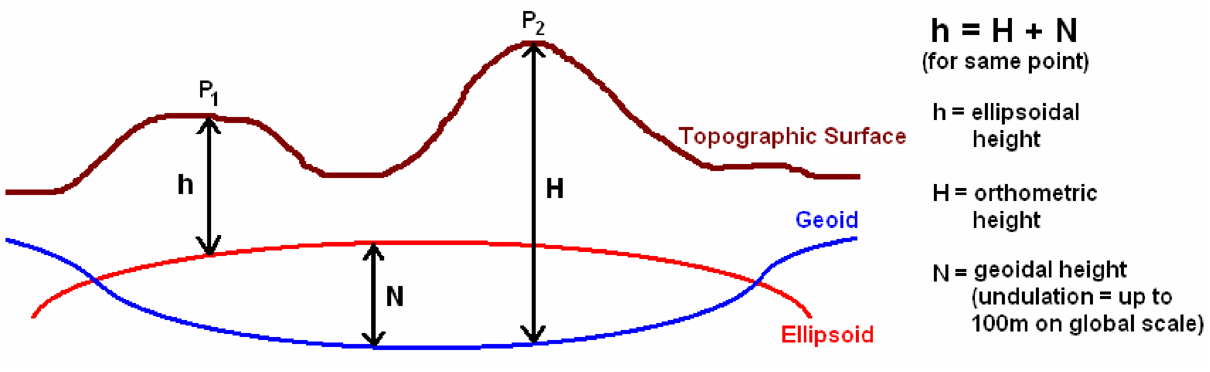

Figure 3.21 General reference height basis.

The different height systems can be related to each other by means of the geopotential number C which is defined as (Hofmann and Moritz 2006):

$$C = W_0 - W = \int_{geoid}^{po\,\mathrm{int}\,s} g\, d_n \tag{3.5}$$

W and W_0 = potentials of gravity of a point and the geoids

g = gravity

d_n = leveling increment

The height derived from SAR interferometric data sets are calculated based on a viewing geometry determined by means of orbital parameters. The satellite orbits are given in the conventional terrestrial system (CTS) that's why the heights are calculated in this system refer to a reference ellipsoid (Gens 1998). The reference to the mean sea level allows to use tide gauges placed around the coastline as height reference points corresponding to orthometric height as usually also the GCPs. The geoids ensures a horizontal representation of water surfaces such as lakes and seas. That's why the heights used in topographic maps have the geoids as reference whereas the horizontal information refers to a position on an ellipsoid (Frei et al. 1993).

Geocoding

Geocoding process of SAR images is different from optical imagery. SAR systems cause a non-linear compression that's why they cannot be corrected using polynomials. The sensor and processor characteristics have to be considered at the geometric correction. For this reason, for geocoding SAR data, Range-Doppler approach is essential. Range equation (3.6) and Doppler equation (3.7) have to be performed for each image pixel.

$$R_s = S - P \tag{3.6}$$

$$f_D = \frac{2 f_0 \left(v_p - v_s\right) R_s}{c \left|R_s\right|} \tag{3.7}$$

R_s = Slant range

S, P = Spacecraft and backscatter element position

v_p, v_s = Spacecraft and backscatter element velocity

f_0 = Carrier frequency

c = Speed of light

f_D = Processed Doppler frequency (Sarmap 2008)

The geocoding can be performed in two ways; if a reference DEM data is available and used for geocoding, this is named as terrain geocoding otherwise ellipsoidal heights are used directly and this is named as ellipsoidal geocoding. Here a SPOT-5 HRS DEM has been used as reference for the interferogram generation (according for the geocoding) from TSX data sets.

Phase to height conversion and geocoding of interferometric processing is automatically done by the ENVI-SARScape module. However, before the automatic process, coherence threshold, interpolation window size and mean window size values should be selected and requested grid size has to be determined. The result of phase to height conversion and geocoding is a DSM. Figures 3.22 and 3.23 show the DSM derived by TSX SM InSAR data set (10m grid spacing) and its 3D visualization using an exaggeration factor of 10.

Figures 3.24 and 3.25 show the DSM derived by TSX SL (3m grid spacing) and its 3D visualization using an exaggeration factor 5.

In Figures 3.22 and 3.23, the minimum and maximum height values at the grey value scales and in Figures 3.24 and 3.25, the blunders at the visualizations shall be carefully analyzed to realize the refinement effects to the TSX DSMs by following steps (shift, manipulations, blunder filtering etc.) of this study before geometric evaluation.

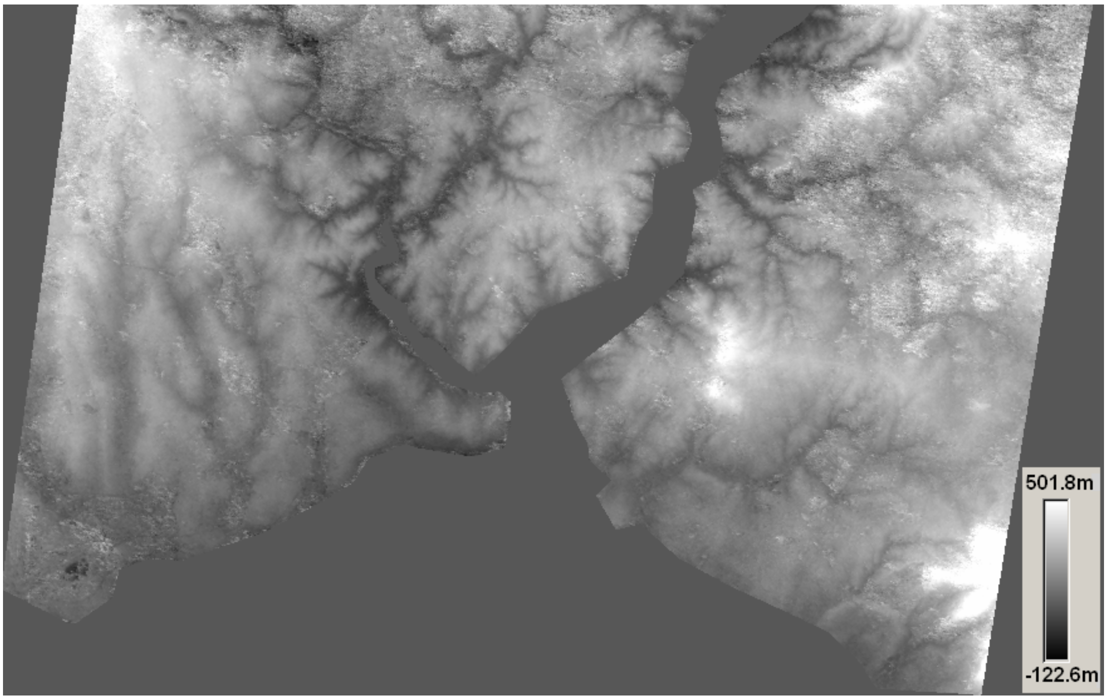

Figure 3.22 DSM of TSX SM InSAR data set (10m grid spacing).

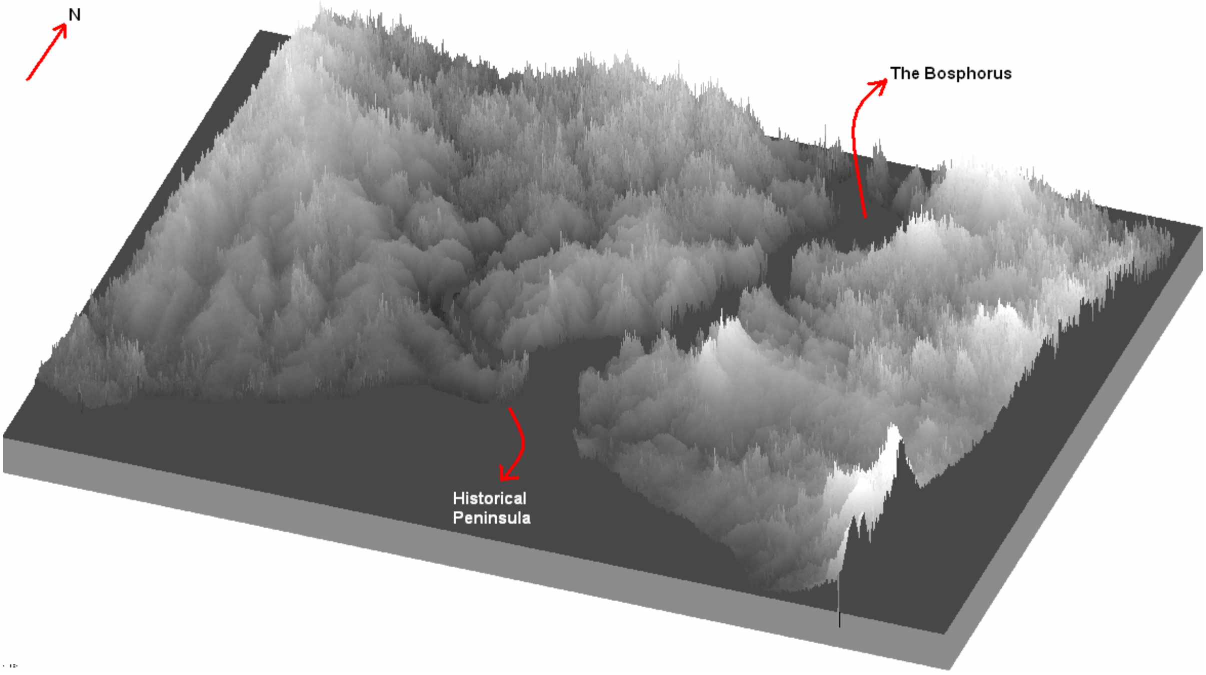

Figure 3.23 3D visualization of TSX SM DSM (exaggeration factor 10).

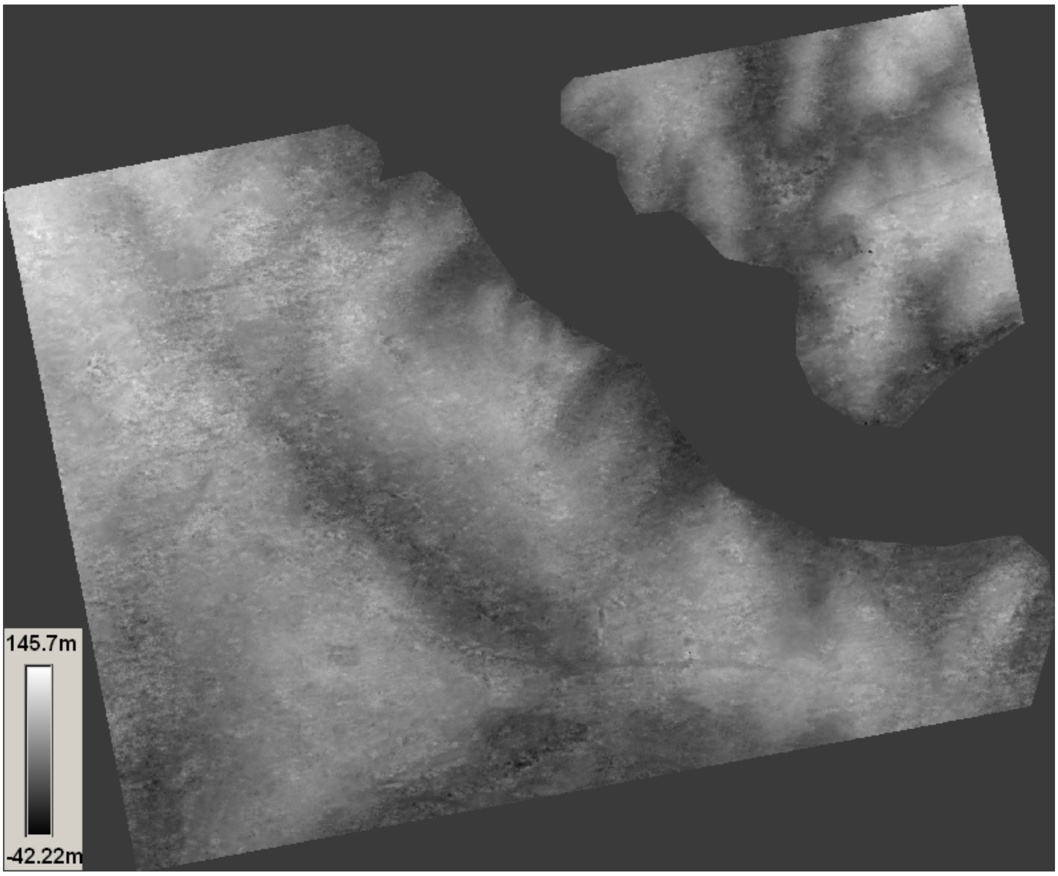

Figure 3.24 DSM of TSX SL InSAR data set (3m grid spacing).

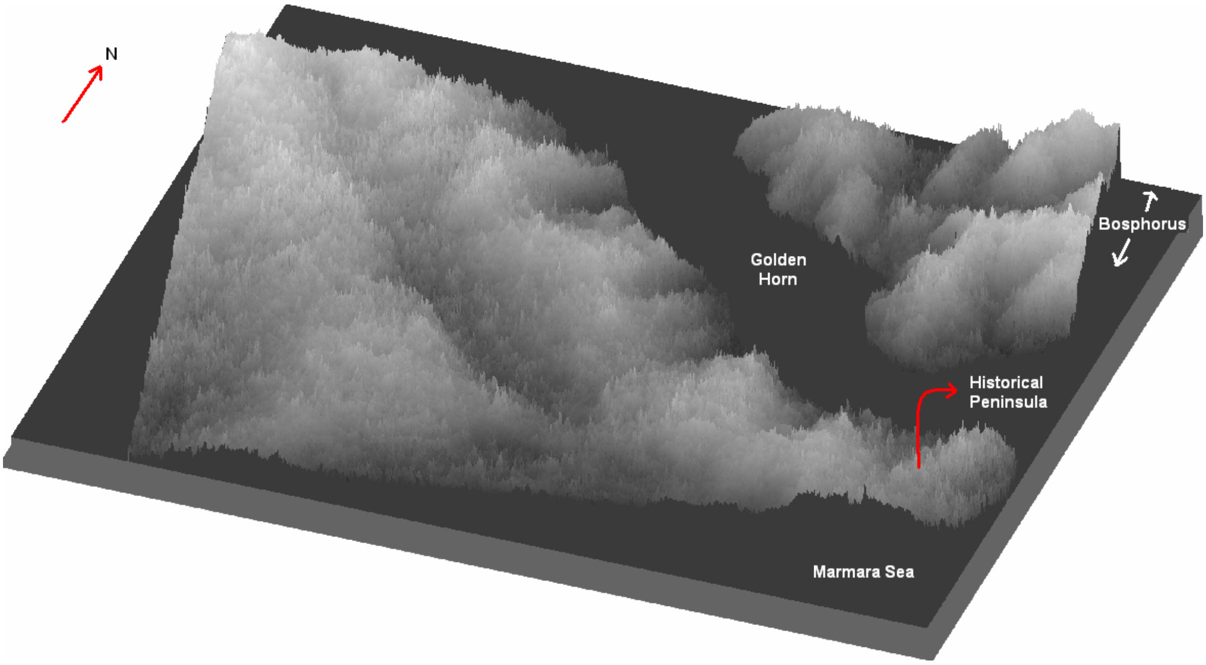

Figure 3.25 3D visualization of TSX SL DSM (exaggeration factor 5).

PART 4

DEM EVALUATION

4.1 DEM AND DEM GENERATION TECHNIQUES

A Digital Elevation Model (DEM) alias Digital Height Model (DHM) is a digital cartographic representation of the elevation of the terrain at regularly spaced intervals in X and Y directions, using Z-values related to a common vertical datum (URL 10). A DEM and its components X, Y planimetric coordinates and Z height values are shown in Figure 4.1.

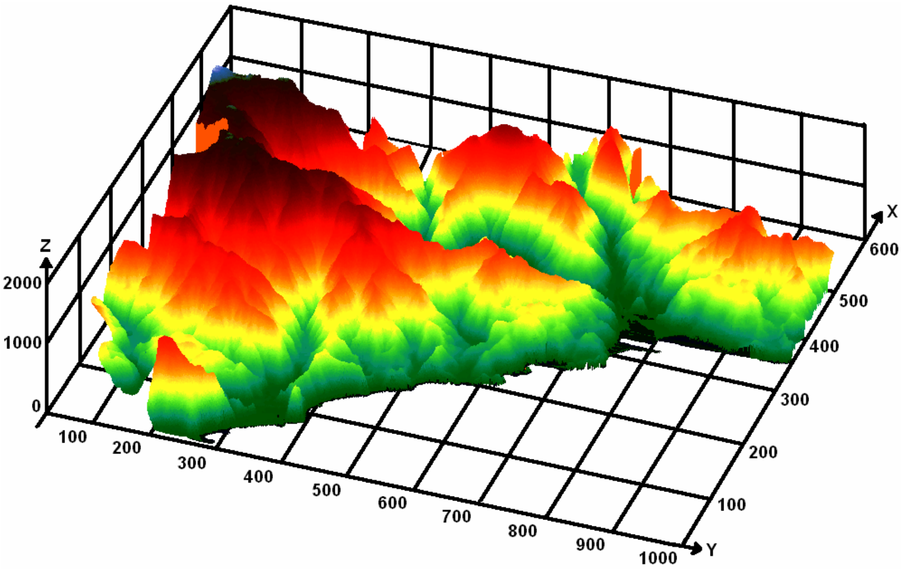

Figure 4.1 Digital elevation model (DEM) components.

As distinct from a Digital Surface Model (DSM), a DEM describes the bare surface of the earth and does not include the features on the surface such as buildings, and vegetation. Figure 4.2 presents the difference between a DSM and a DEM on the same interest area.

A DEM is a digital representation of topography and the most common. Usually, Digital Terrain Models (DTMs) contain additional topographic features on the terrain including mass points and break lines which improves the description of the bare earth topography and they are more superior for many applications against DEMs. However, owing to their high cost and time consuming generation caused by poorly matched break lines, they are not often used as DEMs.

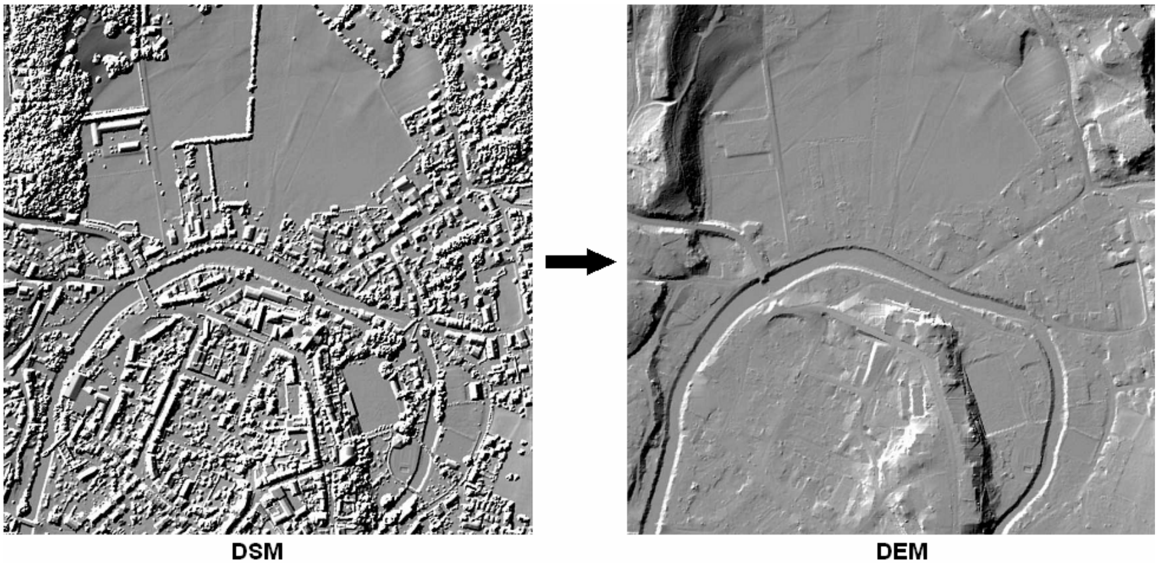

Figure 4.2 The difference between DSM and DEM.

DEMs are required for several applications like generation of orthoimages, terrain determination (such as point elevation, slope, distance, aspect), environmental analysis, generation of contour lines, modeling of hydrologic functions, cartography, civil applications, geographical information system (GIS), urban planning, disaster management (forest fires, erosion control, flood management, earthquake analysis), agriculture, visibility check and also for 3D-views. Because of this large application field, in order to satisfy the need, various DEM generation techniques have been developed up to this time. These techniques can be grouped under three headings according to data collection methods as geodesy, traditional photogrammetry based on aerial photos and remote sensing. Remote sensing contains three sub-techniques for DEM generation as stereo-optical satellite imagery, air-borne laser scanning (LIDAR) and interferometric synthetic aperture radar (InSAR). In this part of study, all of these DEM generation techniques will be described separately.

4.1.1 DEM Generation via Ground Survey

In this technique, planimetric coordinates (x, y) and height values (z) are collected point by point with surveying instruments (GPS, total stations etc.) on the topography. Nowadays, the most common instruments are Real Time Kinematic (RTK) GPSs. Using them, planimetric coordinates and height values of a point can be obtained in few seconds. The numbers of ground points are propagated using interpolation. Contour lines are generated for topographic maps. The vector data from these maps turn into digital data by contour-grid transfer or by direct interpolation of the original data.

By ground survey the collected data are precise and the produced DEMs have standard deviations up to 10cm. However, DEM generation applying ground survey are time consuming and expensive, limited to small areas. If a DEM should be generated for a large area (regional, global etc.), this method today is not economic but it can be used for the completion of a topographic map or a DEM which is generated with other advanced techniques. For example, for the completion of 1/25000 scale topographic maps of Turkey which were created using aerial photogrammetry, ground survey has been used to fill gaps. Figure 4.3 shows an example of 1/25000 scale topographic map from Zonguldak city, Turkey built-up by Turkish military agency map service and generated DEM from it.

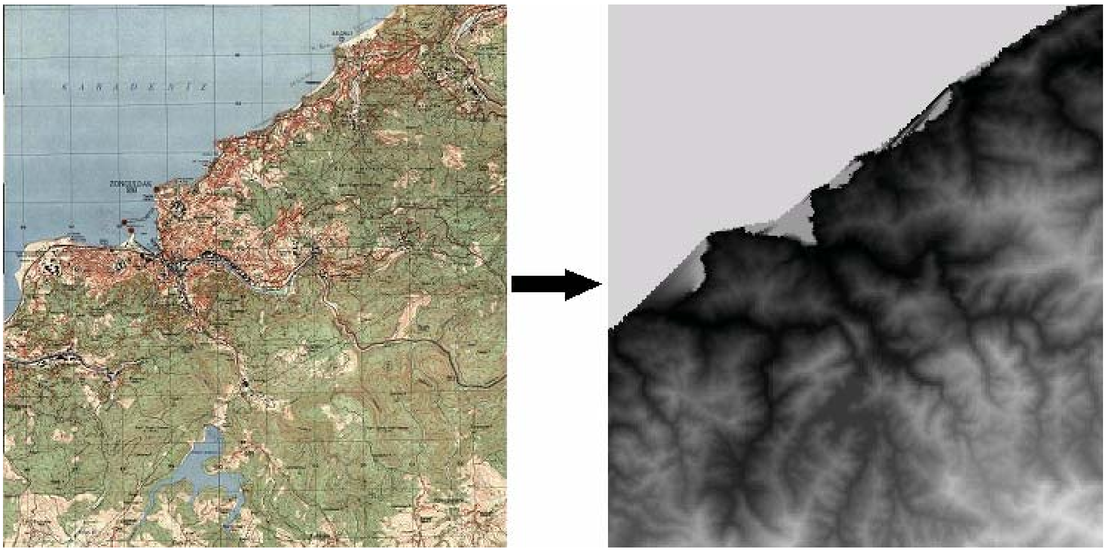

Figure 4.3 1/25000 scale topographic map and corresponding DEM.

4.1.2 DEM Generation by Aerial Photogrammetry

With a photo flight, aerial photos are taken on the interest area flight line by flight, the combination of the flight lines build blocks. Based on the standard end lap of 60%, stereo-pairs are obtained and stereoscopic evaluation can be performed using ground control points (GCPs) for the geo-reference. By means of this process the height information can be obtained beside the planimetric locations. The DEMs which are used as reference for this project are generated via photogrammetric techniques; they have 30m and 1m grid spacing. Figures 4.4 and 4.5 show these reference DEMs.

Figure 4.4 The reference DEM of Istanbul test field (30m grid spacing).

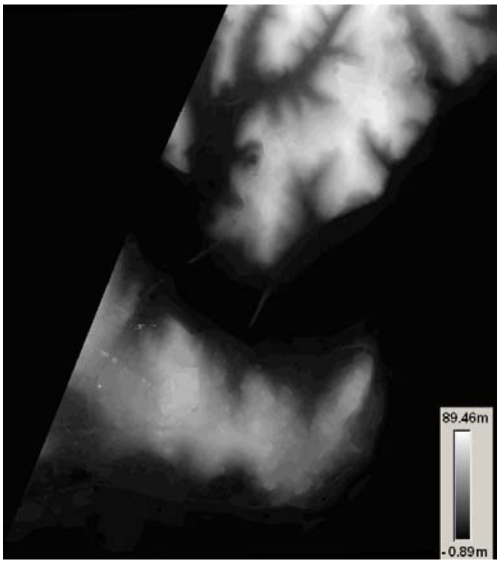

Figure 4.5 The reference DEM of Istanbul test field (1m grid spacing).

The most important disadvantage of this technique is the dependency on weather conditions. Photogrammetric flights can be made only an in cloud-free open air condition that’s why it can be done only in limited time interval. Additionally, some problems have been detected especially at automatic generated DEMs using digital photogrammetry in forest regions, grove areas, settled areas, low contrast areas and marsh areas. The supplementing ground survey is time consuming.

On the other hand, except these disadvantages, photogrammetric techniques provide precise DEMs. The accuracy of these models are between 10cm and 1m.

4.1.3 DEM Generation by Laser Scanning (LIDAR)

Air-borne LIDAR (Light Detection and Ranging or Laser Imaging Detection and Ranging) enables three dimensional data acquisition for higher resolution DEM generation. The measuring method for generating DEMs is based on active distance measurement and oriented by GPS positional determination and inertial measurement units (IMU). GPS/IMU-systems record the three dimensional position and attitude of the Laser scanner.

At laser scanning operation, by calculating the response time between transmitted and received laser pulse, the distance between Earth’s surface and laser scanner can be measured. For every measurement, in addition, an opto-mechanical device deflects the laser beam laterally into a slightly different direction. In conjunction with the forward movement of the aircraft, a wide strip of terrain is scanned as a result. In post-flight processing, the laser range, scan angle, GPS data and INS (inertial navigation system) data are combined to determine the position of each point on the earth's surface accurately (URL 11) which may be supported also ground control areas. In Figure 4.6 the basic geometry of laser scanning and laser pulse reflection steps can be seen.

The first laser pulse reflects from the top of the ground objects and describes the object surface through these objects. Using this data set which is collected by the reflection of first laser pulse, DSMs are generated. On the other hand, last laser pulse reflects may be the bare ground. It describes the bare topography of the Earth and using this data set after filtering DTMs and DEMs can be generated. Figure 4.7 shows an example of LIDAR DEM from an isle of UK.

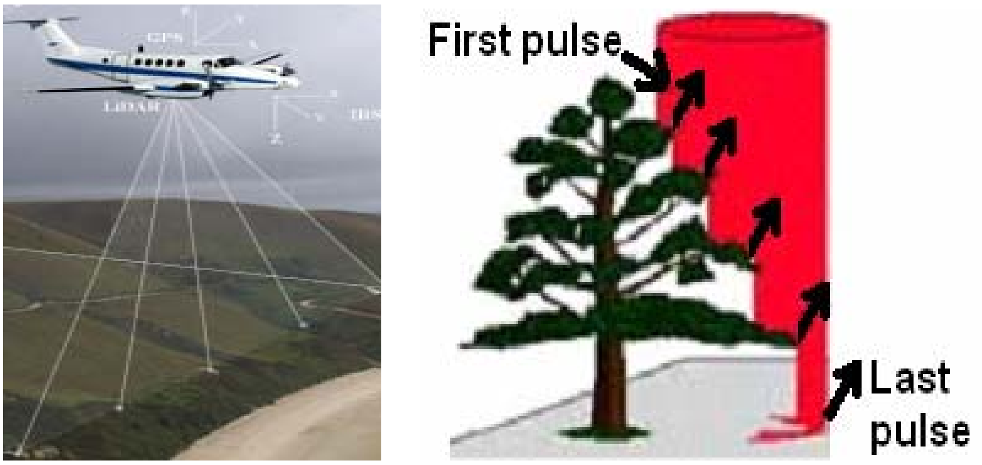

Figure 4.6 LIDAR geometry and laser pulse reflection steps.

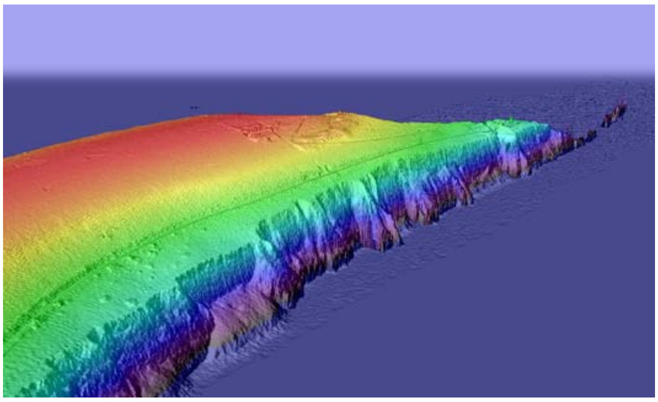

Figure 4.7 Perspective view of 'The Needles', Isle of Wight, UK as derived from LIDAR DEM (URL 12).

Nowadays, LIDAR technique progresses with high acceleration especially in business of governing city (municipality) activities. For example, operations (acquisition of stripmaps, calculation of deformation, renovation etc.) related with roads, highways, railways, bridges etc., city modeling, the conservation of historical heritage and so on. LIDAR offers high resolution data for the generation of high quality topographic maps and DEMs (10cm-2m accuracy) but it is the most expensive method of DEM generation, needs a special designed aircraft to fix the GPS, INS and IMU systems, powerful computer hardware's and software's to process collected data and for covering wide areas (≥ regional) this technique is time consuming.

4.1.4 DEM Generation via Remote Sensing From Space

As mentioned before, two main methods are used for DEM generation by remote sensing from space.

4.1.4.1 Optical Imagery

DEMs are generated regularly by this method since optical space images are economic and offer larger area coverage as ground survey, aerial photogrammetry and aerial LIDAR methods. For the DEM generation with optical images two or more images of the same area, taken from different directions are required. The image orientation has to be known in the specified object coordinate system (Jacobsen 2003). Based on this the image matching is performed. The accuracy of the generated DEMs based on optical space images is mainly depending upon the ground resolution, height-to-base relation and the image contrast. In this study, SPOT-5 HRS, ASTER and IKONOS optical DEMs are used for the analysis. Figure 4.8 shows the SPOT-5 and ASTER DEMs of Istanbul. SPOT-5 HRS DEM has 20m, ASTER DEM has 30m grid spacing.

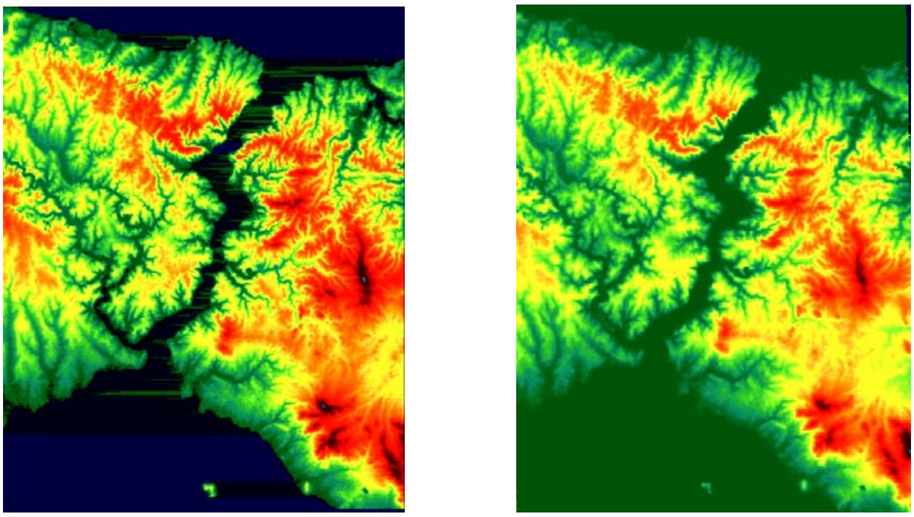

SPOT-5 HRS DEM (20m grid spacing) ASTER DEM (30m grid spacing)

Figure 4.8 SPOT-5 HRS and ASTER DEMs of Istanbul.

The DEMs can be generated fast but there are still some problems. The main problems are the conditions of weather and light. The optical imagery is directly depending upon weather conditions like aerial photogrammetry. Images should not contain clouds and in addition the sun elevation during imaging should be sufficient. Besides these problems, the very high resolution optical space sensors are mainly operating not in a stereo mode with the exception of stereo sensors as ASTER, SPOT-5 HRS and Cartosat-1. Therefore acquisition of high resolution suitable stereo-pair may take long time for an interest area. Because of this situation and difficulties to get high resolution stereo-pairs taken from the same orbit, optical images taken in a time interval are preferred to achieve stereo-pairs thus some parts of the images might include clouds and also changes are occurred caused by vegetation and different sun elevation.

4.1.4.2 Interferometric Synthetic Aperture Radar (INSAR)

The DEM data acquisition using SAR interferometry was explained in the study parting section 2.2.4. Sample DEMs generated by single-pass interferometry can be seen in Figure 4.9. These DEMs are the outcomes of SRTM C-band and X-band data in Zonguldak city, Turkey. The C-band DEM has 3 arcsecond (~90m) and X-band DEM has 1 arc-second (~30m) grid spacing. The triangle at the X-band DEM represents no data part.

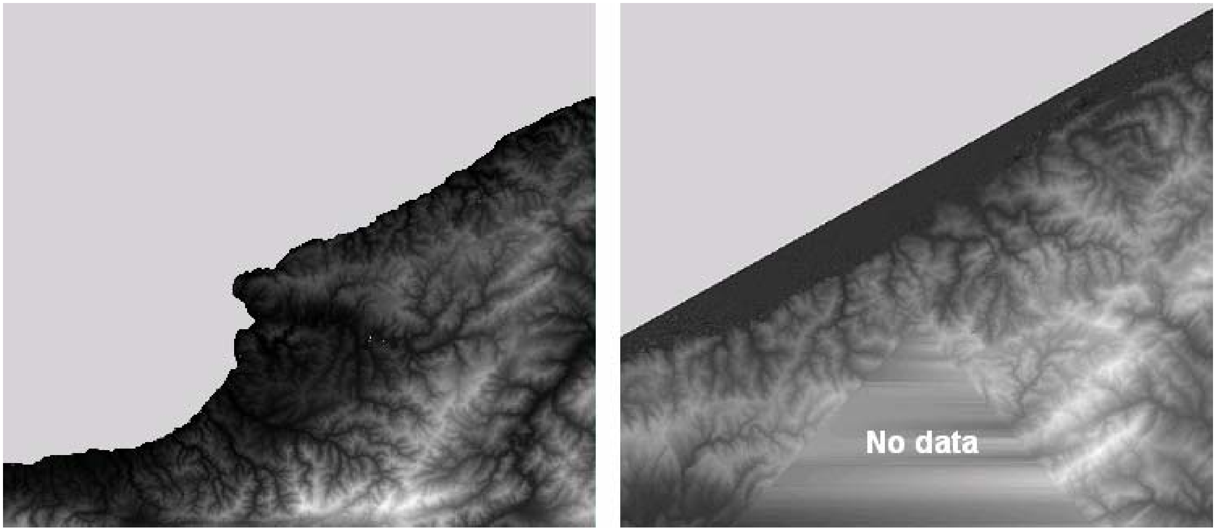

Figure 4.9 SRTM C-band and X-band DEMs.

DEM generation using interferometric synthetic aperture radar technique has several advantages. In this method, data collection is independent from weather conditions except heavy rainfall, clouds can be penetrated and large coverage up to global can be obtained fast at specific times. Besides, it permits imaging at very low look angles thus results in remarkable different perspectives than common vertical photographs. Additionally, it enables resolution to be independent of distance to the target objects also polarization effects can be used. But also DSM generation by InSAR has some disadvantages in comparison with other techniques, object recognition is poor in SAR images that's why the selection of GCPs are more difficult and because of imaging geometry and related distortions mentioned in section 2.2.2, accuracies of DEMs are lower especially in steep and mountainous parts of the interest area.

4.2 DEM EVALUATION – OVERVIEW

After the generation of a DEM, the next step should be the evaluation because the accuracy and characteristics of the generated DEM have to be known to specify its possible applications. For example, land survey requires high quality DEMs whereas forestry does not need.

For analysis a reference DEM is required. The generated DEM is compared against this and for each height value the discrepancy is determined. Point by point, by calculating the elevation differences between generated DEM and reference DEM the Root Mean Square of the height (Z-component) (RMSZ) values are obtained and the absolute and relative accuracy of generated DEM can be determined. The morphological details presented by the DEM are also analyzed. Various factors influence the accuracy of a DEM, mainly; the topographic characteristics (flat, hilly, steep, mountainous, forested etc.) of interest area, the DEM data collection method accordingly sampling distance. The quality of the reference DEM also has to be respected.

Table 4.1 shows the main acquisition techniques and the accuracy level of their DEM products.

Table 4.2 represents the required height accuracies for cartographic mapping defined by U.S national map accuracy standards.

In this study, DEMs acquired by space-borne SAR interferometry - TSX SL, TSX SM and SRTM C-band - and space-borne optical imagery - IKONOS, SPOT-5 HRS and ASTER –

have been evaluated. For the evaluation processes two height models derived by aerial photogrammetry have been selected as reference.

Table 4.1 DEM acquisition techniques and the accuracies.

Acquisition technique	Coverage	Accuracy of DEM
Ground	Local, large scale mapping	10cm – 50cm
Aerial photogrammetry	Regional	10cm-1m
Laser scanning	Regional	10cm-2m
Space-borne SAR interferometry	Regional to global	0.5m-20m
Airborne SAR interferometry	Regional	10cm-5m
Space-borne optical imagery	Regional to global	0.5m-20m
Digitizing from map	Depends on mapping coverage	Depends on maps

Table 4.2 U.S national map accuracy standards.

Map Scale	Horizontal accuracy RMS (m)	Vertical accuracy RMS (m)	Cartographic image map resolution (m)	Thematic image map resolution (m)
1:250000	75	15-30	14	≤75
1:100000	30	6-15	6	≤30
1:50000	15	6	3	≤15
1:25000	7.5	3	1.5	≤7.5

4.3 DEM EVALUATION

In the study, the common coordinate system was defined as UTM (universal transverse Mercator) for the whole of data sets and references. That’s why before the evaluation processes, the transformation of the coordinate systems of all of data sets into UTM suitable zone have been performed using program BLTRA. This program is a member of system BLUH (Bundle Block Adjustment Leibniz University Hannover), developed by Dr. Karsten Jacobsen, Institute of Photogrammetry and Geoinformation (IPI), Leibniz University of

Hannover, Germany. Table 4.3 illustrates an example about the transformation of geographical coordinates into UTM suitable zone in program BLTRA.

Table 4.3 Coordinate transformation by program BLTRA.

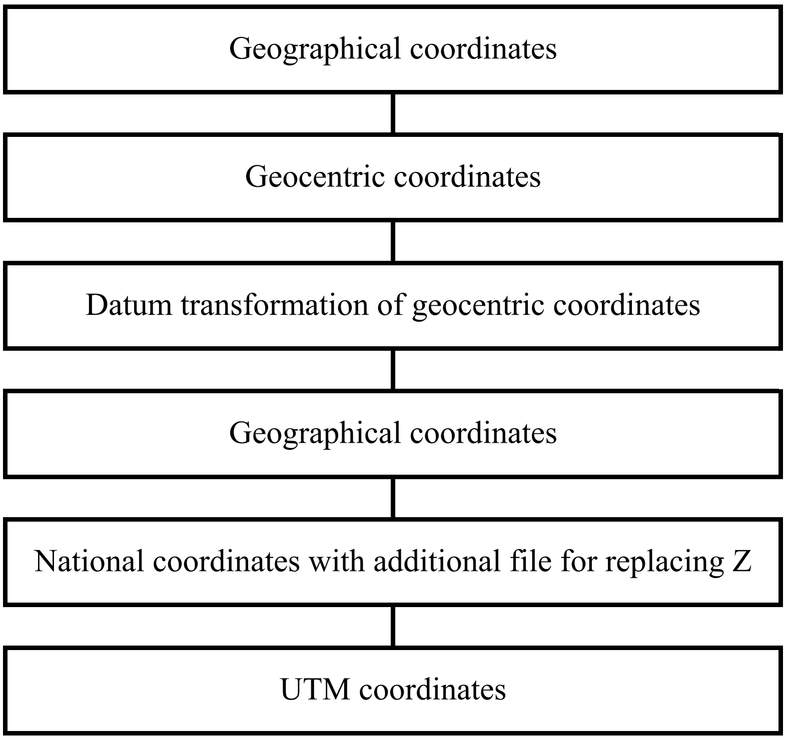

4.3.1 Main Programs for DEM Evaluation

After the transformation of all models into UTM suitable zone, for the evaluation analysis, a number of investigations have been performed using several modules of the software package BLUH. Table 4.4 shows these evaluation programs and their functions.

4.3.1.1 RASCOR

Using program RASCOR, an elevation model which is generated by any technique in equal grid spacing or a random arrangement can be analyzed, improved, filtered and interpolated.

Program RASCOR can identified points which are not located on the solid ground but on topographic features like vegetation and buildings by a minimal and maximal height in the area, by maximal height differences between neighbored points, by a sudden change of the height level, by a linear or polynomial interpolation in X- and Y-direction, by a minimal and maximal height difference against a local tilted plane or polynomial surface and a local prediction (least squares interpolation) based on the tilted plane or polynomial surface. The final results can be filtered (smoothened) in relation to a rotated plane or polynomial surface fitted to the neighbored, blunders can be eliminated and a graphical representation as isometric plot by means of HP/GL-files is possible. Figure 4.10 shows the impact of filtering process by program RASCOR (Jacobsen 2004).

Table 4.4 DEM evaluation programs and their functions.

Program	Function
RASCOR	Filtering, analysis, correction and plot of a DEM
DEMSHIFT	Shifting of a DEM to another in X, Y, Z and scaling in Z
DEMANAL	Accuracy Analysis of DEM against a reference DEM
MANI	Manipulation of object coordinates, image orientations, IMU-data and pixel addresses, numbering the points
BLCON	Conversion of ground coordinates window function, reduction to equal distributed points, change of spacing
DEMINT	Computation of Z-value for points with given X and Y by interpolation of a raster-digital elevation model
ZANAL	Analysis of a DEM
ZPROF	Plot profiles
UNDUL	Calculation of Geoid Undulation
HPSHOW	Visualization

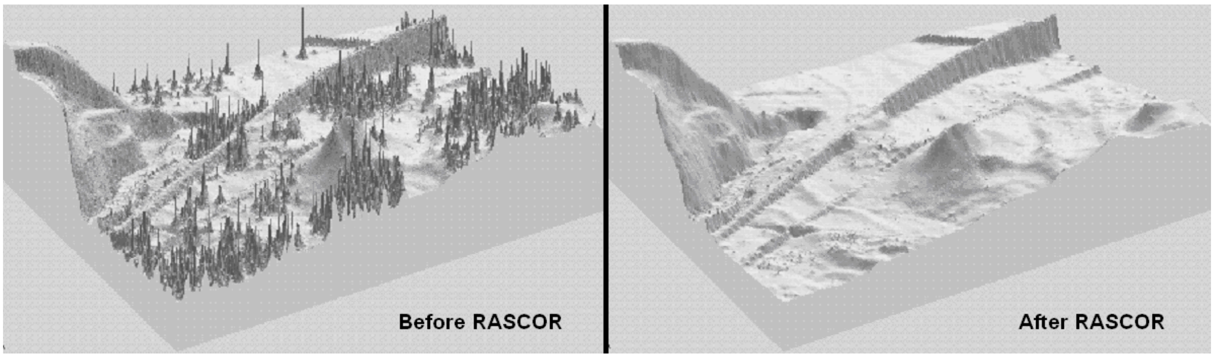

Figure 4.10 Impact of program RASCOR.

In program RASCOR, the number of iterations for the filtering process can be determined by the operator from 1 up to 9 considering some cases like the topographic structure of the test field (flat, rough, mountainous etc.), urban or rural area coverage (built-up areas, forests, vegetation etc.), the quality and homogeneity of data set etc..

After filtering and elimination of blunders, DSMs substantially converge into DEMs. Figure 4.11 shows the differences between the elevation model of largely built-up area of Istanbul (test field 1) derived by TSX SM data set before and after program RASCOR.

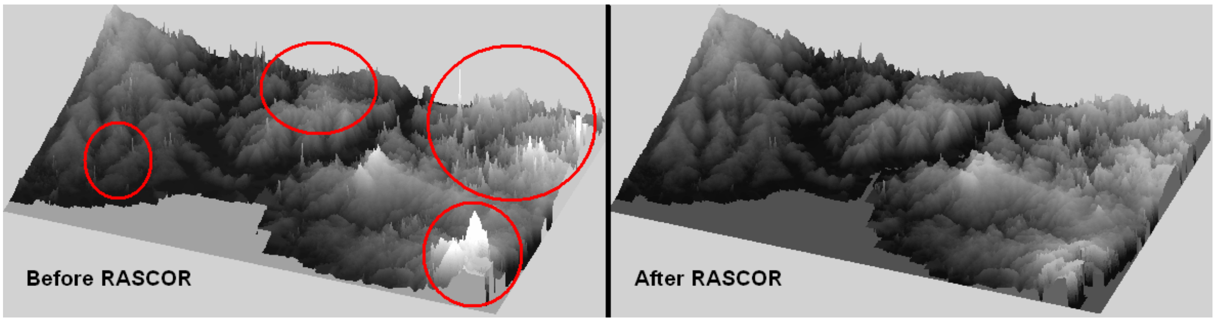

Figure 4.11 Changes of the height model by program RASCOR.

4.3.1.2 DEMSHIFT

One of the principle rules for the DEM accuracy analysis is overlapping of the evaluated DEM and reference DEM. Since the reference DEMs are generally in national coordinate systems they may be influenced by local datum effects. On the other hand, also the evaluated DEM may have horizontal shifts. Figure 4.12 presents the horizontal shift (ΔD) of same point between two DEMs and height difference (ΔZ) because of this horizontal shift.

Figure 4.12 Effect of horizontal shift between DEMs.

In Figure 4.12, it can be seen that point ‘P’ has different planimetric coordinates (X and Y) in two DEMs and locates in different positions because of horizontal shift. This shift causes height differences for the same points and errors for the height accuracy analysis between two models. After all, it is not correct to make an evaluation between two height models not fitting to each other.

In this study, the program DEMSHIFT is used to shift a DEM to another in X, Y and Z. In addition the scale of the Z-component can be adjusted in this program. To use this program, reference DEM and the DEM which shall be shifted and scaled have to be in ASCII form. In addition, reference DEM has to be in regular grid spacing. The evaluated DEM may have a random point distribution and the grid spacing may not be same as for the reference. The reference points corresponding to the file for analysis are determined by bilinear interpolation.

The shift and the possible scaling are determined by adjustment. Only the first 10 million points of the file for shifting are respected in the adjustment, but all points are used for the output file. Depending upon the terrain inclination, a different number of iterations is required. Independent upon the specified number of iterations in the input, the iteration stops if there is no more improvement at the RMSZ value. In this study, '11' iterations were required for DEM shifting. If the scale of the Z-component also shall be determined, the last iteration will be made without scaling. The convergence radius of the DEM shifting may be limited depending upon the terrain inclination – in this case a rough DEM shift should be performed before by program MANI or BLCON (Jacobsen 2006).

4.3.1.3 MANI

If large RMSZ values are achieved with DEMSHIFT, this indicates large shifts of the height model with a size outside the convergence radius. In this case a pre-correction of the height model with program MANI is possible. The object coordinates can be manipulated manually by this program. The points and coordinates for manipulation can be achieved by a visual inspection of the height models like shown in Figure 4.13.

For example, a point located in a river junction is measured in the evaluated and the reference DEMs and the difference in location (X, Y coordinates) is used as pre-correction. The coordinate differences (ΔX, ΔY) are added or subtracted to the DEM which shall be shifted to the other. In addition, point numbers can be inserted automatically to the data sets after typing the lowest number which the operator wants to start by the help of program MANI.

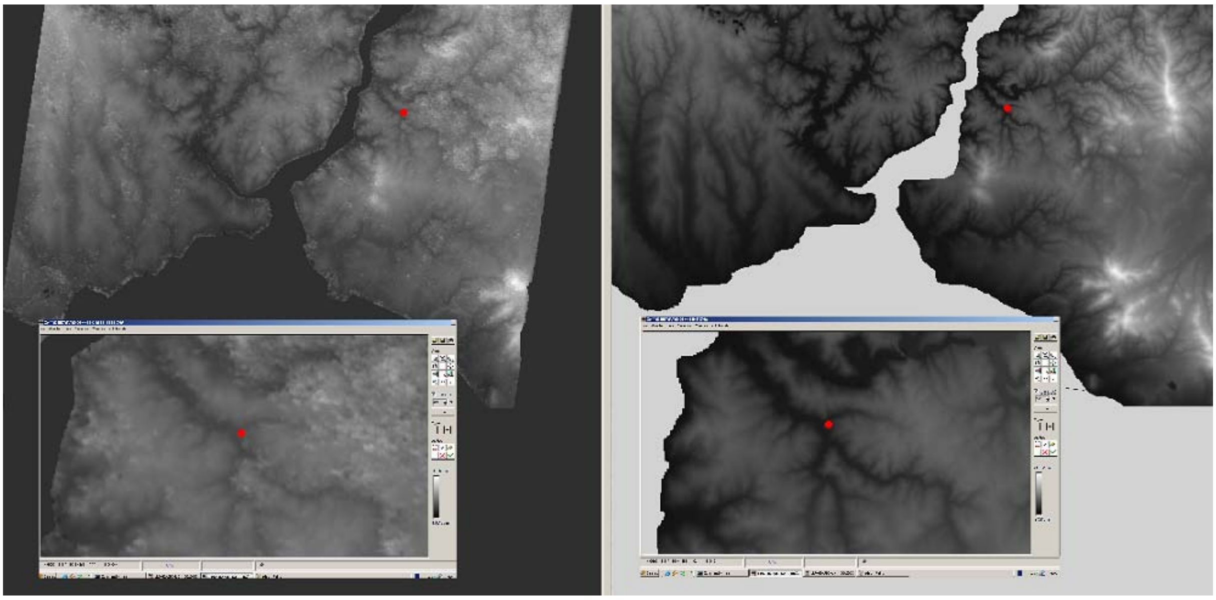

Figure 4.13 Selection of points for pre-correction with program MANI.

4.3.1.4 DEMANAL

After the elimination of the shifts between two height models, the accuracy and accuracy characteristics of a DEM against a reference DEM can be analyzed by program DEMANAL. In this program, accuracy analysis can be done for different layers (land classes) separately (open flat areas, forest areas etc.) because they can have also dissimilar characteristics and the accuracy of them may be different. For example, in this study, especially water surfaces, intensive forest areas and steep and mountainous parts of the height models also have dissimilar characteristics and cause noise and problems for InSAR, meanwhile nearly flat areas and built-up areas have high coherence and accuracy.

In DEMANAL, the discrepancies between the evaluated DEMs and reference DEMs can be analyzed in detail including the analysis for a dependency against the terrain inclination and the height level. The influence of a vertical scale difference can be respected iteratively (Jacobsen 2006). Same with DEMSHIFT, the reference data set has to be in regular grid spacing, the evaluated DEM may have a random point distribution and the grid spacing may not be same with the reference. The reference points corresponding to the file for analysis are also determined by bilinear interpolation.

At the end of program DEMANAL, the distribution of the point heights, the frequency distribution of slope on the terrain, the frequency distribution of DZ (Z-difference between both files) etc. can be visualized by HPSHOW and the graphical representations can be plotted. Figure 4.14 shows a graphical representation example of the frequency distribution of DZ.

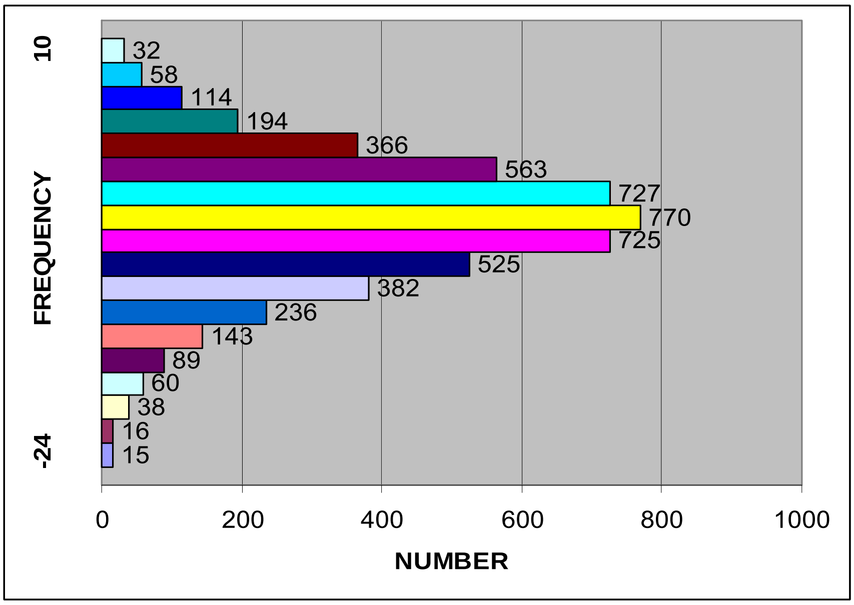

Figure 4.14 Graphical representation example of the height differences distribution of DZ.

The high numbers of graphics achieved by DEMANAL during the accuracy analysis are shown in a different section.

4.3.1.5 BLCON

Program BLCON can convert ground coordinates of the three accepted control point definitions of program system BLUH or projection center coordinates of image orientations into each other format and can convert Helava-GPF-files into the structure required by BLUH. ASCII-files in raster arrangement (equal spacing of points) can be reduced to another spacing. In addition the ground coordinates can be shifted, the sign can be changed and the output file can be limited to the points located in or outside of windows. The number of points in the input file can be reduced depending upon the location. It will be reduced to 1 point in a sub-area which can be specified. The output file can be reduced by points from a second input file which does have a similar location. The use of the input file can be limited by the definition of a first and last line. The window function can be used also for photo orientations (Jacobsen 2004).

In this study, window function of this program has been used especially for dividing the DEMs into the coordinates of REFDEM 2 for the overlapping and evaluation in historical peninsula (test field 2). An example of this division by BLCON can be seen in Figure 4.15. For the accuracy level control of REFDEM 2, a part of REFDEM 1 was divided into the limitations of REFDEM 2 and after overlapping accuracy analysis was performed.

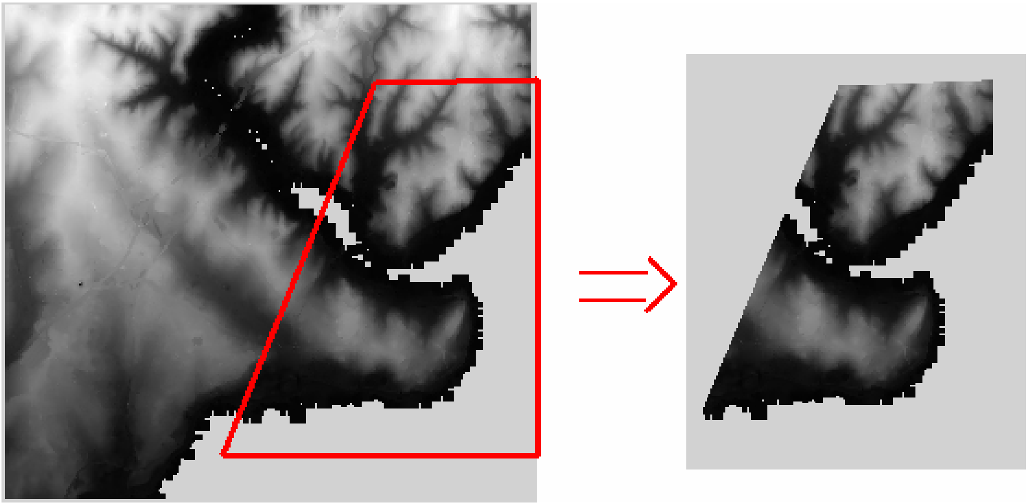

Figure 4.15 Window function of program BLCON.

4.3.1.6 Other Programs

In the study, besides these main evaluation programs, for different types of analysis, various programs have been used too. For example, the loss of accuracy by interpolation can be analyzed with program ZANAL. It allows the interpolation over a multiplication of the spacing and a comparison of the interpolated value against the corresponding original height value. An estimation of the loss of accuracy by interpolation is possible based on the hypothesis that the loss of accuracy is depending upon the square of the spacing.

In ZANAL the DEM which shall be analyzed can be divided into windows. The number of windows can be selected as 2*2, 4*4, 6*6 etc. Figure 4.16 represents the analysis of influence of interpolation by ZANAL as example of interpolation over the double spacing.

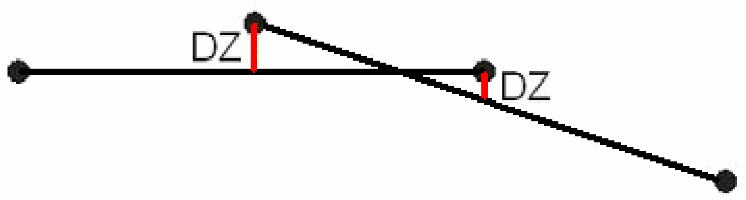

Figure 4.16 Analysis of influence of interpolation by ZANAL as example of interpolation over the double spacing.

Besides ZANAL, program DEMINT has been used for the interpolation of Z-values for points with given X and Y-coordinates in a raster-DEM. A bilinear interpolation based on the neighbored 4 points or a polynomial surface based on the neighbored points can be used in this program.

Program ZPROF has been used for plotting the profiles and aspects which can be visualized by program HPSHOW.

Program UNDUL has been used for the calculation of geoid undulations.

4.3.2 Programs for DEM Visualization

4.3.2.1 LISA

In the study, for the visualization, interpolation (by triangulation, moving surfaces etc.) and regular gridding of DSMs and DEMs, program LISA has been used. This program has been generated at the Institute of Photogrammetry and Geoinformation, Leibniz University of Hannover, Germany by Dr. Wilfred Linder. In program LISA, a height model and its height levels can be seen in a color scale accompanied minimum up to maximum heights at the same screen and different color palettes can be created and used for visualization. Using the optimum palette in every process, the details can be established clearly. Figure 4.17 shows a DEM in four different color palettes. First image represents the original grey value coded visualization and others are different palettes.

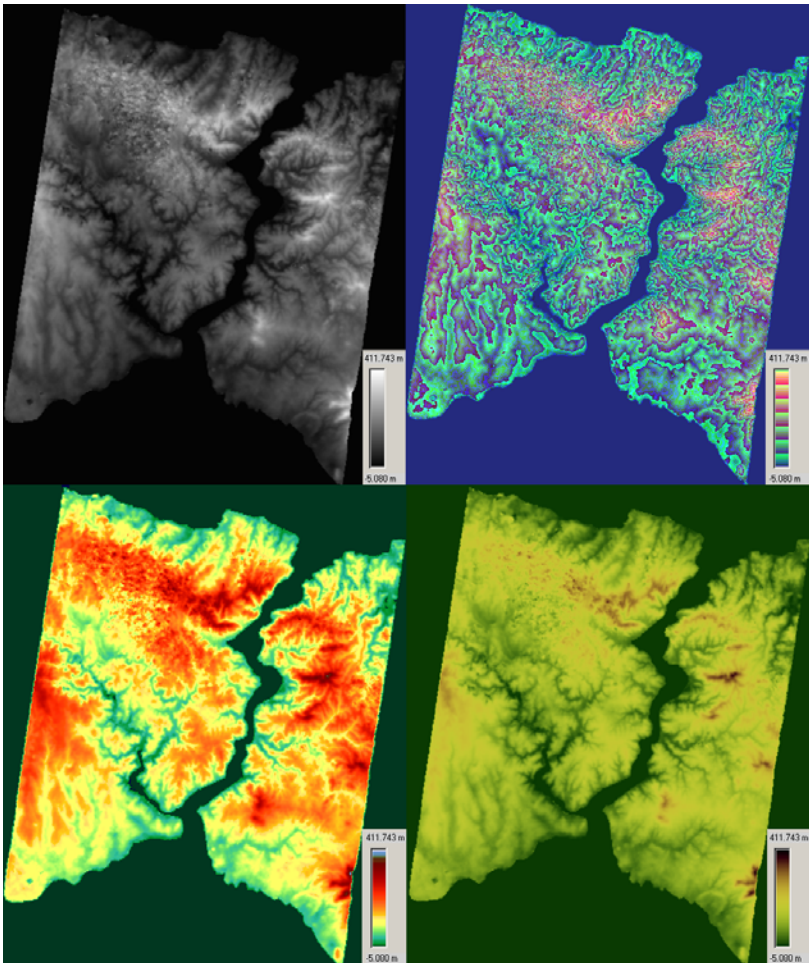

Figure 4.17 DEM presented with different palettes by program LISA.

In addition, program LISA enables to create 3D visualizations of height models, implementation of morphologic detail analysis, generation of contour lines and generation of differential DEMs. These types of analysis which have been made by LISA and corresponding results as it can be seen parting section 5.

4.3.2.1 Photoshop CS3

The program Photoshop was applied to see the outcome raw files of program DEMANAL (the regions of height discrepancies between DEMs etc.) and for the creation of different layers for separate accuracy analysis (open, forest, sea etc.).

PART 5

DATA, RESULTS AND DISCUSSIONS

In this section, initially the general description and topographic characteristics of the test areas and the evaluated DEM data is given, followed by the evaluation analysis of height models. At the evaluation analysis, a number of investigations have been performed using several modules of the software package BLUH, explained in section 4. Firstly, determination of systematic bias (i.e. shift) between evaluated DEMs and reference DEMs have been handled. After respecting shifts between the height models, absolute and relative accuracy analysis have been performed for determination of the DEM accuracy levels, frequency distribution of terrain inclination graphic representations and aspect dependency of analyzed data sets have been created, influence of interpolation analysis have been made for calculating the loss of accuracy by the interpolation using two different methods, morphological detail analysis have been applied by visualization of contour lines based on DEMs, differential DEMs have been created and shading analysis have been performed for the quality assessment of DEM visualizations.

5.1 TEST FIELD AND DATA SETS

5.1.1 General Description and Characteristics of the Test Areas

The test area Istanbul is located in north-west area of Turkey. The Greater Municipality Area has a coast line to the Black Sea and the Marmara Sea connected by the Bosporus. Istanbul is one of the biggest cities in the world. About 14 million people leave in the city and most of settlements are at the surrounding of Bosporus and coast line of Marmara Sea. Figure 5.1 shows the location of the city and the close up satellite image derived from Google Earth.

Istanbul is a suitable test area for the accuracy analysis because its topography contains various characteristics and this enables to understand the quality of evaluated DEMs in different types of terrain formations. In patches, terrain is open-flat, hilly-steep and woody. But generally, city scope is rolling with elevations up to 540m. Approximately 50% of the city is covered by built-up (urban) areas, the rest is forestry. Figure 5.2 shows an example of the topography.

Figure 5.1 Location of Istanbul and space image of the test area.

Figure 5.2 Example of Istanbul topography.

In the study, the analysis has been performed for two test areas in Istanbul. One of these areas is a large test field of approximately 30km×20km, covered approximately by 80% with built-up and by 20% with forest area. The elevation goes from sea level up to 435m. This test field is named as test field 1 in the study. Figure 5.3 shows the Google Earth image of test field 1 with the frequency distribution of terrain inclination.

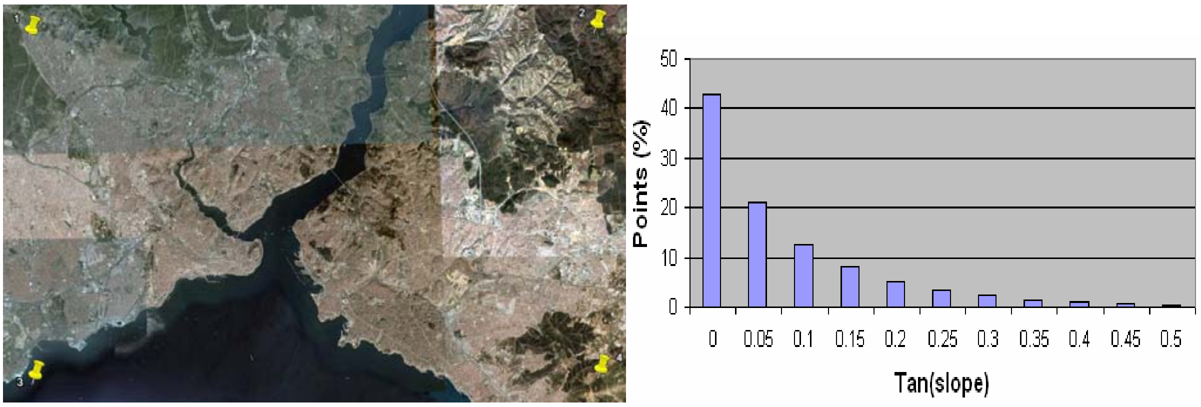

Figure 5.3 Test field 1 with frequency distribution of terrain inclination.

The second test area is selected especially for the analysis of TSX SL DSM and covers 10km×8km. It includes the historical peninsula and near surroundings. Historical Peninsula (Old City) is one of the most important regions in Istanbul, located on the European side, neighbored to the Bosporus and Marmara Sea. This part named as Historical Peninsula because of its historic heritage. This test field is named as test field 2 in the study. Figure 5.4 shows the high resolution IKONOS satellite image of test field 2 with the frequency distribution of terrain inclination. This area has smoother topography in relation to the rest of Istanbul. The elevation reaches from sea level up to 130m.

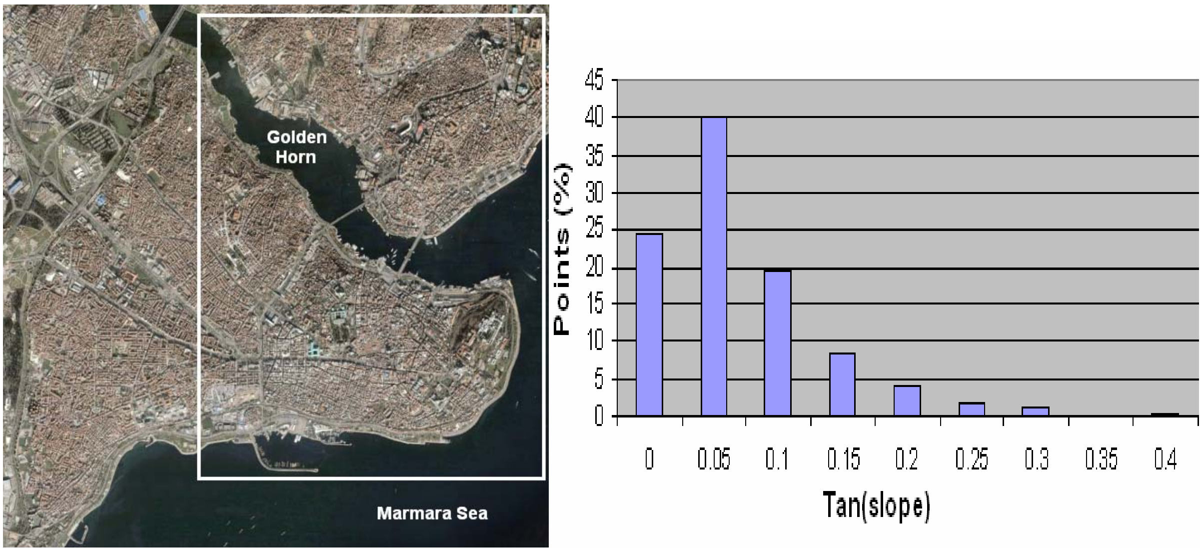

Figure 5.4 Test field 2 with frequency distribution of terrain inclination.

5.1.2 Reference DEMs

Two different DEMs have been used as reference for the accuracy analysis in this study. Both of them were obtained by photogrammetry and has 10cm up to 1m accuracy.

5.1.2.1 Photogrammetric DEM 1:5000 Scale

First reference DEM was obtained from 1:5000 scale photogrammetric maps acquired by a project of Greater Istanbul Municipality and contains the whole Istanbul city area. Because of this large coverage, it has been produced with 30m grid size for avoiding too big file sizes for the data processing. Figure 5.5 shows this large coverage reference DEM.

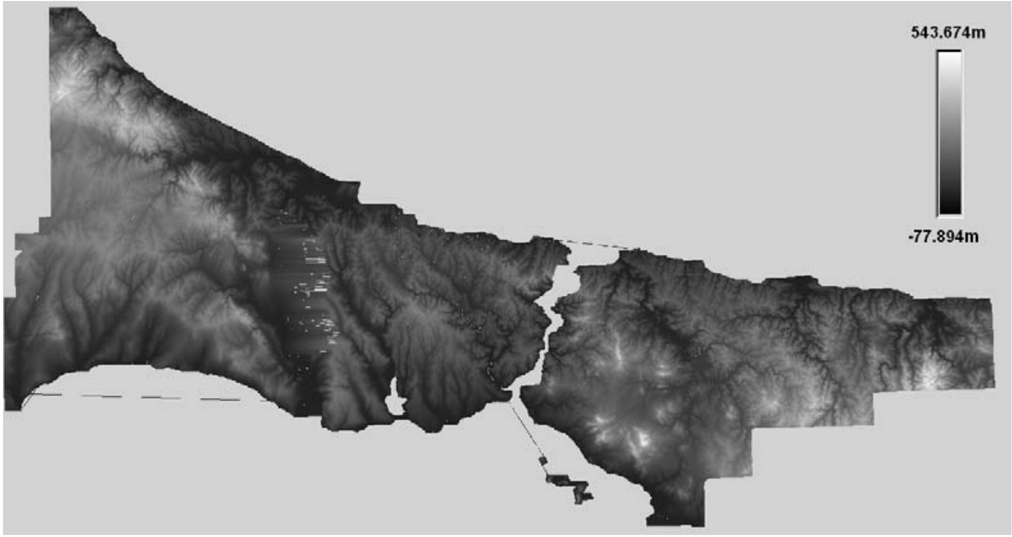

Figure 5.5 Reference DEM of whole Greater Istanbul Municipality area (1:5000).

For the overlapping with the evaluated DEMs and avoiding to study with large data set, this reference DEM has been reduced into required limits using program BLCON. The reduced version can be seen in Figure 5.6 along with color coded height representation.

This reduced DEM overlaps with test field 1, approximately 30km×20km and covers approximately 80% built-up and 20% forest areas. The elevations are in between sea level and 435m. This reference DEM is named as 'REFDEM 1' in the study.

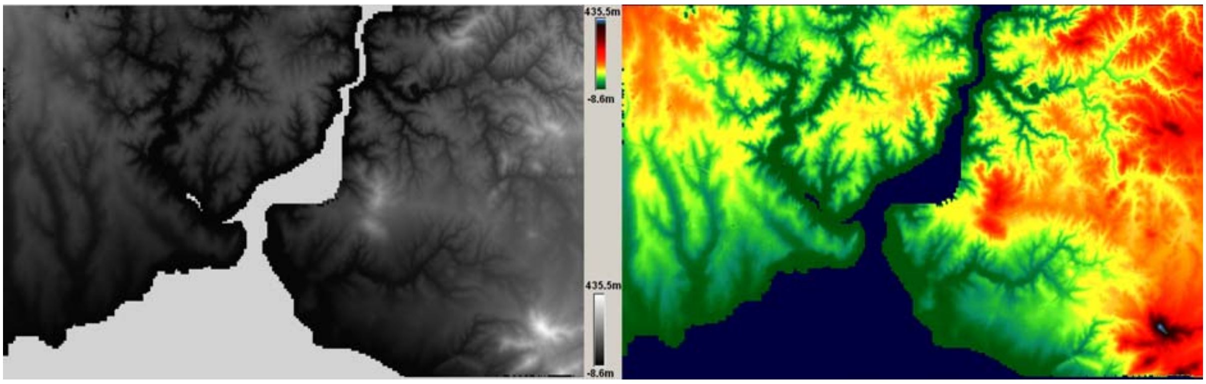

Figure 5.6 First reference DEM as grey value and color coded version (1:5000).

5.1.2.2 Photogrammetric DEM 1:1000 Scale

Second reference DEM was derived from 1:1000 scale digital aerial photogrammetric maps, a project of Greater Istanbul Municipality and involves the large part of Historical Peninsula and near surroundings. This DEM was generated between 2007 and 2009. The original grid spacing of the DEM is 5m but it has been resampled into 1m according to the needs of the project. Figure 5.7 illustrates this reference DEM along with colored version to visualize the elevation levels easier.

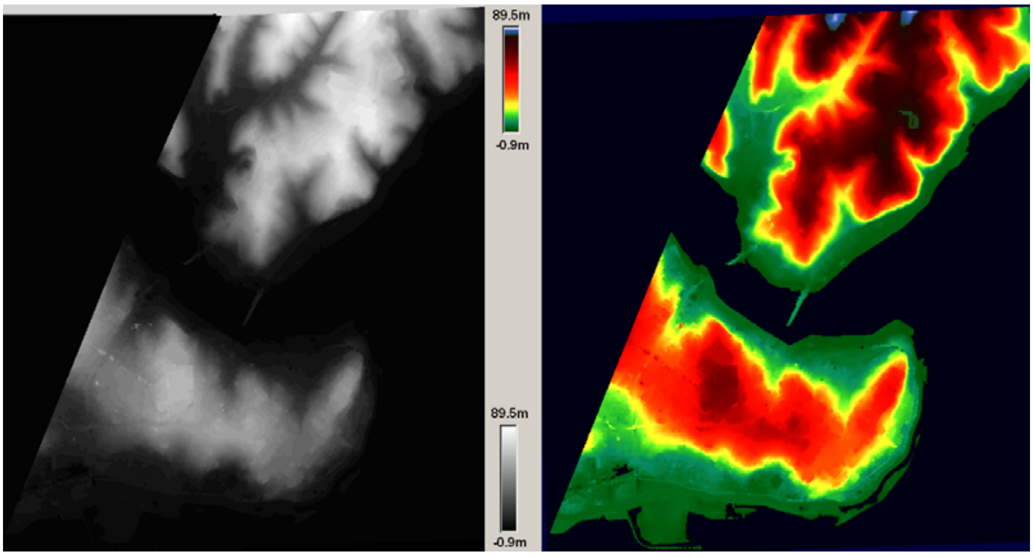

Figure 5.7 Second reference DEM as grey value and color coded version (1:1000).

This DEM overlaps with test field 2, approximately 5km×5km and covers more than 95% built-up areas that's why accuracy analysis were not performed for open and forest areas separately in this test field. The elevations are in between sea level and 90m. This reference DEM is named as 'REFDEM 2' in the study.

5.1.3 DEMs Derived by Optical Imagery

In this study, IKONOS, SPOT-5 HRS and ASTER DEMs derived by optical stereo image pairs have been used for the analysis. They are explained in detail in this section.

5.1.3.1 High Resolution IKONOS DSM

The world's first commercial very high resolution optical satellite IKONOS (means image in Greek) was launched to space in 1999 by Geoeye, USA. It has panchromatic and multispectral sensors and is able to take images with a ground resolution of 0.82m (PAN) and 4m (MS) with 11.3km swath width from 681km orbital altitude. By the combination of both sensor products 1m pan-sharpened color images can be created. The more than 300 million square kilometers of imagery that IKONOS has been collected over every continent; they are used for national security, military mapping, air and marine transportation, by regional and local governments and others (URL 13).

In this study, in Istanbul test field, PAN IKONOS GEO stereo model with a ground sampling distance (GSD) of 1m was available. The height-to-base (h/b) ratio value was 1.6 (angle of convergence 35°) and the sun elevation angle is 65.5° (Alobeid et. Al. 2009). Using this stereo model DSM have been generated in 3m grid spacing overlapping with test field 2 and with the refinement processes (shifting, blunder filtering etc.) regulated for the evaluation analysis. Figure 5.8 shows the generated IKONOS DSM along with its color coded version before the refinement process.

Figure 5.9 illustrates the DSM of IKONOS overlapping with test field 2 (corresponding with REFDEM 2) after refinement processes.

This DSM overlaps completely with TSX SL DSM and is the most important indicator for understand the quality of TSX SL DSM.

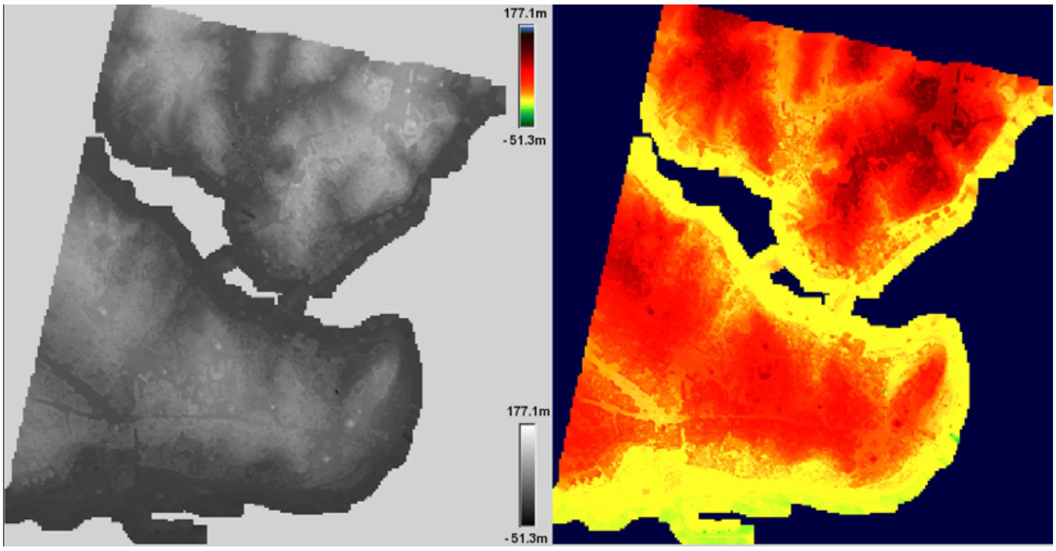

Figure 5.8 IKONOS DSM before refinement grey value and color coded.

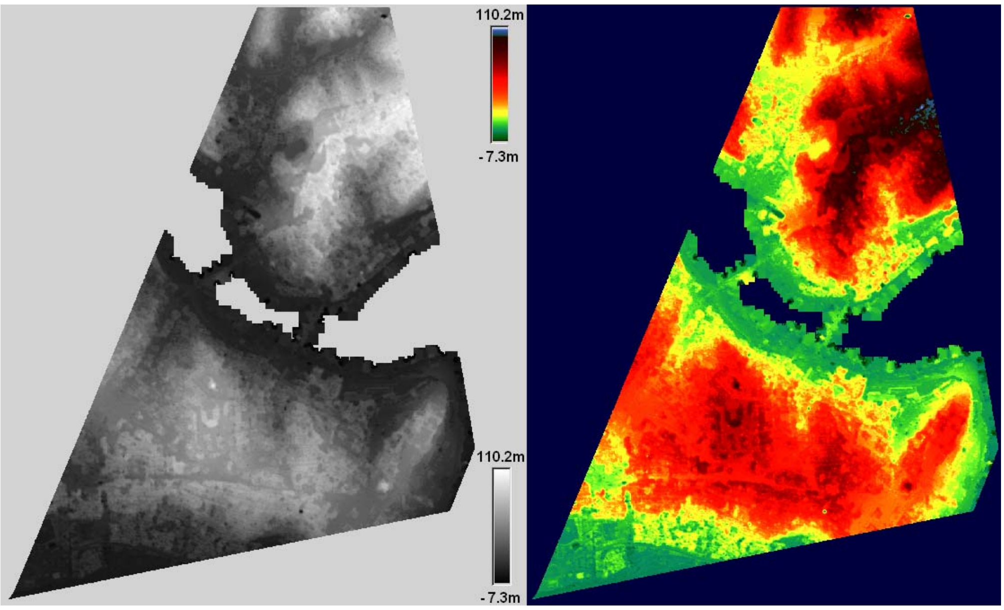

Figure 5.9 IKONOS DSM (test field 2) grey value and color coded.

5.1.3.2 SPOT-5 HRS DSM

First SPOT (Satellite Positioning and Tracking) mission SPOT-1 was generated by a joint project of France, Belgium and Sweden in 1986. Following missions SPOT-2, SPOT-3 and SPOT-4 were respectively launched in 1990, 1993 and 1998. Finally, the last mission of

SPOT family SPOT-5 was launched to its orbit in May 2002 along with Ariane 4 launch vehicle from Europe's spaceport in Kourou, French Guiana.

SPOT-5 ensures data continuity with the previous satellites but provides also enhanced images (at 5 m resolution with its two HRG instruments) and new stereoscopic capabilities with the HRS instrument. A star tracker is used to get attitude measurements and therefore good image location. The High Resolution Stereoscopic instrument (HRS) has two telescopes and acquires stereopairs at a 90-second interval, of 120-km swath, along the track of the satellite, with a h/b ratio of about 0.8. (Minimum base-to-height ratio is 0.5) (Baudoin et al, 2003). Forward and backward acquisitions cannot be performed at the same time. As a consequence, the maximum scene length that can be acquired in the range of 600 km (≈ 832 km altitude x 2 x tan(20°)). Forward and backward images are obtained in the same panchromatic spectral band as for HRG. The size of the pixels on the ground is 10m x 10m. However, the HRS instrument has been designed for a ground sampling distance of 5 meters along the track. In a direction close to the epipolar planes, this along-track over-sampling allows higher altimetric accuracy of the DEM to be obtained (Michalis and Dowman 2004).

The SPOT-5 HRS DSM of Istanbul test field used in this study was available in 20m grid spacing and covers so large area but it has been reduced to the study area. Figures 5.10 and 5.11 show the SPOT-5 HRS DEMs along with their color coded representation in test field 1 and test field 2.

The elevations of the SPOT-5 HRS DSM ranges between -3 and 435m in test filed 1. However in test field 2 maximum height values are exceeding REFDEM 2 and reach up to 105m.

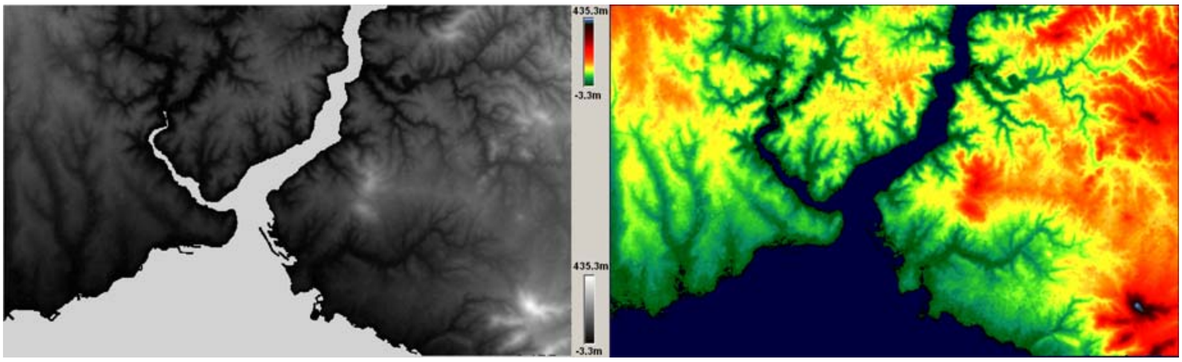

Figure 5.10 SPOT-5 HRS DSM (test field 1), grey value and color coded presentation.

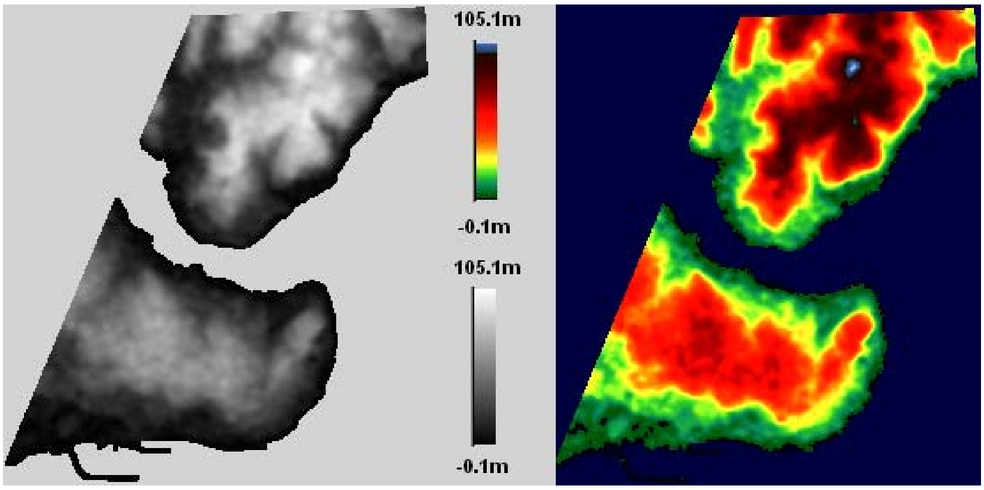

Figure 5.11 SPOT-5 HRS DSM (test field 2), grey value and color coded presentation.

5.1.3.3 ASTER DSM

The optical satellite ASTER (Advanced Spaceborne Thermal Emission and Reflection Radiometer) has been launched to its orbit in December, 1999 by NASA. The satellite was capable to along-track stereoscopy. It used two telescopes in its near infrared spectral band to acquire data from nadir and backward views and collected over 1.2 million scenes in a global coverage (North 83° to South 83°) between March 2000 and August 2008 (temporal coverage between January 2000 and June 2008).

Using entire ASTER stereo-optical images, a Global DEM was generated and early 2009, it was allowed to the scientific usage. This DEM has 1 arcsecond (~30m) posting interval, approximately 20m vertical (LE90) and 30m horizontal (CE90) accuracy with 90% confidence.

For this study, this global DSM has been obtained from Land Processes Distributed Active Archive Center (LPDAAC) as four parts, mosaic into one. Final ASTER DSMs used at the analysis can be seen in Figures 5.12 and 5.13 along with their colored representation.

The elevations are in between -3m and 423m in the area of test field 1 and between 0.1m and 93m in test field 2.

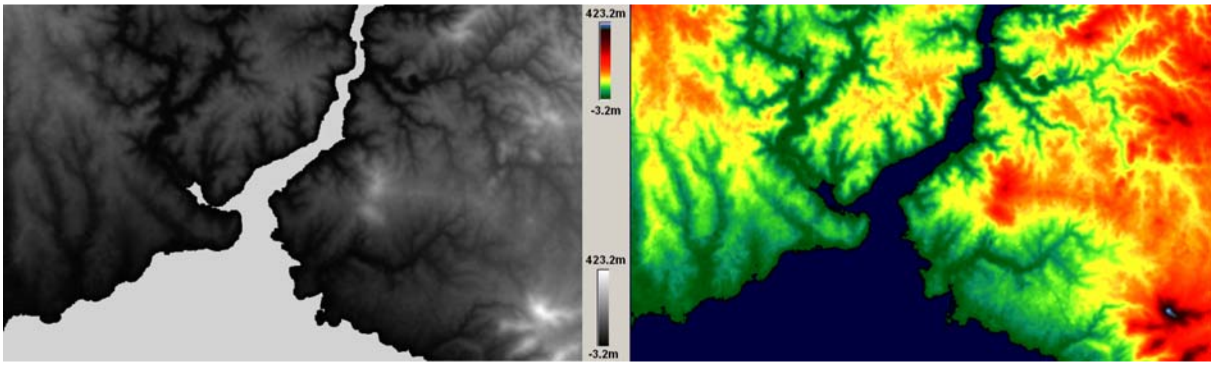

Figure 5.12 ASTER DSM (test field 1), grey value and color coded presentation.

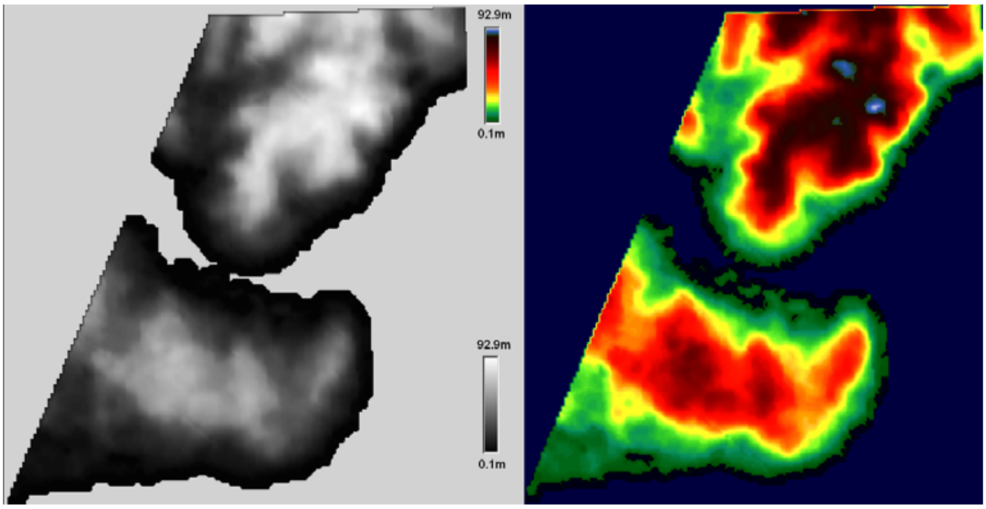

Figure 5.13 ASTER DSM (test field 2), grey value and color coded presentation.

5.1.4 DEMs Derived by SAR Interferometry

In this project, SRTM C-band DSM, TSX SM DSM and TSX SL DSM derived by SAR interferometry have been used for the analysis. They are explained in sequence in this section.

5.1.4.1 SRTM C-Band DSM

The characteristics of SRTM (Shuttle Radar Topography Mission) are explained at section 2.3.2. The DSM is generated based on SRTM C-band data and has in the average 70m grid size (3 arcsecond). Figures 5.14 and 5.15 indicate the SRTM C-band DSMs of test areas along with their colored representation.

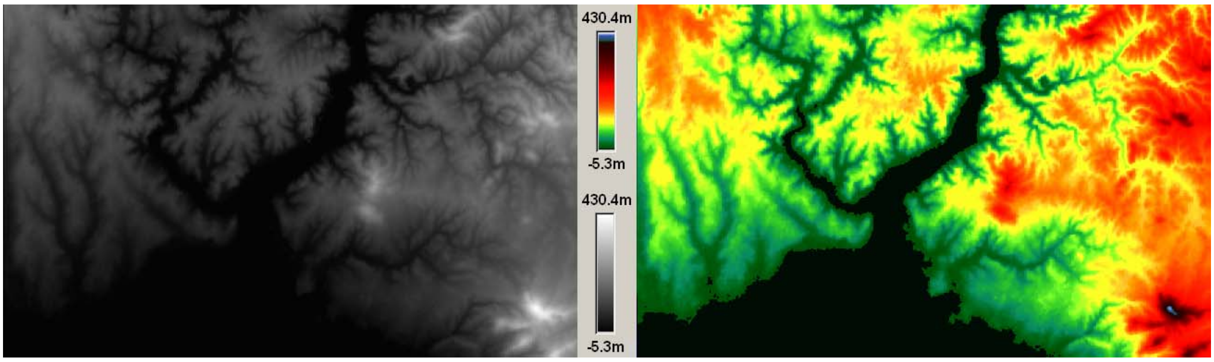

Figure 5.14 SRTM C-band DSM (test field 1), grey value and color coded presentation.

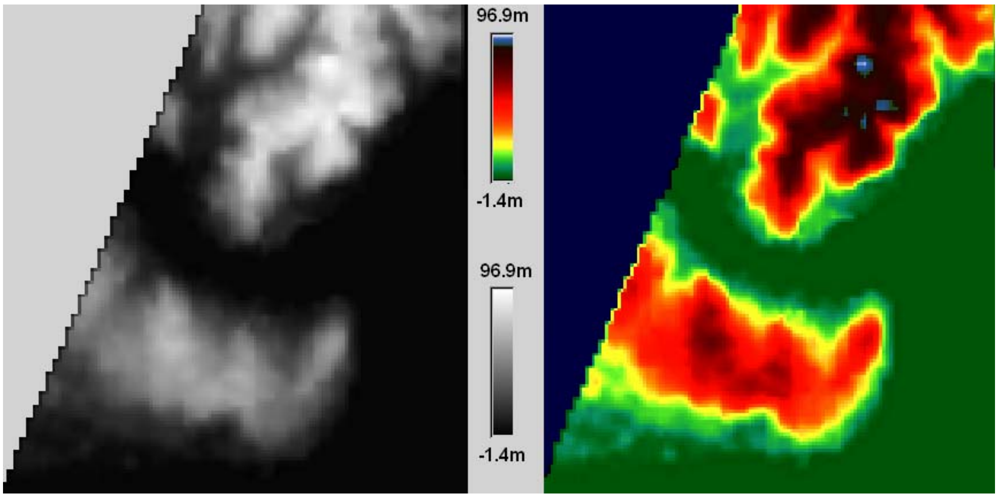

Figure 5.15 SRTM C-band DSM (test field 2), grey value and color coded presentation.

The elevations are in between -5m and 430m in the area of test field 1 and between -1m and 97m in the with the area of test field 2.

5.1.4.2 TerraSAR-X Stripmap DSM

As mentioned before, this model is derived by TSX Stripmap mode InSAR image- pairs explained in InSAR data sets section (3.1). It has been generated with 10m grid spacing using interferometric processing steps of the Sarscape module of program ENVI 4.6. Figure 5.16 and 5.17 show this DSM and colored representation of it in test field 1 and test field 2.

The elevations are in between -8m and 443m in the area of test field 1 and between -7m and 116m in the area of test field 2.

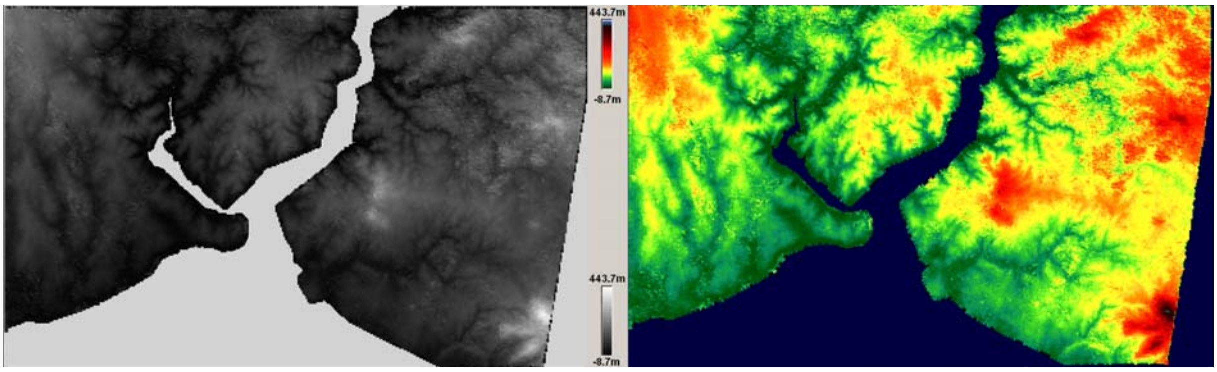

Figure 5.16 TSX SM DSM (test field 1), grey value and color coded presentation.

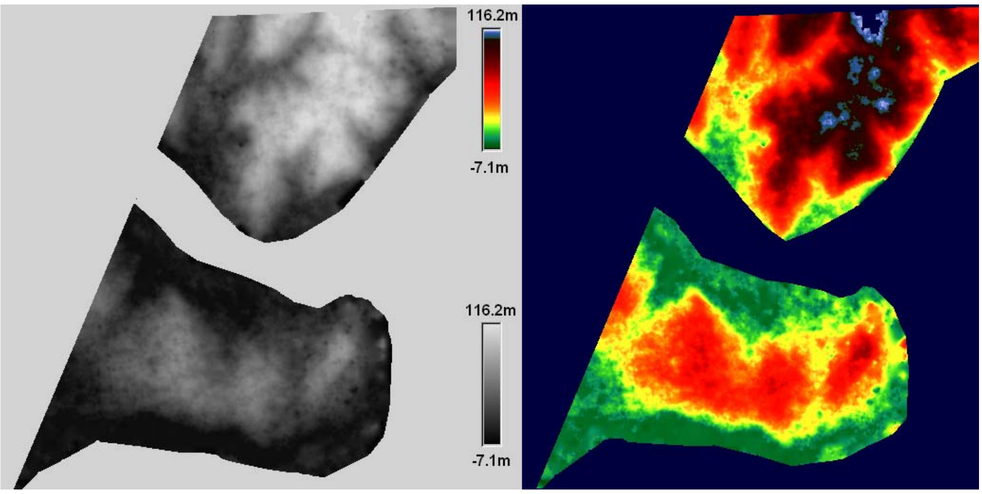

Figure 5.17 TSX SM DSM (test field 2), grey value and color coded presentation.

5.1.4.3 TerraSAR-X High Resolution Spotlight DSM

This model is derived by high resolution TSX Spotlight mode SAR image-pairs explained in InSAR data sets section (3.1). It has been generated with 3m grid spacing using interferometric processing steps of the Sarscape module of program ENVI 4.6. Figure 5.18 displays this DSM along with its colored representation and Figure 5.19 illustrates the area of test field 2.

The main difference of this model against the others is the coverage. The high resolution spotlight InSAR images of TSX used in this study have just 10km×10km ground coverage. That’s why only the DSM of historical peninsula and the near surroundings of it were generated using TSX SL SAR image-pair. The elevations range between -9m and 127m in test field 1 and between -7m and 109m in test field 2.

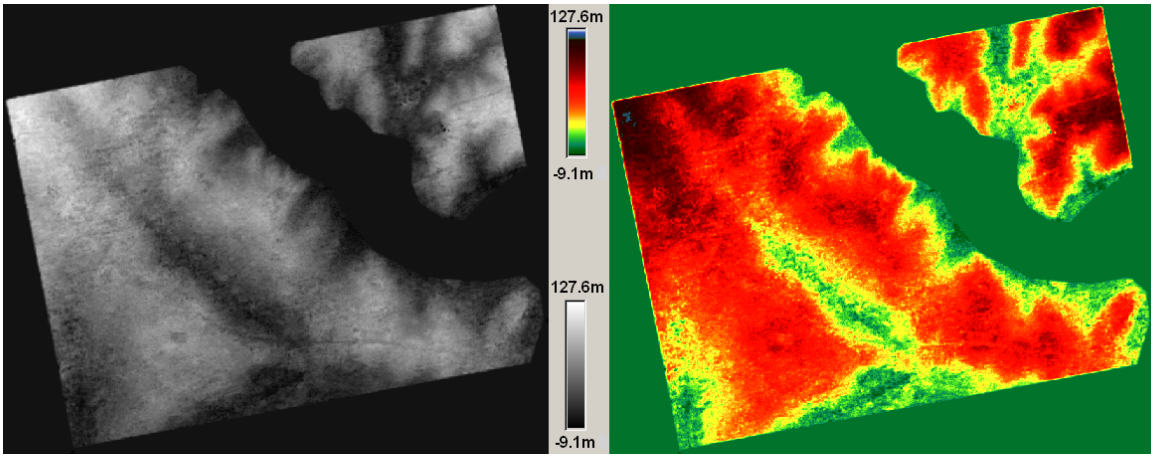

Figure 5.18 TSX SL DSM, grey value and color coded presentation.

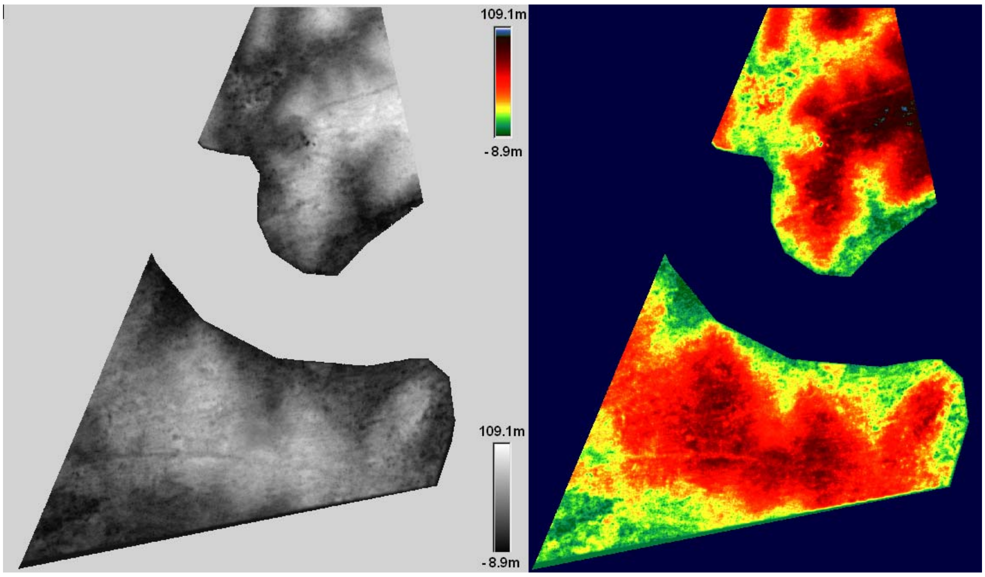

Figure 5.19 TSX SL DSM (test field 2), grey value and color coded presentation.

5.2 SHIFT OF DSMs AND PREPARATIONS

As mentioned in section 4.3.1.2 in order to perform the correct accuracy analysis, the DSM which will be evaluated must have the same location as the reference DEM. For this case, the determination of shifts to the reference height model has to be determined. Initially, using program DEMSHIFT shifts against the reference DEMs are determined. In this operation, maximum accepted ΔZ is selected as 50m and based on the handling the number of iterations are preferred as 11.

As the result of this first determination, the large shift values which cause large incorrect RMSZ values up to 20m have been seen and the radius of convergence for the shift adjustment was exceeded. Accordingly, for the elimination of large shifts the DEMs were pre-corrected by manual shift via point matching using program MANI explained in section 4.3.1.3. The points of corresponding location and their planimetric coordinates (X and Y) were selected from all evaluated DSMs and reference DEMs. The coordinate differences were calculated and used for the rough shifts. Figures 5.20 and 5.21 show the selected points at the corresponding locations for the pre-correction of the evaluated DSMs and reference DEMs in test field 1 and test field 2. TSX SL and IKONOS height models are only available in test field 2. That’s why point selection was performed just for test field 2.

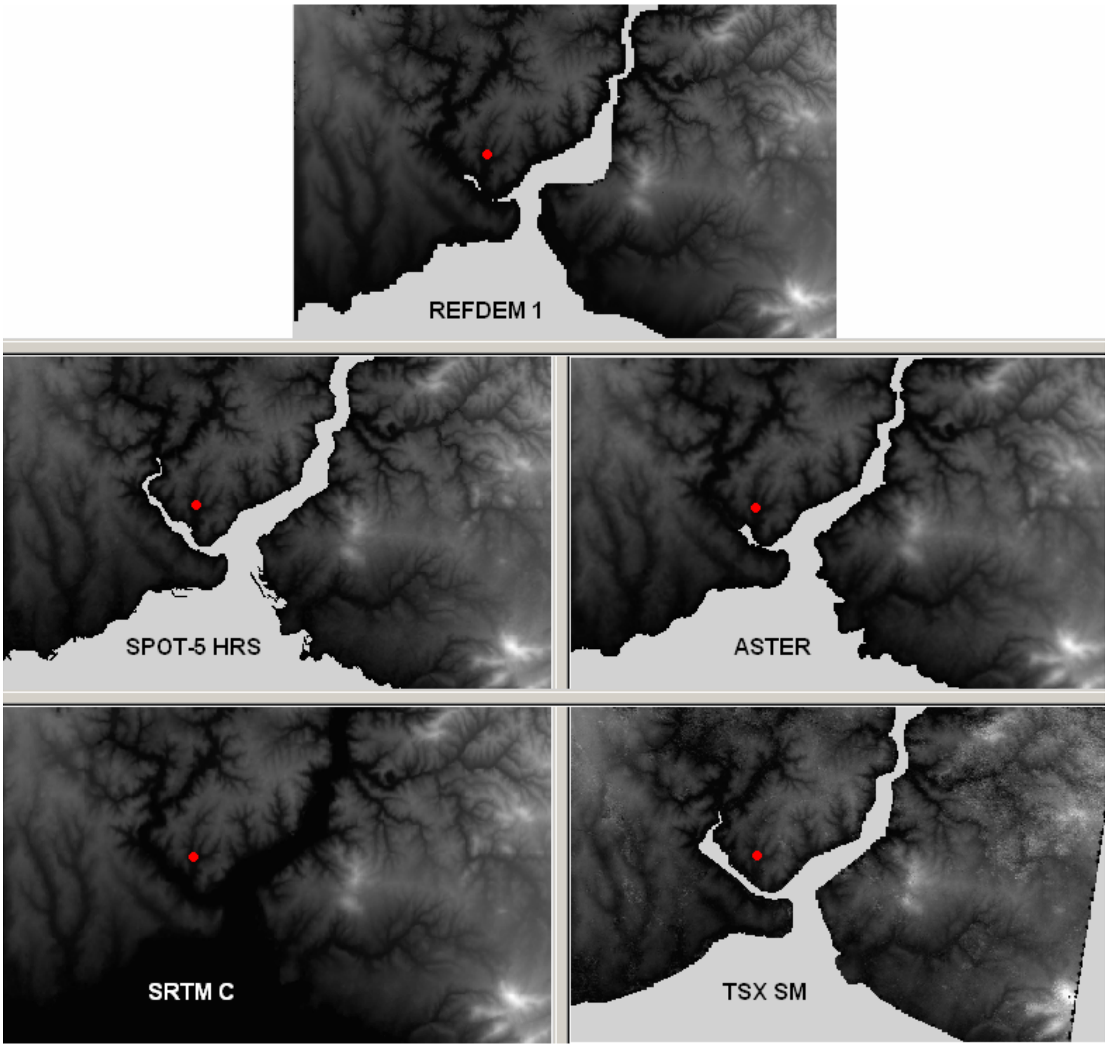

Figure 5.20 Point selection for pre-correction of the shifts by MANI (test field 1).

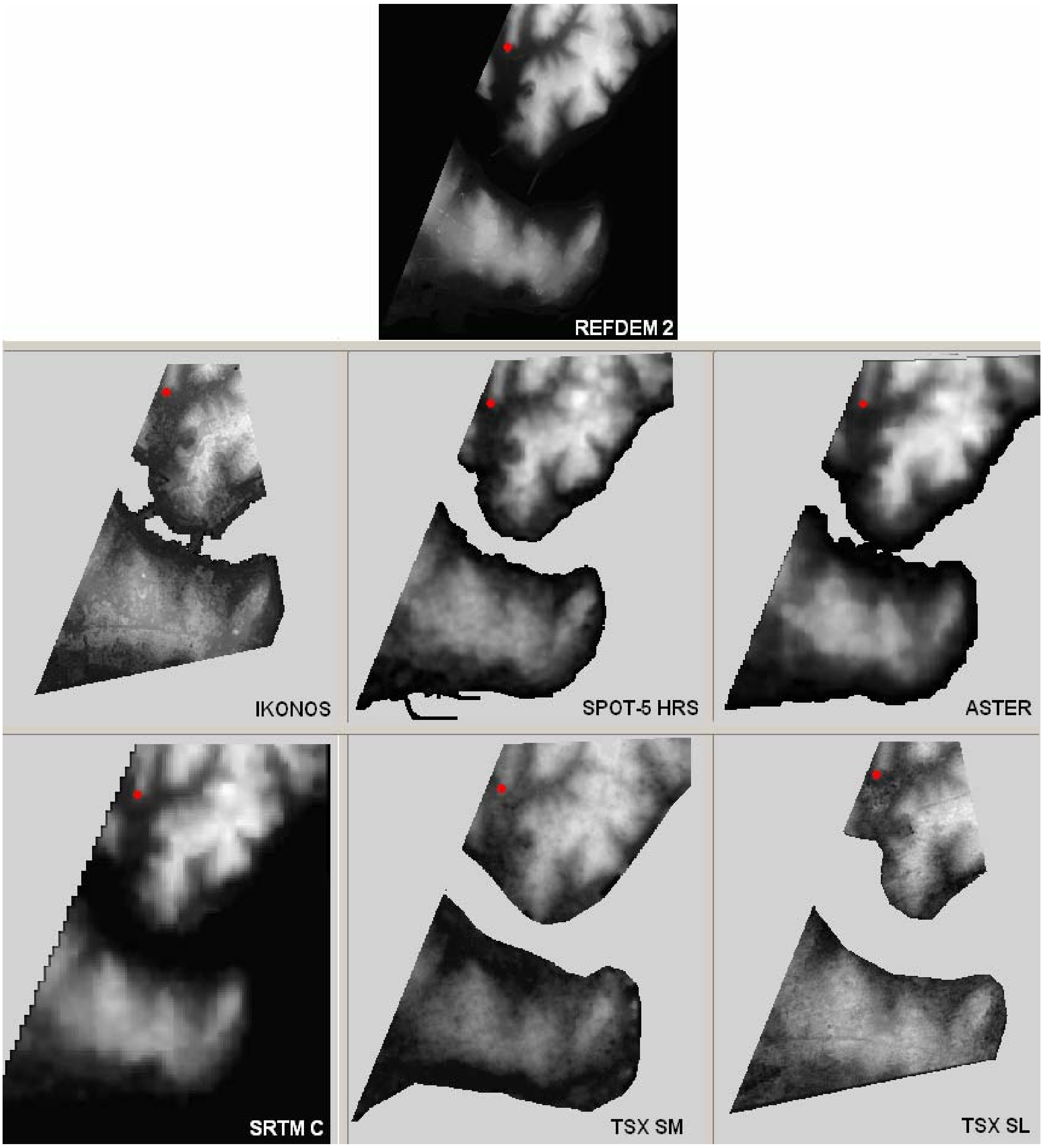

Figure 5.21 Point selection for pre-correction of the shifts by MANI (test field 2).

The Tables 5.1 and 5.2 show the coordinates, and pre-correction of the shifts before DEMSHIFT, adjusted shift values by DEMSHIFT and final RMSZ values for the large test field (test field 1) and Tables 5.3 and 5.4 for the historical peninsula and near surroundings (test field 2).

Table 5.1 Coordinates and pre-correction of shift values before DEMSHIFT (test field 1).

DEM	X before MANI	Y before MANI	Manual shift before DEMSHIFT (-1) × ΔX, ΔY	
			ΔX	ΔY
REFDEM 1	665445	4544805	0	0
SPOT5	665450	4545010	+5	+205
ASTER	665475	4544985	+30	+180
SRTM	665525	4544925	+80	+120
TSX SM	665485	4544965	+40	+160

Table 5.2 Adjusted shifts after pre-correction by MANI and RMSZ values (test field 1).

DEM	Original RMSZ (m)	RMSZ After Manual Shift (m)	Shift by DEMSHIFT (m)		Final RMSZ (m)
			ΔX	ΔY	
SPOT5	15.245	7.215	-29.93	+18.70	5.703
ASTER	15.679	7.459	-14.51	-0.72	6.902
SRTM	12.651	5.431	+27.39	-10.18	4.861
TSX SM	20.256	17.969	0.00	0.00	18.340

Table 5.3 Coordinates and pre-correction of shift values before DEMSHIFT (test field 2).

DEM	X before MANI	Y before MANI	Manual shift before DEMSHIFT (-1) × ΔX, ΔY	
			ΔX	ΔY
REFDEM 2	665421	4544814	0	0
IKONOS	665444	4545001	+10	+193
SPOT5	665450	4545010	+29	+196
ASTER	665475	4544985	+54	+171
SRTM	665525	4544925	+104	+111
TSX SM	665485	4544965	+64	+151
TSX SL	665425	4545008	+4	+194

Table 5.4 Adjusted shifts after pre-correction by MANI and RMSZ values (test field 2).

DEM	Original RMSZ (m)	RMSZ After Manual Shift (m)	Shift by DEMSHIFT (m)		Final RMSZ (m)
			ΔX	ΔY	
IKONOS	13.666	7.443	-11.38	+8.03	7.318
SPOT5	13.311	5.631	-12.31	+5.94	5.304
ASTER	12.777	5.953	+13.58	-12.03	5.777
SRTM	8.275	5.924	+50.38	-10.11	4.464
TSX SM	16.194	13.208	-12.91	-38.35	12.985
TSX SL	13.784	8.444	-7.93	+21.44	8.249

5.3 ACCURACY ANALYSIS OF DSMs

After shifting of DEMs, the accuracies of them have been analyzed in relation to the reference DEMs of the test fields separately for open and forest areas using program DEMANAL (section 4.3.1.4). For the analysis by DEMANAL, the maximal accepted DZ was limited as 50m and the maximal accepted tangent of terrain inclination was selected as 1.00. In the second iteration, shift and vertical scale were respected. These settings were made depending upon the characteristic of the test fields.

For the separation of the open and forest areas, layers with the grey value 0 for the forest areas and 255 for the open areas were used. The created classification image for open and forest areas can be seen in Figure 5.22; the blue part is sea and has no effect on the results.

In the following sections the results of accuracy analysis will be displayed separately for optical and SAR satellite's height models. In the tables, SZ means standard deviation of Z, NAP means 'not accepted points' which have height difference exceeding 50m against the reference and α= slope.

Figure 5.22 Classification image of open and forest areas (White= open areas, black= forest areas, blue= sea).

5.3.1 Absolute Accuracy Analysis of DSMs

5.3.1.1 Absolute Accuracy Analysis of DSMs Based on Optical Images

As mentioned before, in this study, the height models based on stereo image-pairs of IKONOS, SPOT-5 HRS and ASTER have been used for the analysis.

IKONOS

The accuracy analysis of IKONOS height model have been performed just for the test field 2 because it does not overlap with test field 1. In Table 5.5 the results of absolute accuracy analysis for IKONOS can be seen.

Test Field 2

Accuracy analysis have been performed for the smaller test field 2 to compare the results of entire height models with TSX SL model in same interest area. With this aim, all height models have been reduced into the sizes of test field 2. Following Tables and Figures show the results of accuracy analysis for IKONOS DSM against REFDEM 2. Nearly full area of test field 2 is built-up area and the forest coverage is so less. That is why the accuracy analysis were performed just for general area not separate for open and forest layers.

Table 5.5 Accuracy of IKONOS height model for test field 2.

DSM	General	
	SZ [m]	NAP[%]
IKONOS	7.04+1.03×tan(α)	0.00

The frequency distribution of DZ values between evaluated models and reference models are shown in Figure 5.23. The components of this graphic are achieved from the list file of program DEMANAL after the analysis and generated using Microsoft Excel. The height differences and the corresponding number of points can be seen in this graphic presentation. The main point which should be analyzed in this graphic is the symmetric distribution. If the frequency distribution is symmetric, no influence of the buildings and vegetation exist. In this study, these graphic visualizations have been prepared between all evaluated models and reference models to form an opinion about the frequency distribution of DZ values. Figure 5.23 shows the frequency distribution of DZ values between IKONOS DSM and REFDEM 2.

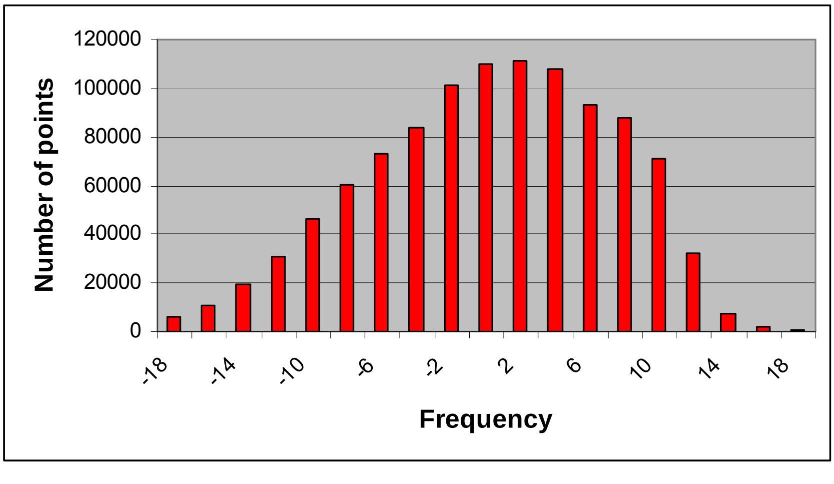

Figure 5.23 Height differences distribution of DZ between IKONOS DSM and REFDEM 2 (test field 2).

As mentioned before, at the accuracy analysis of heights, for the elimination of blunders, the maximal accepted DZ value is selected to 50m in program DEMANAL and the points which exceed this threshold value are automatically excluded by the program. If the image of this exception process is generated, the parts which are constituted by eliminated points can be identified clearly. By this way, these parts which have problems can be excluded when the models will be used for the precise applications. Using program DEMANAL, images have been created containing the excluded points. Figure 5.24 illustrates the image which contains the excluded points for IKONOS DSM against REFDEM 2. The excluded points are represented by the dark spots.

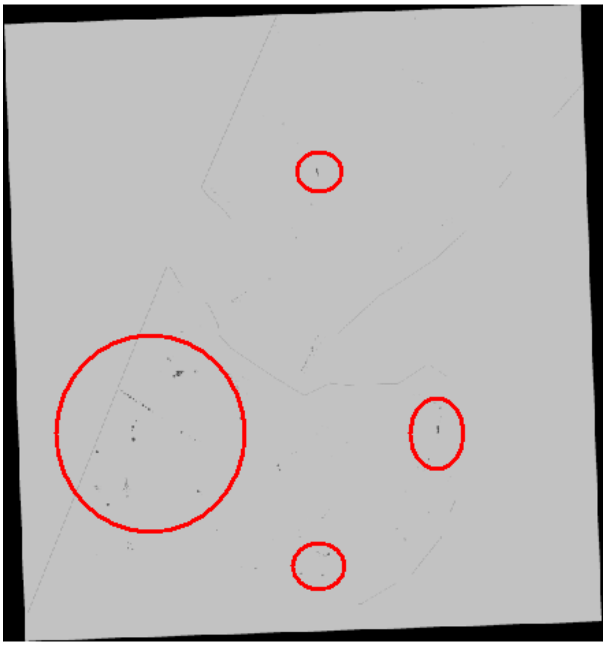

Figure 5.24 Excluded points (IKONOS, test field 2).

Besides these information's, RMSE of evaluated models against reference models as a function of the terrain inclination direction (aspects) can be visualized using program HPSHOW. Especially, in SAR imagery the accuracy shows dependency upon the aspects. As mentioned above aspects are the functions of the terrain inclination direction and present information about the mean value, the situation for zero inclination, factor for multiplication 'tan(slope)' and for average inclination. Considering aspects, the most effective contents on the accuracy results can be appeared easily. Figure 5.25 shows the aspects of the accuracy analysis between IKONOS stereo model and REFDEM 2.

As expected, the IKONOS DSM shows no dependency upon the aspects.

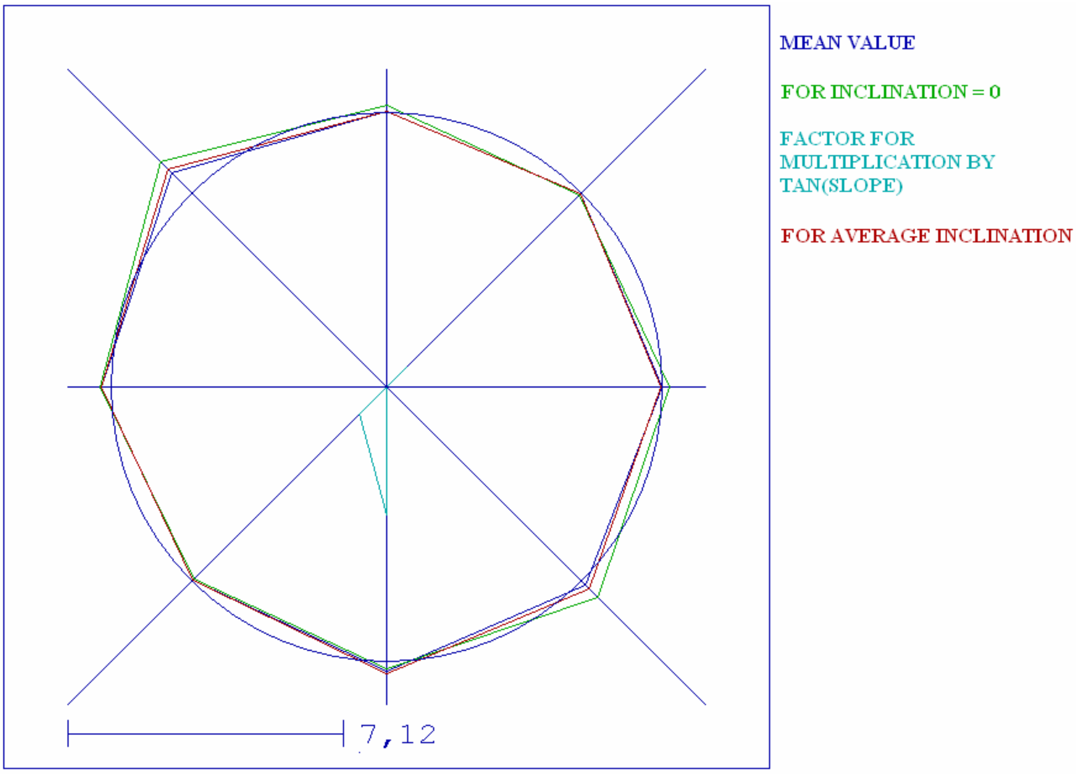

Figure 5.25 Aspects of the accuracy analysis (IKONOS, test field 2).

SPOT-5 HRS

Test Field 1

Table 5.6 shows the results of accuracy analysis between SPOT-HRS DSM against REFDEM 1 separately for open, forest areas and for the whole area. The following Figure 5.26 represents the frequency distribution of DZ values.

Table 5.6 Accuracy of SPOT-5 HRS DSM for test field 1.

DSM	Open Areas (79.60%)		Forest Areas (19.51%)		Whole area	
	SZ [m]	NAP [%]	SZ [m]	NAP [%]	SZ [m]	NAP [%]
SPOT5 (20m)	4.54 +5.96×tan(α)	0.01	5.38 +3.98×tan(α)	0.00	4.88 +5.45×tan(α)	0.01

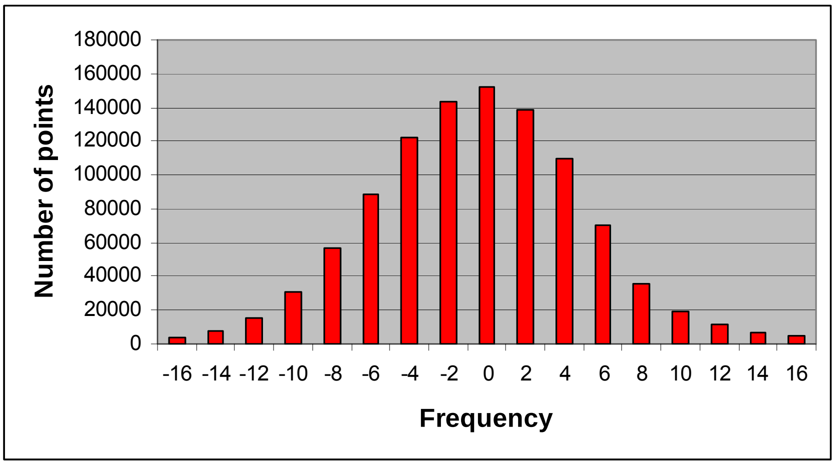

Figure 5.26 Height differences distribution of DZ between SPOT-5 HRS DSM and REFDEM 1 (test field 1).

Figure 5.27 shows the created image which contains the excluded points and the Figure 5.28 represents the aspect analysis.

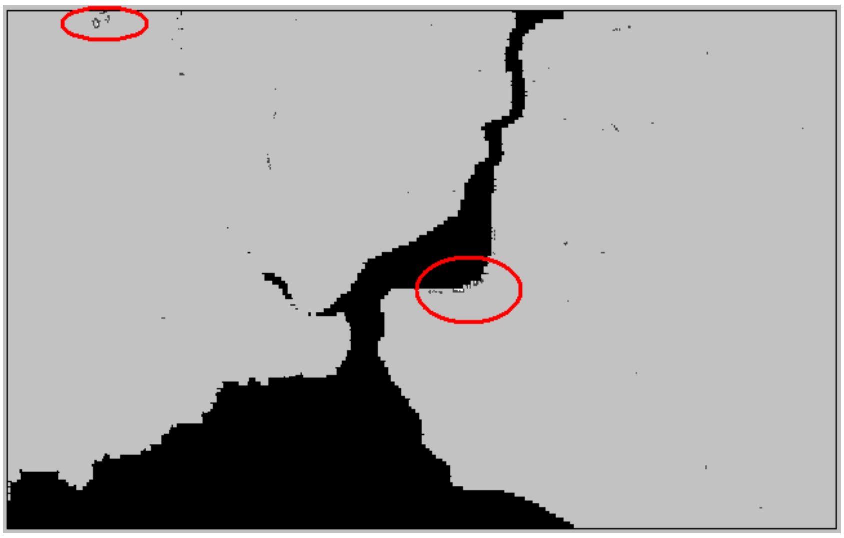

Figure 5.27 Excluded points (SPOT-5 HRS, test field 1).

Test Field 2

Table 5.7 shows the results of the accuracy analysis for SPOT-HRS DSM against REFDEM 2 and Figure 5.29 illustrates the frequency distribution of DZ.

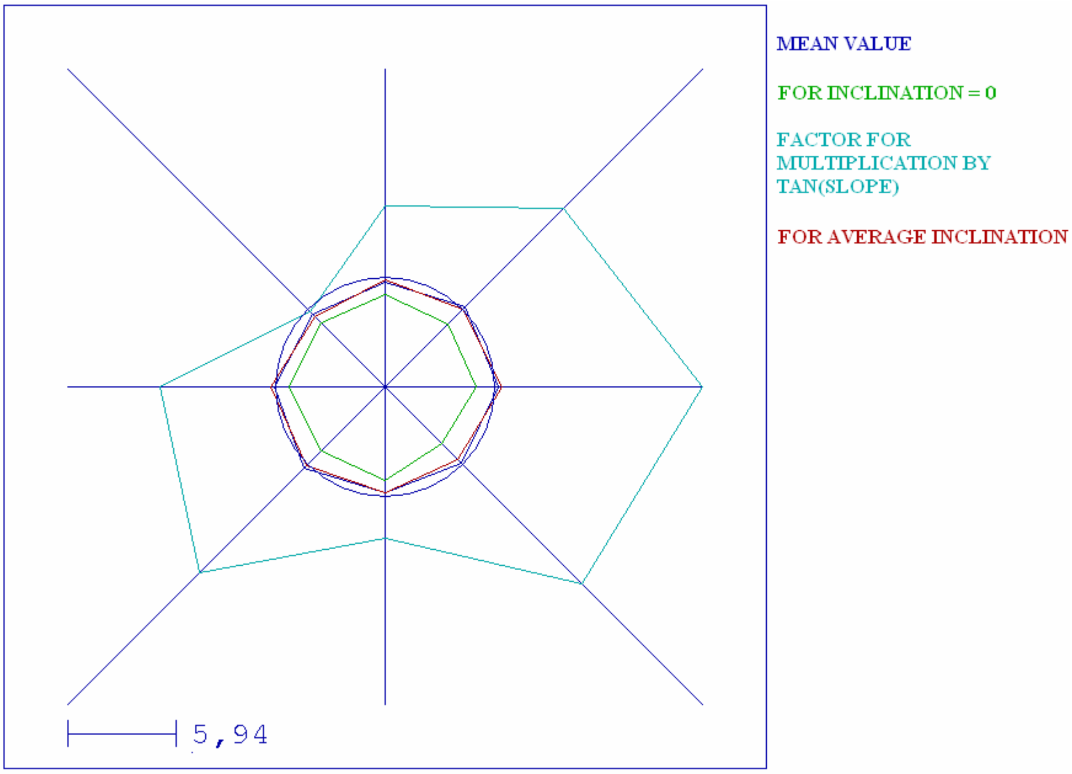

Figure 5.28 Aspects of the accuracy analysis (SPOT-5 HRS, test field 1).

Table 5.7 Accuracy of SPOT-5 HRS DSM for test field 2.

DSM	General	
	SZ (m)	NAP(%)
SPOT5 (20m)	5.13+2.17×tan(α)	0.00

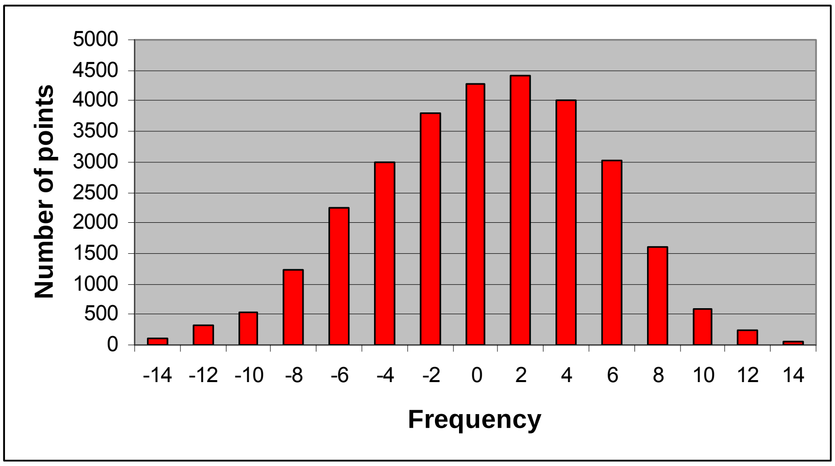

Figure 5.29 Height differences distribution of DZ between SPOT-5 HRS DEM and REFDEM 2 (test field 2).

Figure 5.30 shows the excluded points and Figure 5.31 represents the aspect of analysis.

Figure 5.30 Excluded points (SPOT-5 HRS, test field 2).

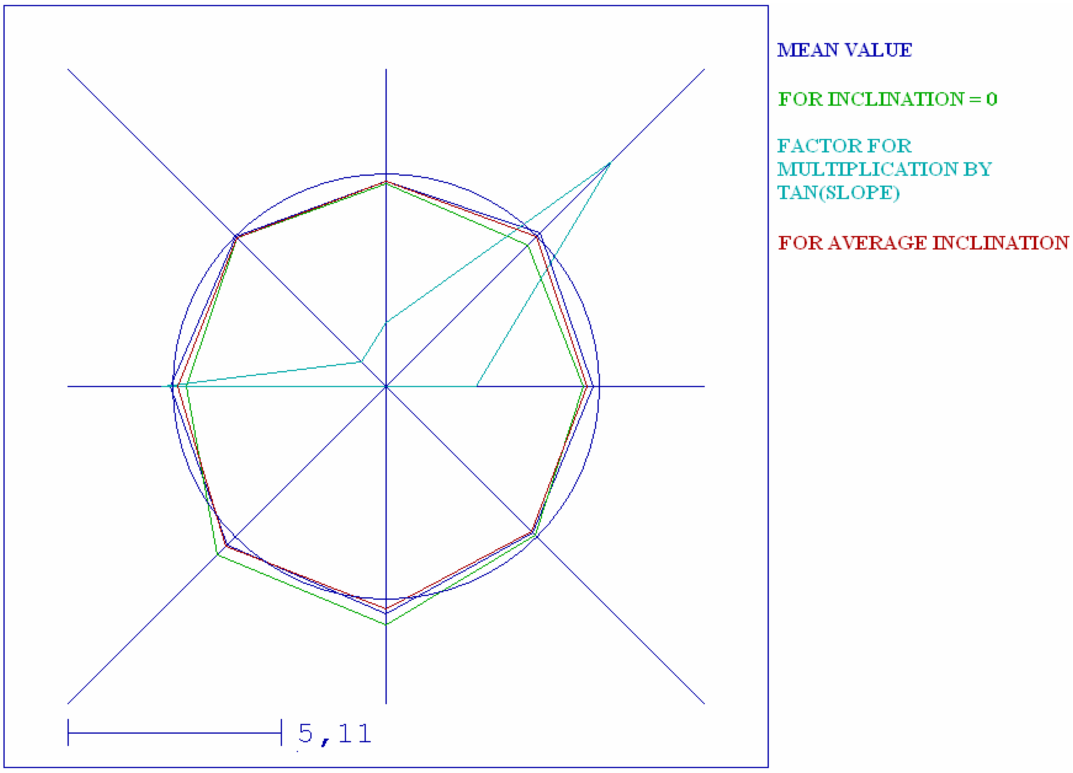

Figure 5.31 Aspects of the accuracy analysis (SPOT-5 HRS, test field 2).

ASTER

Test Field 1

Table 5.8 shows the results of accuracy analysis between ASTER DSM against REFDEM 1 separately for open, forest layers and whole area. Figure 5.32 represents the frequency distribution of DZ values.

Table 5.8 Accuracy of ASTER DSM for test field 1.

DSM	Open Areas (79.60%)		Forest Areas (19.51%)		General	
	SZ [m]	NAP [%]	SZ [m]	NAP [%]	SZ [m]	NAP [%]
ASTER (30m)	5.48 +6.63×tan(α)	0.03	4.78 +10.16×tan(α)	0.08	5.65 +6.63×tan(α)	0.03

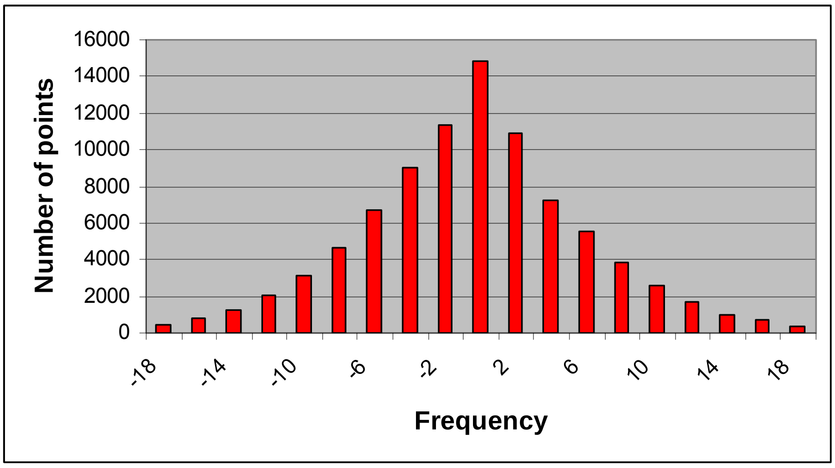

Figure 5.32 Height differences distribution of DZ between ASTER DSM and REFDEM 1 (test field 1)

Figure 5.33 shows the excluded points and Figure 5.34 represents the aspects.

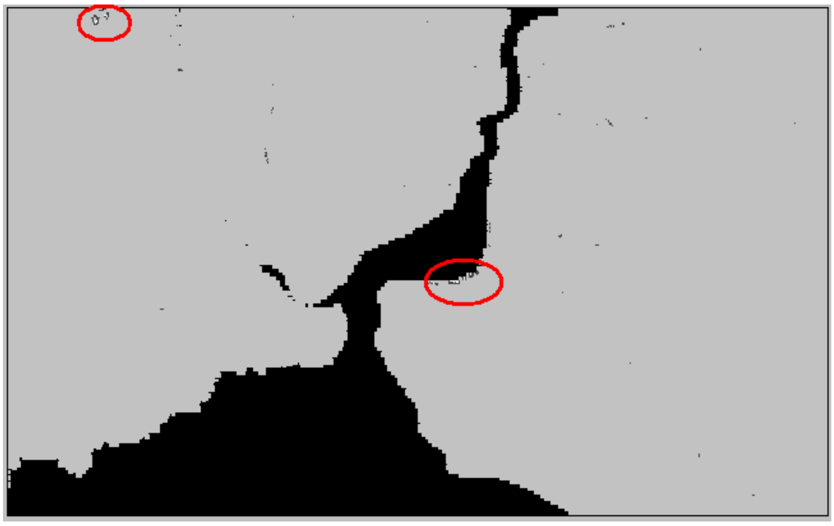

Figure 5.33 Excluded points (ASTER, test field 1).

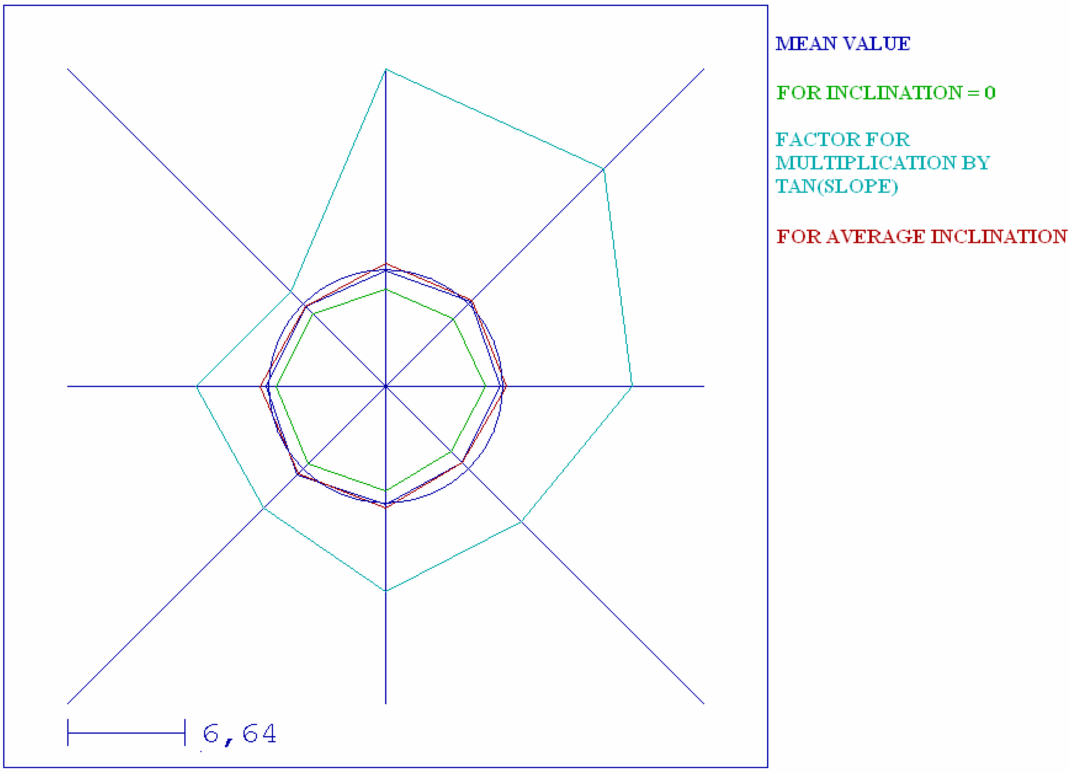

Figure 5.34 Aspects of the accuracy analysis (ASTER, test field 1).

Test Field 2

Table 5.9 shows the results of the accuracy analysis for ASTER DSM against REFDEM 2 and Figure 5.35 the frequency distribution of DZ.

Table 5.9 Accuracy of ASTER DSM for test field 2.

DSM	General	
	SZ [m]	NAP[%]
ASTER (30m)	5.13+2.17×tan(α)	0.00

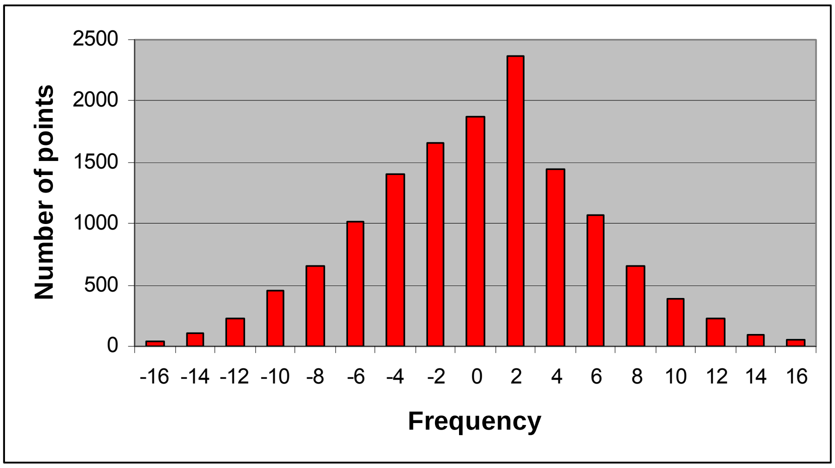

Figure 5.35 Height differences distribution of DZ between ASTER DSM and REFDEM 2 (test field 2)

Figure 5.36 shows the excluded points and Figure 5.37 the aspects.

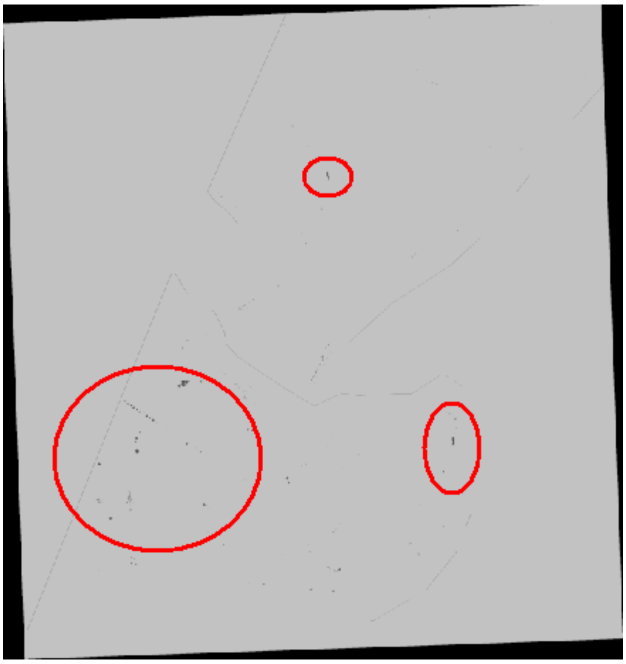

Figure 5.36 Excluded points (ASTER, test field 2).

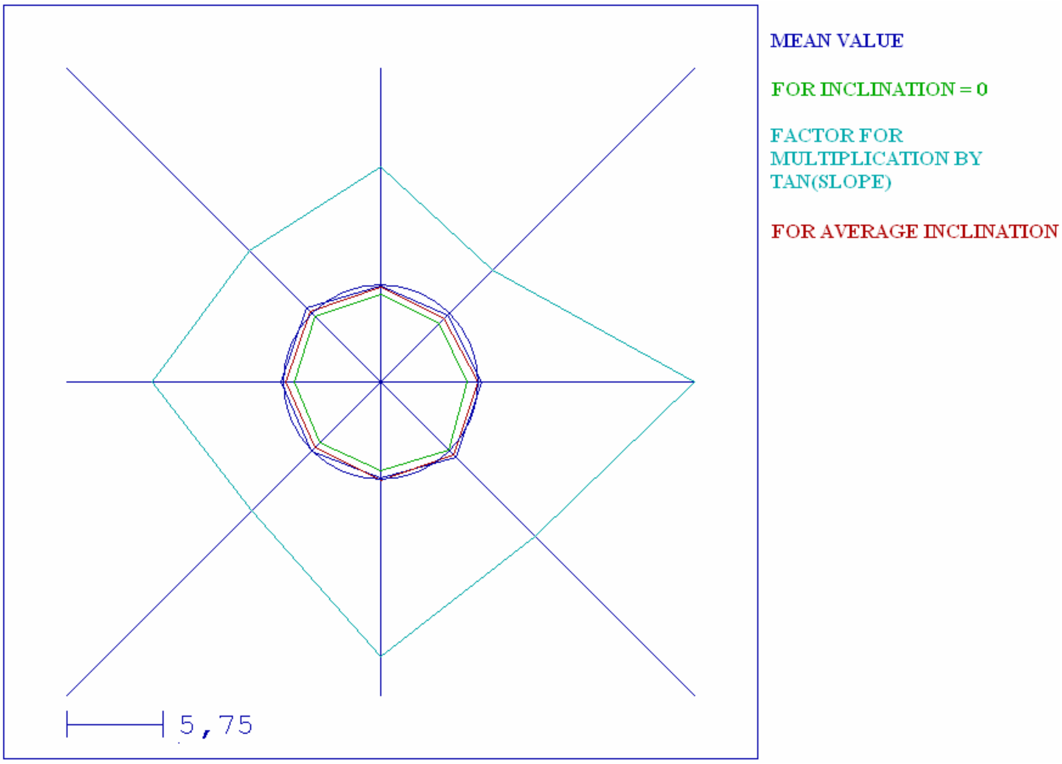

Figure 5.37 Aspects of the accuracy analysis (ASTER, test field 2).

5.3.1.2 Absolute Accuracy Analysis of InSAR DSMs

As explained before, in this study, SRTM C-band, TSX SM and high resolution TSX SL mode InSAR height models have been analyzed. In this section, the results of accuracy analysis of these height models have been exhibited sequentially starting with SRTM C-band.

SRTM C-Band

Test Field 1

Table 5.10 represents the results of accuracy analysis between SRTM C-band DSM against REFDEM 1 separately for open, forest area and whole area. Figure 5.38 illustrates the frequency distribution of DZ values.

Figure 5.39 shows the excluded points and Figure 5.40 illustrates the aspects of the accuracy analysis.

Table 5.10 Accuracy of SRTM C-band DSM for test field 1.

DSM	Open Areas (79.60%)		Forest Areas (19.51%)		Whole area	
	SZ [m]	NAP [%]	SZ [m]	NAP [%]	SZ [m]	NAP [%]
SRTM (70m)	3.20 +8.67×tan(α)	0.01	3.32 +9.29×tan(α)	0.00	3.38 +8.11×tan(α)	0.01

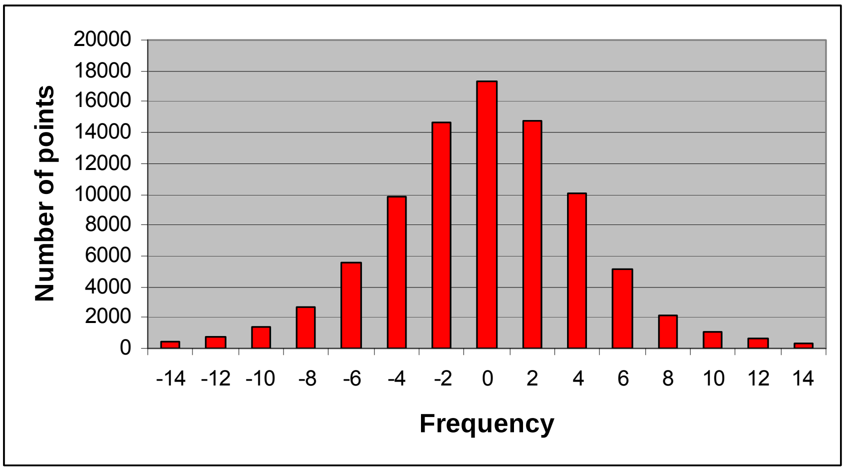

Figure 5.38 Height differences distribution of DZ between SRTM C-band DSM and REFDEM 1 (test field 1).

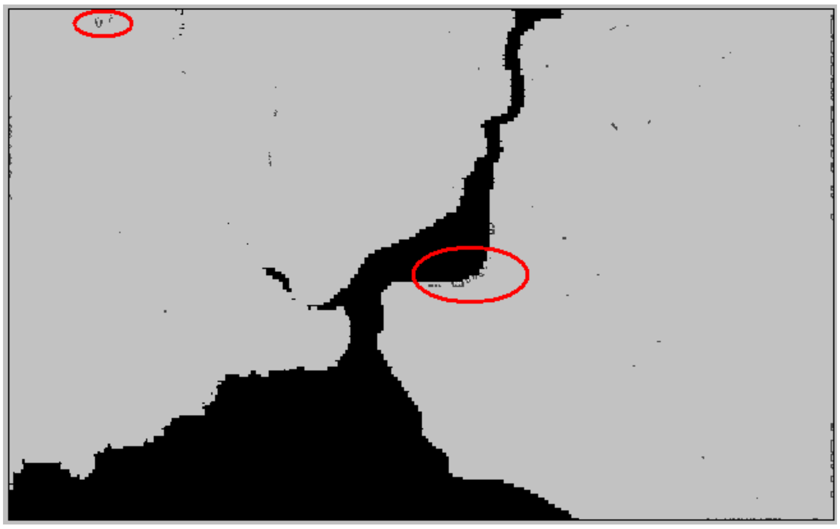

Figure 5.39 Excluded points (SRTM C-band, test field 1).

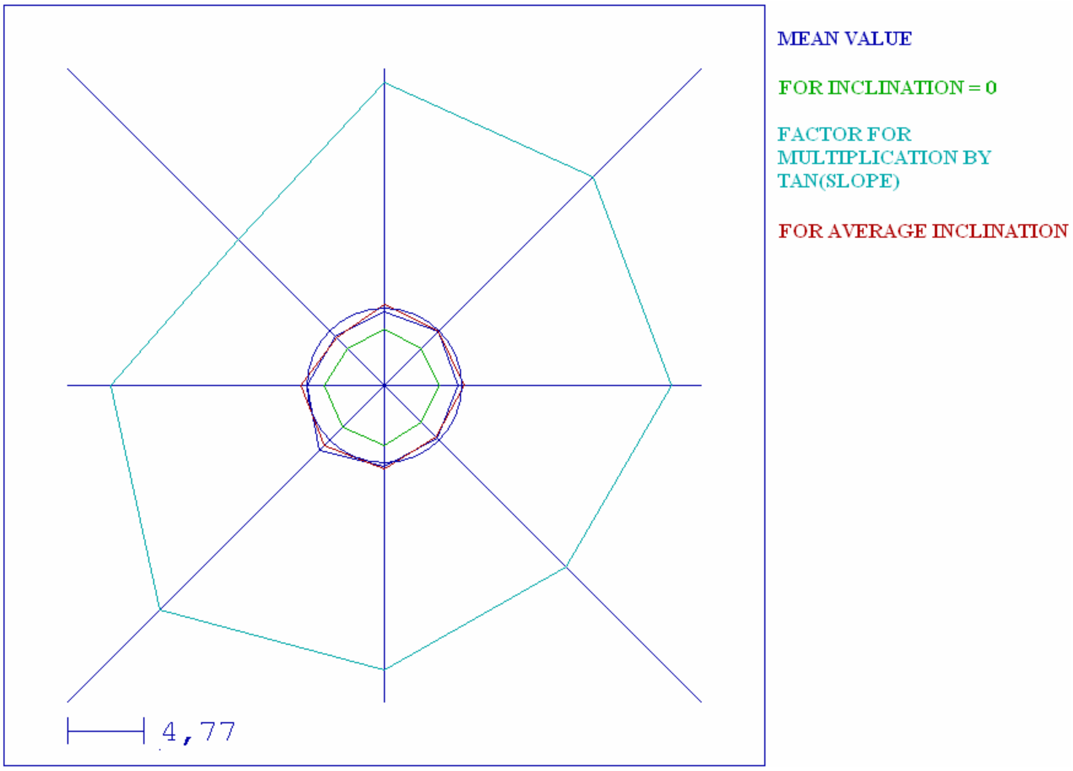

Figure 5.40 Aspects of the accuracy analysis (SRTM C-band, test field 1).

Test Field 2

Table 5.11 shows the results of absolute accuracy analysis for SRTM C-band DSM against REFDEM 2 and Figure 5.41 illustrates the frequency distribution of DZ between them for general accuracy analyses.

Table 5.11 Accuracy of SRTM C-band DSM for test field 2.

DSM	whole area	
	SZ (m)	NAP(%)
SRTM (70m)	$2.61+12.98\times\tan(\alpha)$	0.00

Figure 5.42 shows the excluded points and Figure 5.43 the aspect.

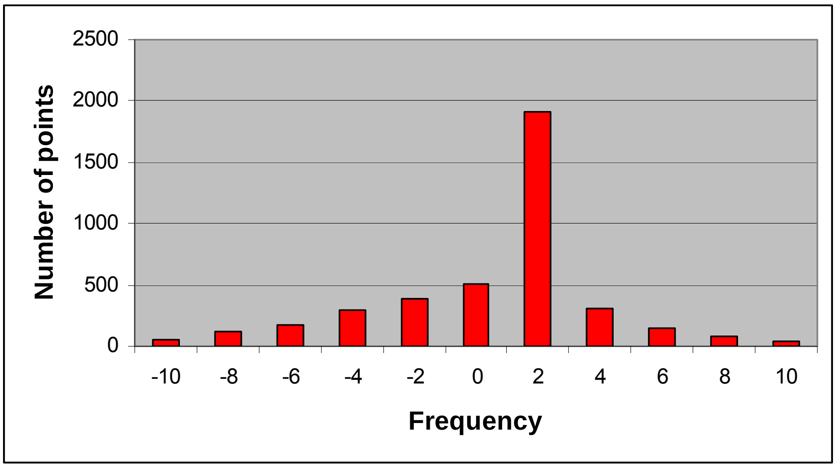

Figure 5.41 Height differences distribution of DZ between SRTM C-band DSM and REFDEM 2 (test field 2).

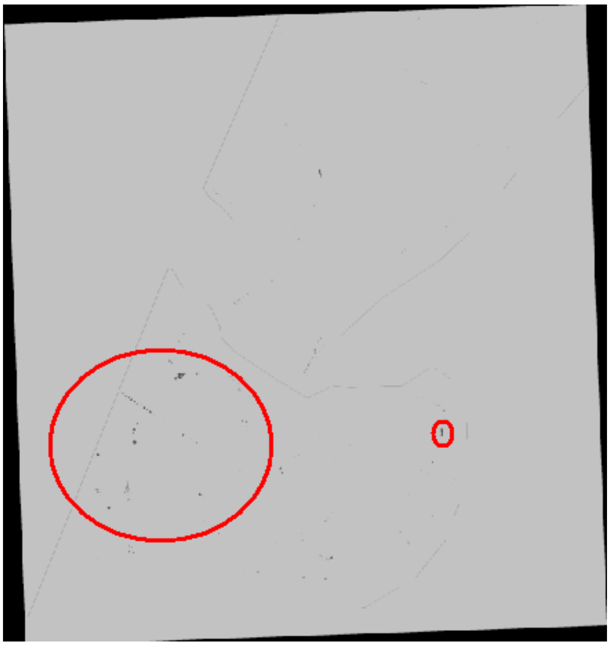

Figure 5.42 Excluded points (SRTM C-band, test field 2).

TSX SM

Test Field 1

Table 5.12 shows the results of accuracy analysis between TSX SM DSM against REFDEM 1 separately for open, forest layers and the whole area. Figure 5.44 represents the frequency distribution of DZ values.

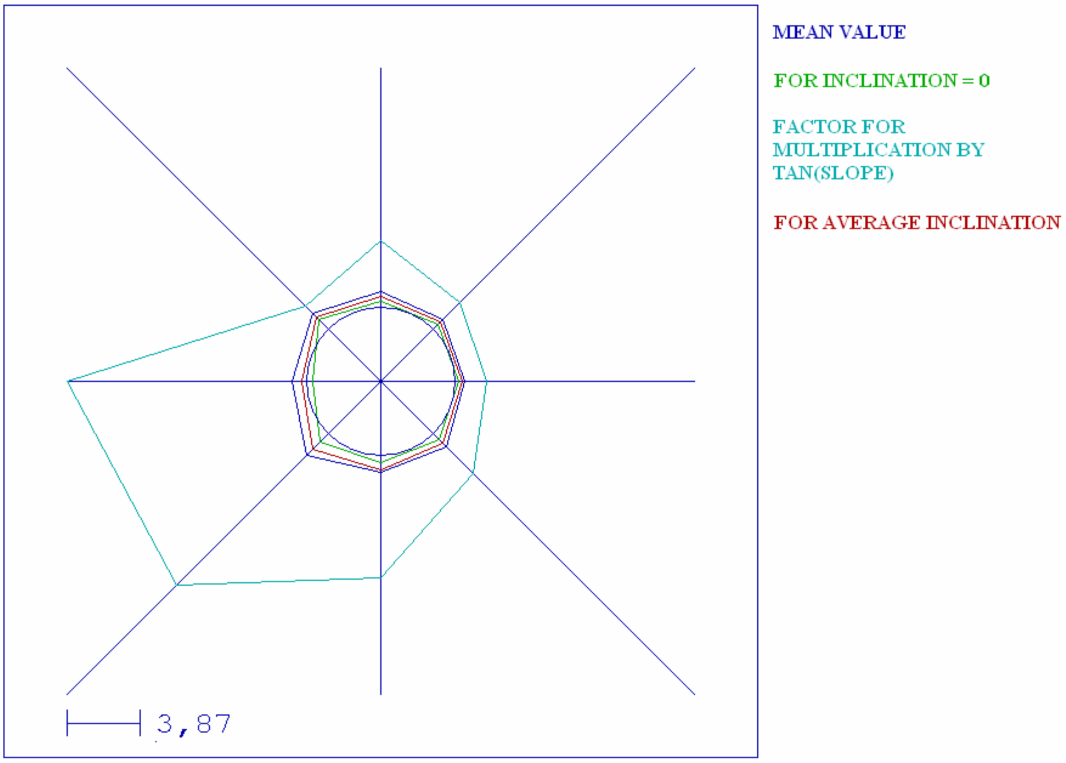

Figure 5.43 Aspects of the accuracy analysis (SRTM C-band, test field 2).

Table 5.12 Accuracy of TSX SM DSM for test field 1.

DEM	Open Areas (79.60%)		Forest Areas (19.51%)		Whole area	
	SZ [m]	NAP [%]	SZ [m]	NAP [%]	SZ [m]	NAP [%]
TSX SM (10m)	14.65 +12.72×tan(α)	0.43	18.26 +1.96×tan(α)	2.38	14.98 +11.89×tan(α)	0.73

Usually 3863058 points were used for this comparison and just the 0.73% (28288 points) of them exceeded the maximal accepted ΔZ value (50m) however because of the smaller grid size against the other DSMs, the number of excluded points (shown by white spots) are more. For recognizing the distribution of these excluded points, DEMANAL generates graphical overviews for open and forest layers of TSX SM height model as seen in Figure 5.46.

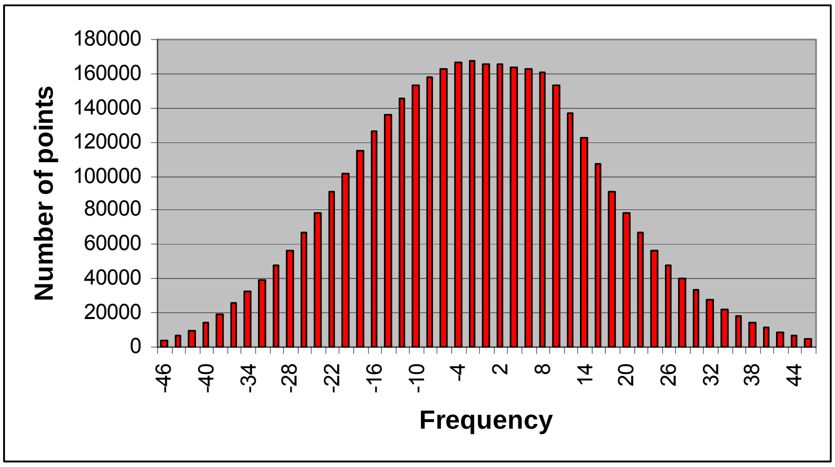

Figure 5.44 Height differences distribution of DZ between TSX SM DSM and REFDEM 1 (test field 1).

Figure 5.45 shows the excluded points.

Figure 5.45 Excluded points (TSX SM, test field 1).

At the left hand side of Figure 5.46, the bright and dark regions represent open and forest areas. For the analysis of open areas, 3261035 points were used for comparison and 14041 (0.43%) of them exceeded the maximal accepted DZ value. On the right hand side of Figure 5.46, the bright regions represent forest and dark regions represent the open areas. For the analysis of the forest areas, 616354 points were used for comparison and 15045 (2.38%) points were excluded.

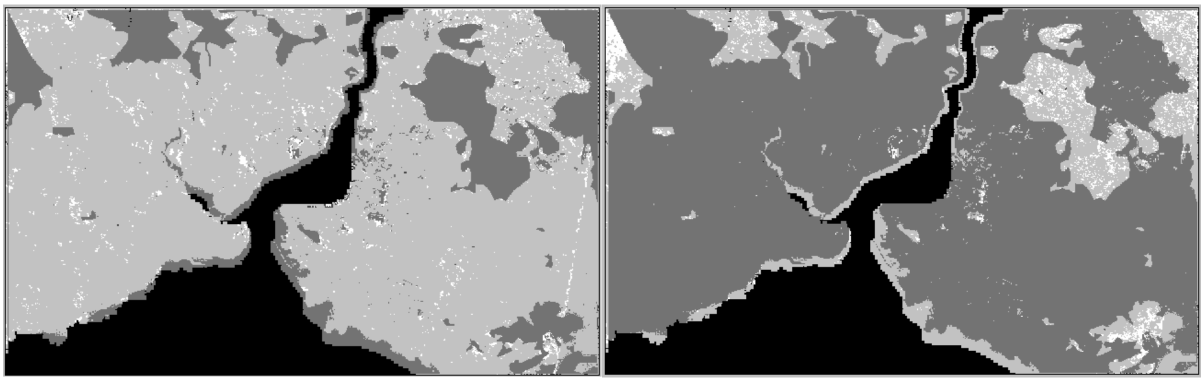

Figure 5.46 Excluded points for open and forest areas (TSX SM, test field 1).

Figure 5.47 represents the aspects for the whole area.

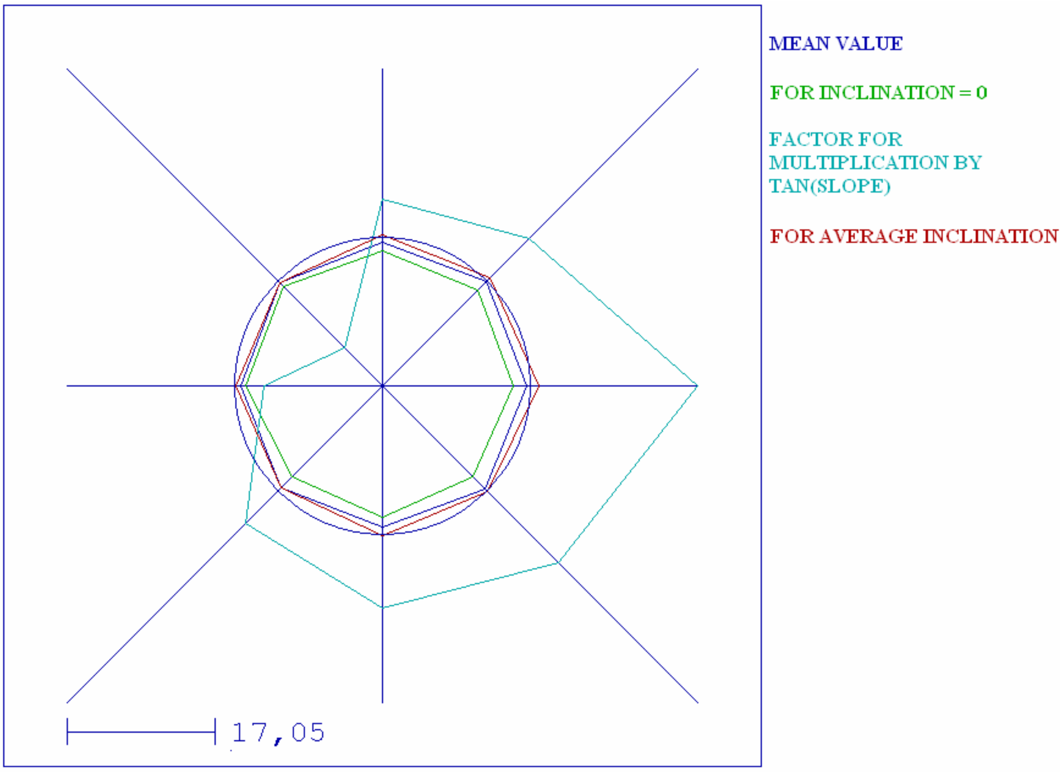

Figure 5.47 Aspects of the accuracy analysis (TSX SM, test field 1).

Test Field 2

Table 5.13 shows the results of the accuracy analysis for TSX SM DSM against REFDEM 2 and Figure 5.48 the frequency distribution of DZ between them.

Table 5.13 Accuracy of TSX SM DSM for test field 2.

DEM	Whole area	
	SZ [m]	NAP[%]
TSX SM (10m)	10.51+17.93×tan(α)	0.06

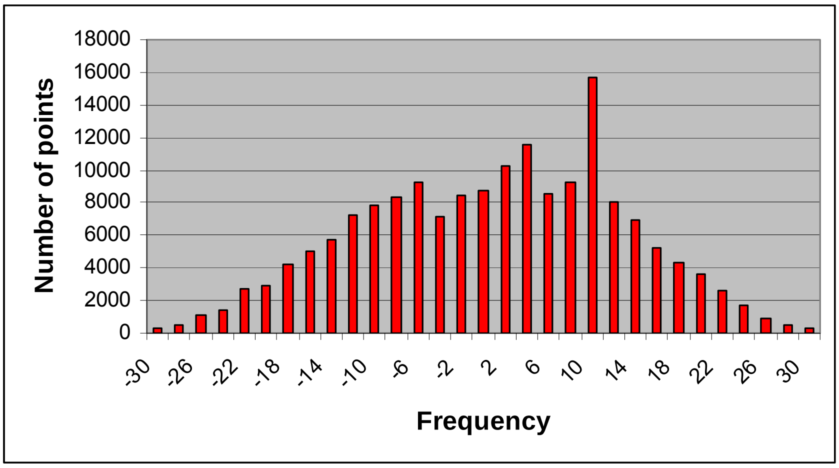

Figure 5.48 Height differences distribution of DZ between TSX SM DSM and REFDEM 2 (test field 2)

Figure 5.49 shows the excluded points and Figure 5.50 illustrates the aspects.

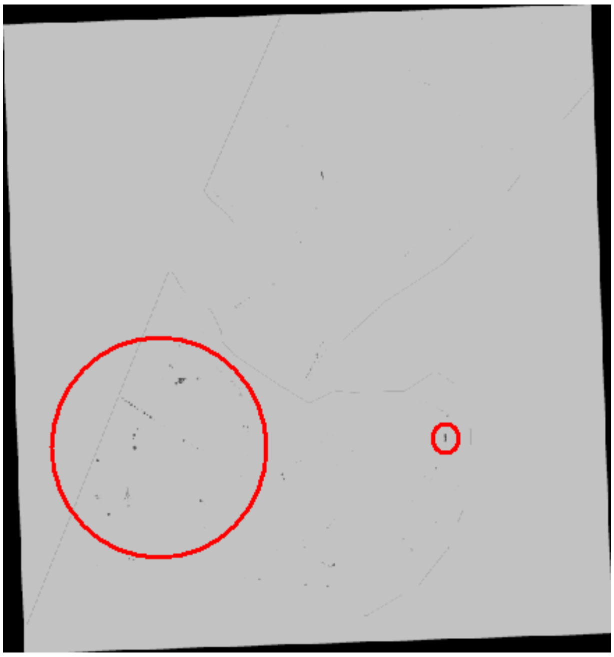

Figure 5.49 Excluded points (TSX SM, test field 2).

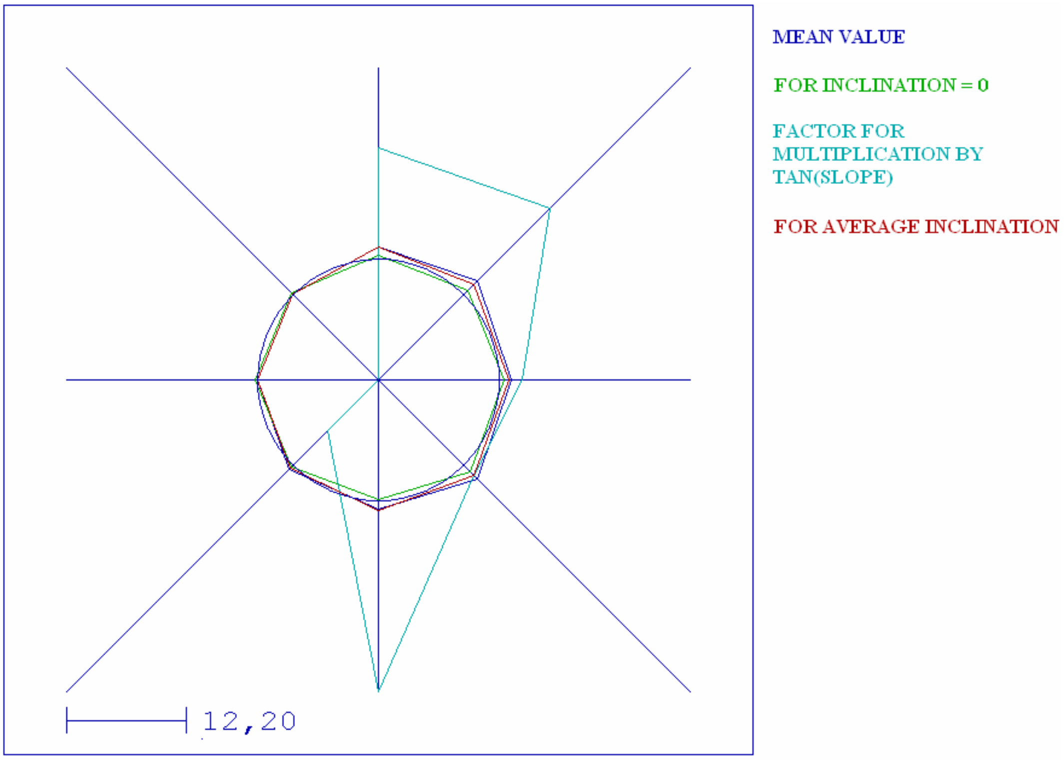

Figure 5.50 Aspects of the accuracy analysis (TSX SM, test field 2).

TSX SL

The accuracy analysis of TSX SL DSM has been performed just for the test field 2 because it does not overlap with test field 1.

Test Field 2

Table 5.14 shows the results of accuracy analysis for TSX SL DSM against REFDEM 2 and Figure 5.51 illustrates the frequency distribution of DZ between them for the whole area.

Table 5.14 Accuracy of TSX SL DSM for test field 2.

DSM	Whole area	
	SZ [m]	NAP[%]
TSX SL (3m)	7.09+11.22×tan(α)	0.00

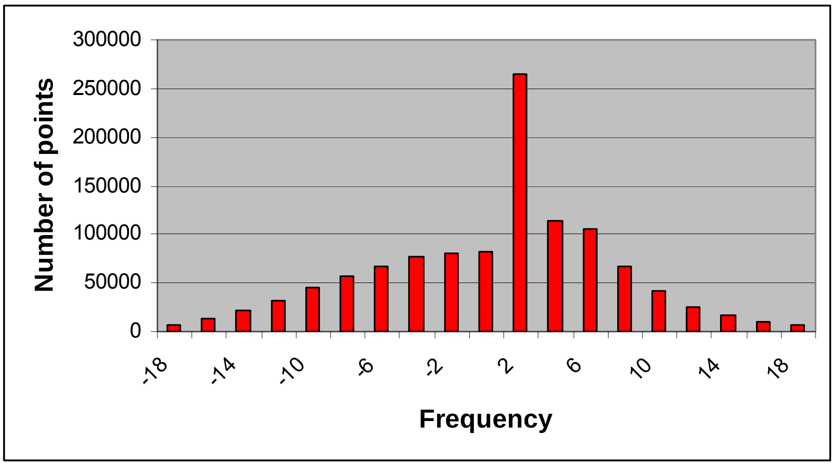

Figure 5.51 Height differences distribution of DZ between TSX SL DSM and REFDEM 2 (test field 2).

Figure 5.52 shows the excluded points and Figure 5.53 illustrates the aspects.

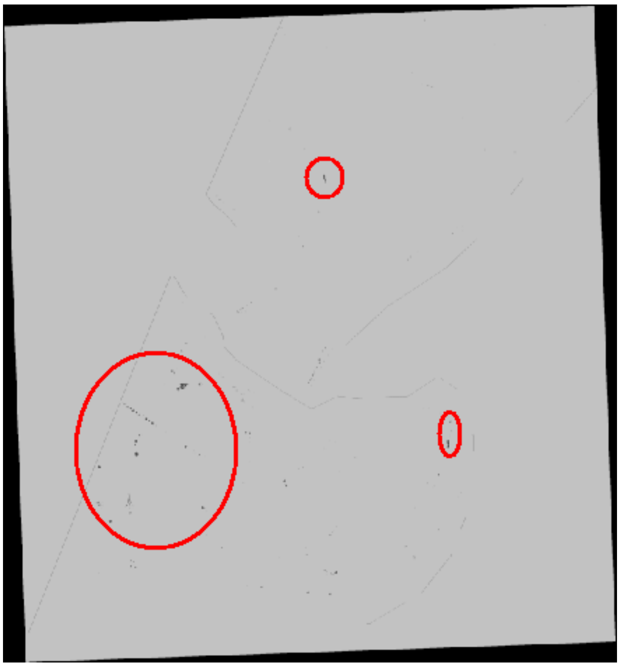

Figure 5.52 Excluded points (TSX SL, test field 2).

An overview of the accuracy analysis for test field 1 is shown in Table 5.15 below.

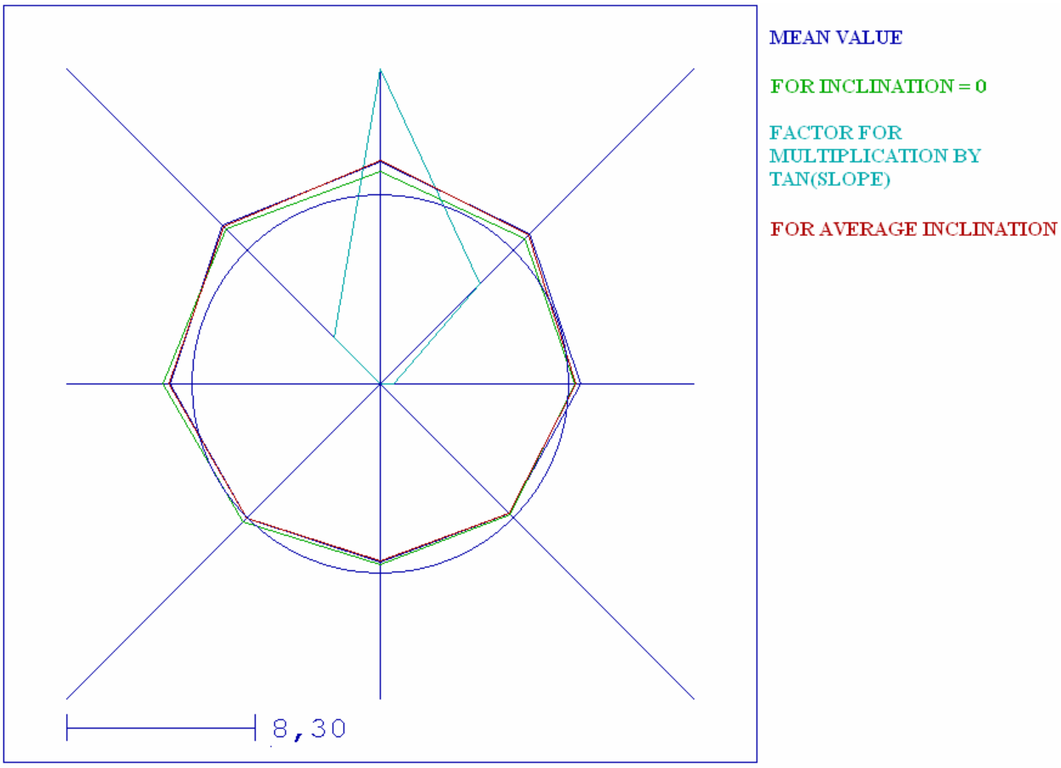

Figure 5.53 Aspects of the accuracy analysis (TSX SL, test field 2).

Table 5.15 Overview of accuracy for test field 1.

DEM	Open Areas (79.60%)		Forest Areas (19.51%)		whole area	
	SZ [m]	NAP [%]	SZ [m]	NAP [%]	SZ [m]	NAP [%]
SPOT5 (20m)	4.54 +6.22×tan(α)	0.01	5.41 +4.24×tan(α)	0.04	4.88 +5.73×tan(α)	0.01
ASTER (30m)	5.48 +6.63×tan(α)	0.03	4.78 +10.16×tan(α)	0.08	5.65 +6.63×tan(α)	0.03
SRTM (70m)	3.20 +8.67×tan(α)	0.01	3.32 +9.29×tan(α)	0.00	3.38 +8.11×tan(α)	0.01
TSX SM (10m)	14.63 +12.84×tan(α)	0.42	18.25 +1.83×tan(α)	2.35	14.98 +11.89×tan(α)	0.73

An overview of accuracy analysis for test field 2 is shown in Table 5.16.

Table 5.16 Overview of accuracy for test field 2.

DEM	Whole area	
	SZ [m]	NAP[%]
IKONOS (3m)	7.02 +1.12×tan(α)	0.00
SPOT5 (20m)	5.05 +0.14×tan(α)	0.00
ASTER (30m)	4.75 +8.98×tan(α)	0.00
SRTM (70m)	2.61 +12.98×tan(α)	0.00
TSX SM (10m)	10.51 +17.93×tan(α)	0.06
TSX SL (3m)	7.09 +11.22×tan(α)	0.00

5.3.2 Relative Accuracy Analysis of DSMs

Besides the absolute accuracy assessments the relative accuracies (relative standard deviations) of evaluated DEMs have been identified in the study. As distinct from absolute accuracies, relative accuracies indicate the interior accuracy of a model that means a point in relation to the neighbored points.

$$RSX = \sqrt{\sum (dxi - dxj)^2 / (2 \times nx)} \tag{5.1}$$

RSX = relative standard deviation

d = distance between points

dl < d < du dl = lower distance limit du = upper distance limit of the distance

The relative accuracy is important for the morphologic details. The morphologic details for example, are not influenced by an error of phase unwrapping, leading to a local absolute error of the DSM, but not to a relative error of closely neighbored points.

In this study, for the evaluation of relative accuracy, the accuracy from each point to the neighbored points was calculated for each evaluated DEM. For example, for a DEM has 30m grid spacing the relative accuracies were calculated between 30m and 300m at the 30m distance interval. The relative accuracies of the evaluated DEMs for test field 1 and 2 can be seen sequentially in this part. Depending upon the reference model's grid spacing, the relative accuracies have been calculated from 30m to 300m in test field 1 and 1m to 10m in test field 2.

5.3.2.1 Relative Accuracy Analysis of DSMs Based on Optical Images

IKONOS

As mentioned before, IKONOS height model covers only test field 2 that's why the relative accuracies have been calculated just for this test field.

Test Field 2

Table 5.17 shows the results of relative accuracy analysis for IKONOS DSM against REFDEM 2 in test field 2 with the regular distance interval corresponding to reference DEM's grid spacing.

SPOT-5 HRS DSM

Test Field 1

Table 5.18 shows the results of relative accuracy analysis for SPOT-5 HRS DEM against REFDEM 1 at the test field 1 separately for open, forest layers and the whole area with the regular distance interval corresponding with reference DEM's grid spacing.

Table 5.17 Relative accuracies of IKONOS DSM (test field 2).

Distance [m]	SZ General [m]
1	.98
2	1.63
3	2.14
4	2.57
5	2.92
6	3.23
7	3.48
8	3.70
9	3.89
10	4.05

Table 5.18 Relative accuracies of SPOT-5 HRS DSM (test field 1).

Distance [m]	SZ Open [m]	SZ Forest [m]	SZ whole area [m]
30	1.33	1.95	1.33
60	2.28	3.18	2.34
90	3.02	4.08	3.12
120	3.57	4.73	3.69
150	3.95	5.18	4.10
180	4.22	5.48	4.38
210	4.40	5.69	4.58
240	4.53	5.84	4.72
270	4.63	5.95	4.82
300	4.70	6.03	4.90

Test Field 2

Table 5.19 shows the results of relative accuracy analysis for SPOT-5 HRS DSM against REFDEM 2 in test field 2 with the regular distance interval corresponding with reference DEM's grid spacing.

Table 5.19 Relative accuracies of SPOT-5 HRS DSM (test field 2).

Distance [m]	SZ General[m]
1	1.34
2	2.19
3	2.83
4	3.32
5	3.67
6	3.90
7	4.06
8	4.18
9	4.27
10	4.34

ASTER DSM

Test Field 1

Table 5.20 shows the results of relative accuracy analysis for ASTER DSM against REFDEM 1 in test field 1 separately for open, forest layers and the whole area with the regular distance interval corresponding with reference DSM's grid spacing.

Test Field 2

Table 5.21 shows the results of relative accuracy analysis for ASTER DSM against REFDEM 2 for test field 2 with the regular distance interval corresponding to reference DEM's grid spacing.

Table 5.20 Relative accuracies of ASTER DSM (test field 1).

Distance [m]	SZ Open [m]	SZ Forest [m]	SZ whole area [m]
30	1.86	2.51	1.84
60	3.02	3.89	3.05
90	3.79	4.76	3.86
120	4.32	5.30	4.41
150	4.66	5.62	4.77
180	4.89	5.80	4.99
210	5.04	5.91	5.14
240	5.16	6.00	5.25
270	5.25	6.07	5.33
300	5.32	6.13	5.41

Table 5.21 Relative accuracies of ASTER DSM (test field 2).

Distance [m]	SZ whole area [m]
1	1.80
2	2.82
3	3.56
4	4.11
5	4.51
6	4.77
7	4.93
8	5.05
9	5.13
10	5.18

5.3.2.2 Relative Accuracy Analysis of INSAR DSMs

SRTM C-Band DSM

Table 5.22 shows the results of relative accuracy analysis for SRTM C-band DSM against REFDEM 1 for test field 1 separately for open, forest layers and the whole area with the regular distance interval corresponding to reference DEM's grid spacing.

Test Field 1

Table 5.22 Relative accuracies of SRTM C-band DSM (test field 1).

Distance [m]	SZ Open [m]	SZ Forest [m]	SZ whole area [m]
30	3.04	3.82	3.14
60	3.70	4.56	3.83
90	3.97	4.84	4.11
120	4.12	5.00	4.27
150	4.20	5.08	4.37
180	4.26	5.13	4.43
210	4.32	5.15	4.50
240	4.32	5.13	4.51
270	4.35	5.20	4.54
300	4.37	5.20	4.56

Test Field 2

Table 5.23 shows the results of relative accuracy analysis for SRTM C-band DSM against REFDEM 2 for test field 2 with the regular distance interval corresponding to reference DSM's grid spacing.

Table 5.23 Relative accuracies of SRTM C-band DSM (test field 2).

Distance [m]	SZ Whole area [m]
1	2.33
2	2.93
3	3.24
4	3.35
5	3.46
6	3.46
7	3.54
8	3.59
9	3.68
10	3.76

TSX SM DSM

Test Field 1

Table 5.24 shows the results of relative accuracy analysis for TSX SM DSM against REFDEM 1 at the test field 1 separately for open, forest layers and whole area with the regular distance interval corresponding with reference DEM's grid spacing.

Test Field 2

Table 5.25 shows the results of relative accuracy analysis for TSX SM DSM against REFDEM 2 in test field 2 with the regular distance interval corresponding with reference DEM's grid spacing.

TSX SL DEM

As mentioned before, TSX SL height model covers only the area of test field 2 that's why the relative accuracies have been calculated just for this test field.

Table 5.24 Relative accuracies of TSX SM DSM (test field 1).

Distance [m]	SZ Open [m]	SZ Forest [m]	SZ whole area [m]
30	3.18	6.90	3.80
60	4.79	9.77	5.63
90	6.09	11.91	7.08
120	6.81	12.79	7.79
150	7.43	13.55	8.41
180	7.95	14.16	8.94
210	8.40	14.64	9.38
240	8.78	15.02	9.75
270	9.10	15.34	10.05
300	9.37	15.59	10.31

Table 5.25 Relative Accuracies of TSX SM DSM (test field 2).

Distance [m]	SZ whole area [m]
1	1.33
2	2.15
3	2.79
4	3.30
5	3.74
6	4.12
7	4.46
8	4.76
9	5.02
10	5.26

Test Field 2

Table 5.26 shows the results of relative accuracy analysis for TSX SL DSM against REFDEM 2 in test field 2 with the regular distance interval corresponding with reference DEM's grid spacing.

Table 5.26 Relative Accuracies of TSX SL DSM (test field 2).

Distance [m]	SZ whole area [m]
1	.69
2	.98
3	1.31
4	1.57
5	1.82
6	2.04
7	2.21
8	2.37
9	2.52
10	2.65

Table 5.27 gives an overview about the relative accuracy analysis for the whole area (all layers included) of test field 1.

Table 5.28 gives an overview about the relative accuracy analysis in test field 2.

It can be seen in Tables 5.27 and 5.28 that SRTM C-band and TSX SL DSMs have a better relative accuracy than the other height models. Opposite to the absolute accuracies (Table 5.15 and 5.16), the relative accuracies of TSX models are quite better. Especially the relative accuracy of TSX SL DSM is better than high resolution optical IKONOS, SPOT-5 HRS and ASTER models. Summarizing Table 5.28, it can be mentioned that the relative accuracy of InSAR models are better as for the optical height models. That means the interior integrity of SRTM and TSX models are powerful, limitations may be caused by phase unwrapping.

Table 5.27 Results of relative accuracy analysis [m] (test field 1).

Distance [m]	SPOT-5 HRS	ASTER	SRTM C	TSX SM
30	1.33	1.84	3.14	3.80
60	2.34	3.05	3.83	5.63
90	3.12	3.86	4.11	7.08
120	3.69	4.41	4.27	7.79
150	4.10	4.77	4.37	8.41
180	4.38	4.99	4.43	8.94
210	4.58	5.14	4.50	9.38
240	4.72	5.25	4.51	9.75
270	4.82	5.33	4.54	10.05
300	4.90	5.41	4.56	10.31

Table 5.28 Results of relative accuracy analysis [m] (test field 2).

Distance [m]	IKONOS	SPOT-5 HRS	ASTER	SRTM C	TSX SM	TSX SL
1	.98	1.16	1.58	2.55	1.33	.69
2	1.63	2.02	2.61	3.23	2.15	.98
3	2.14	2.70	3.36	3.54	2.79	1.31
4	2.57	3.22	3.92	3.72	3.30	1.57
5	2.92	3.60	4.33	3.82	3.74	1.82
6	3.23	3.87	4.62	3.88	4.12	2.04
7	3.48	4.07	4.83	3.94	4.46	2.21
8	3.70	4.21	4.99	4.00	4.76	2.37
9	3.89	4.31	5.12	4.06	5.02	2.52
10	4.05	4.39	5.21	4.11	5.26	2.65

5.4 INFLUENCE OF INTERPOLATION

For the accuracy analysis in DEMANAL, the height values of the file for analysis corresponding to the point locations in the reference file are computed by bilinear interpolation. Under operational conditions the height models have to be interpolated for achieving the height values at the required positions. The interpolation always causes a loss of accuracy depending upon the grid spacing and the terrain roughness. It is performed point by point that's why the accuracies of the models which have large grid spacing are strongly influenced.

To determine the loss of accuracy caused by the interpolation, two different methods have been used. At first, all evaluated models have been interpolated into half of their original grid spacing and they are analyzed against the reference height models. Table 5.29 and 5.30 show the influence of interpolation for test field 1 and 2.

Table 5.29 Influence of interpolation (test field 1).

DSM	SZ before Interpolation [m]	SZ after Interpolation [m]	Relation of accuracy for whole area and slope 0°
SPOT-5 HRS Original spacing 20m	$4.88+5.73\times\tan(\alpha)$	$4.90+3.11\times\tan(\alpha)$	4.90/4.88 **1.01**
ASTER Original spacing 30m	$5.61+6.91\times\tan(\alpha)$	$5.64+7.00\times\tan(\alpha)$	5.64/5.61 **1.01**
SRTM C Original spacing 70m	$3.38+8.11\times\tan(\alpha)$	$3.56+11.91\times\tan(\alpha)$	3.56/3.38 **1.05**
TSX SM Original spacing 10m	$14.98+11.89\times\tan(\alpha)$	$14.99+11.79\times\tan(\alpha)$	14.99/14.98 **1.01**

Table 5.30 Influence of interpolation (test field 2).

DEM	SZ before Interpolation [m]	SZ after Interpolation [m]	Relation of accuracy for whole area and slope 0°
IKONOS Original spacing 3m	7.02+1.12×tan(α)	7.02+1.04×tan(α)	7.02/7.02 **1.00**
SPOT-5 HRS Original spacing 20m	5.05+0.14×tan(α)	5.58+3.87×tan(α)	5.58/5.05 **1.11**
ASTER Original spacing 30m	4.75+8.98×tan(α)	5.16+14.60×tan(α)	5.16/4.75 **1.09**
SRTM C Original spacing 70m	2.61+12.98×tan(α)	5.46+5.57×tan(α)	5.46/2.61 **2.09**
TSX SM Original spacing 10m	10.51+17.93×tan(α)	10.62+18.76×tan(α)	10.62/10.51 **1.01**
TSX SL Original spacing 3m	7.09+10.90×tan(α)	6.98+8.27×tan(α)	6.98/7.09 **0.99**

It is obvious from Table 5.29 that in relation to the reference DEM with 30m spacing only a limited influence of the interpolation can be seen. This is different for Table 5.30 where a clear influence of the interpolation can be seen in relation to the reference DEM with 1m grid spacing. While the IKONOS, TSX SM and TSX SL height models which have smaller grid spacing are not so much influenced by the interpolation, the accuracies of SPOT-5 HRS and ASTER DEMs are effected by 10% and the SRTM C-band DEM which has the largest grid spacing is effected by 100%.

The loss of accuracy by the interpolation can be analyzed also with program ZANAL. This is the second method which was used to determine the interpolation influence. Program ZANAL allows the interpolation over a multiplication of the spacing and a comparison of the interpolated value against the corresponding original height value. By this program the evaluated height model can be divided into sub-windows (2 by 2, 3 by 3 etc.) and can be analyzed separately to show the dependency upon varying terrain roughness.

In ZANAL, information about the tilt and change of tilt can be achieved and three interpolation methods are used for the calculations. These are linear, bilinear and polynomial interpolation techniques. In this study, because of the complex topography (flat, hilly, forest, etc.) of the Istanbul test field a linear (for nearly flat topography) and a bilinear interpolation (for rolling topography) have been used.

In addition, using the factor for the spacing of interpolation in ZANAL the effect of interpolation investigations are based on the hypothesis that the loss of accuracy depends upon the square of the spacing. Figure 5.54 represents the base for this hypothesis, which is correct if the terrain has a constant curvature.

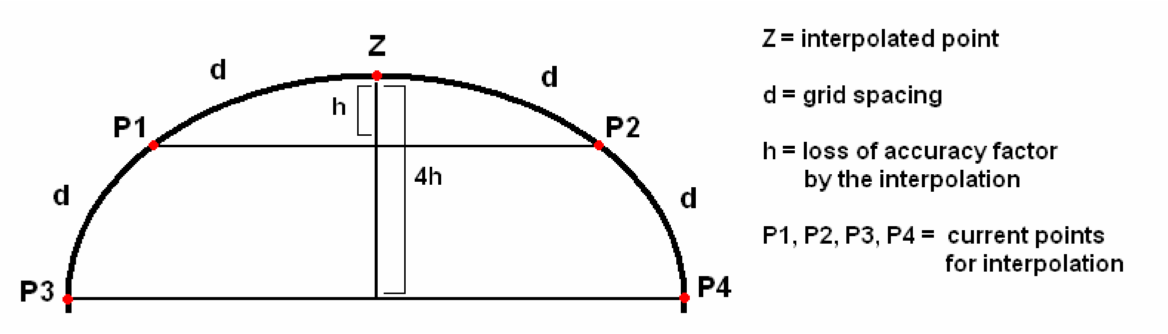

Figure 5.54 Base of hypothesis for loss of accuracy by the interpolation.

An estimation of the loss of accuracy by the interpolation is possible based on this hypothesis and to check the reliability of it the analysis were performed with ZANAL using factor for check of interpolation 2 and 4 separately.

At first the number of sub-windows is in X and Y direction was selected as 2 by 2 (4 sub-windows), the factor for check of interpolation is chosen as 2 (2×(2×3m)=12m) and the Z-tolerance is preferred as 50m. Figure 5.55 shows the sub-windows of TSX SL DSM.

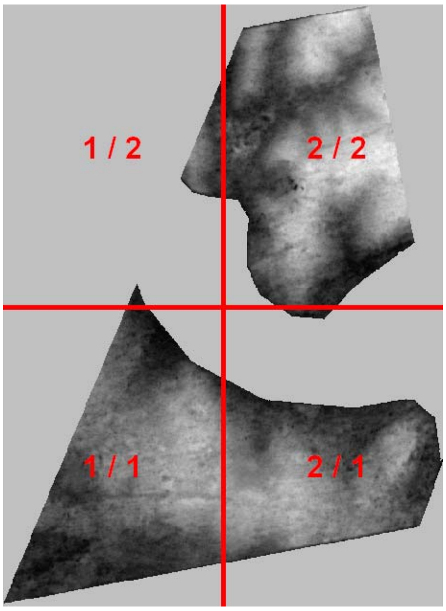

Figure 5.55 Sub-windows of TSX SL DSM used for interpolation analysis.

For the analysis in test field 2, a linear interpolation was used because of nearly flat topography. Table 5.31 shows the results of the linear interpolation.

Table 5.31 Accuracy loss by linear interpolation of TSX SL DSM over a distance of 12m.

Sub-window	Elevations [m]	X direction		Y direction	
		RMS of diff. [m]	Linear mean of diff. [m]	RMS of diff. [m]	Linear mean of diff. [m]
1/1	-7.4 - 85.6	1.58	1.15	1.65	1.22
1/2	-5.5 – 63.0	0.89	0.36	0.93	0.38
2/1	-7.4 – 83.3	1.26	0.73	1.31	0.77
2/2	-7.6 – 109.0	1.53	1.09	1.60	1.16

As can be seen, the influence of interpolation is nearly the same for all sub-windows. Just the results of sub-window 1/2 are below the others due to more smooth terrain.

As second investigation, all processing values are the same except the distance of interpolation. It was increased up to 24m for checking the loss of accuracy by interpolation. Table 5.32 shows the results of second analysis.

Table 5.32 Accuracy loss by linear interpolation of TSX SL DSM over a distance of 24m.

Sub-window	Elevations [m]	X direction		Y direction	
		RMS of diff. [m]	Linear mean of diff. [m]	RMS of diff. [m]	Linear mean of diff. [m]
1/1	-7.4 - 85.6	2.60	1.94	2.80	2.14
1/2	-5.5 – 63.0	1.46	0.60	1.56	0.66
2/1	-7.4 – 83.3	2.14	1.28	2.29	1.40
2/2	-7.6 – 109.0	2.56	1.88	2.78	2.05

Comparing Tables 5.31 and 5.32, it can be stated that the influence of interpolation and corresponding loss of accuracy are directly proportional with the spacing of interpolation in the nearly flat areas.

The test field 1 includes different terrain types, mainly rolling topography. The TSX SM DSM data set has been used for the analysis of the accuracy loss by interpolation. Different from the analysis in test field 2, a bilinear interpolation is preferred for the analysis in test field 1 because of its rough topographic characteristics. The bilinear interpolation is based on the linear interpolation between the 4 corner points of the patch. Figure 5.56 shows the sub-windows of TSX SM DSM.

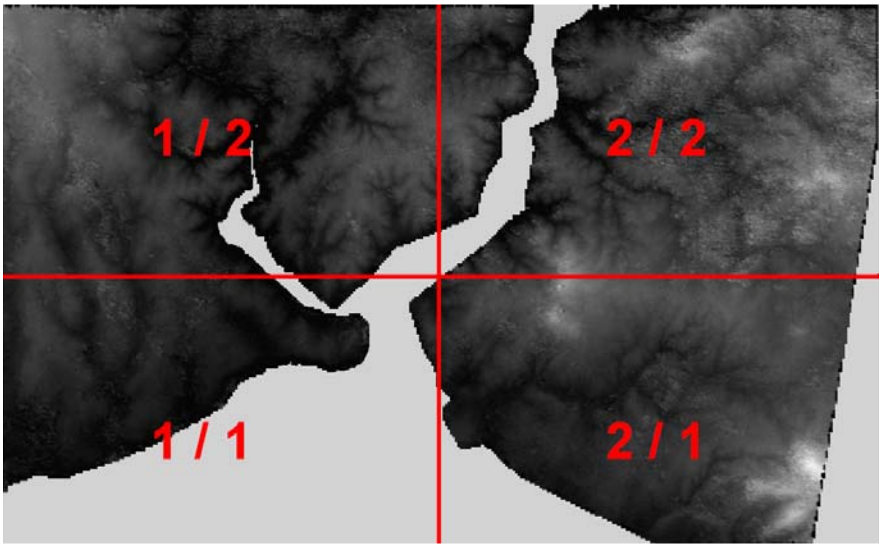

Figure 5.56 Sub-windows of TSX SM DSM used for interpolation analysis.

Table 5.33 Accuracy loss by bilinear interpolation of TSX SM DSM over a distance of 40m

Sub-window	Elevations [m]	RMS of diff. [m]	Linear mean of diff. [m]
1/1	-2.0 – 202.9	5.09	3.04
1/2	-3.1 – 312.3	6.57	3.86
2/1	-4.4 – 439.3	5.81	3.44
2/2	-3.8 – 387.5	11.42	7.39

As can be seen in Table 5.33, the largest influence of interpolation is in part 2/2, dominated by forest. It seems that the TSX SM height model shows some roughness in the forest located on mountainous area.

In second analyses, all processing values are same except the factor for check of interpolation. It was increased up to 4 (4×(2×10m)=80m). Table 5.34 shows the results of second analyses.

Table 5.34 Accuracy loss by bilinear interpolation of TSX SM DSM over a distance of 80m.

Sub-window	Elevations [m]	RMS of diff. [m]	Linear mean of diff. [m]
1/1	-2.0 – 202.9	7.45	4.72
1/2	-3.1 – 312.3	9.40	5.95
2/1	-4.4 – 439.3	8.30	5.24
2/2	-3.8 – 387.5	15.85	10.72

In general the loss of accuracy caused by interpolation, shown above is not negligible. The influence of interpolation based on 3m gridded TSX SL DSM is approximately three times smaller as for the 10m gridded TSX SM DSM.

5.5 MORPHOLOGY

The morphologic detail information analysis is one the main steps of the evaluation of an elevation model. This analysis is another way to understand the relative accuracy of a height model. Base of this application is the check of contour lines from the evaluated height models. Several factors have a strong influence on the morphologic analysis; the most important factor is the grid spacing. If the grid spacing of a height model is larger, fewer points can be used for the generation of contour lines, causing more smooth lines. Figure 5.57 represents the influence of grid spacing to the shape of contour lines.

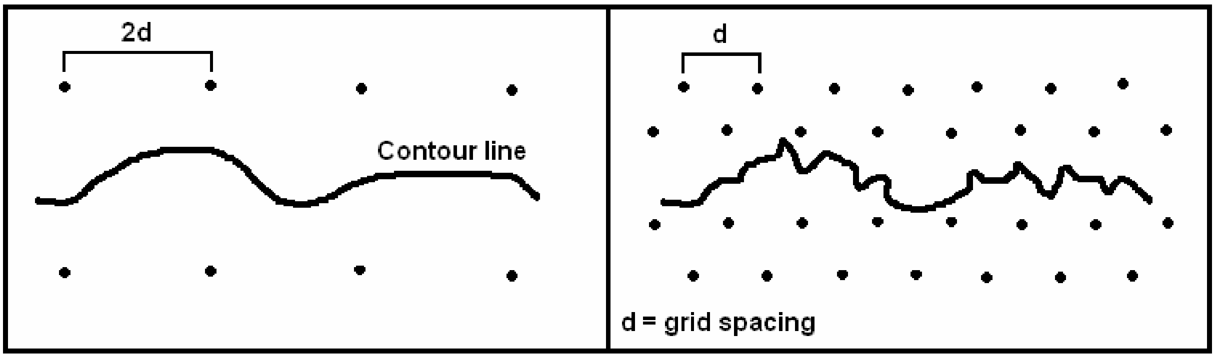

Figure 5.57 Influence of grid spacing to the shape of a contour line.

Another important factor is the noise of the height model. If the inspected elevation models are noisy, small contour-line islands can be seen and the morphologic details are disturbed.

For the morphologic detail information analysis any visualization program which enables contour line generation from a height model can be used. In this study, program LISA has been used. An equidistance of 20m was used for all evaluated models. Test field 2 has been used for the analysis because this area is typical for all evaluated height models.

The morphologic analysis of evaluated data sets in test field 2 is shown for each height model in following sections.

5.5.1 IKONOS

Figure 5.58 shows the contour lines derived from IKONOS 3m DSM.

Figure 5.58 Contour lines of IKONOS DSM in test field 2, 20m contour interval.

5.5.2 SPOT-5 HRS

Figure 5.59 shows the contour lines derived from SPOT-5 HRS 20m DSM.

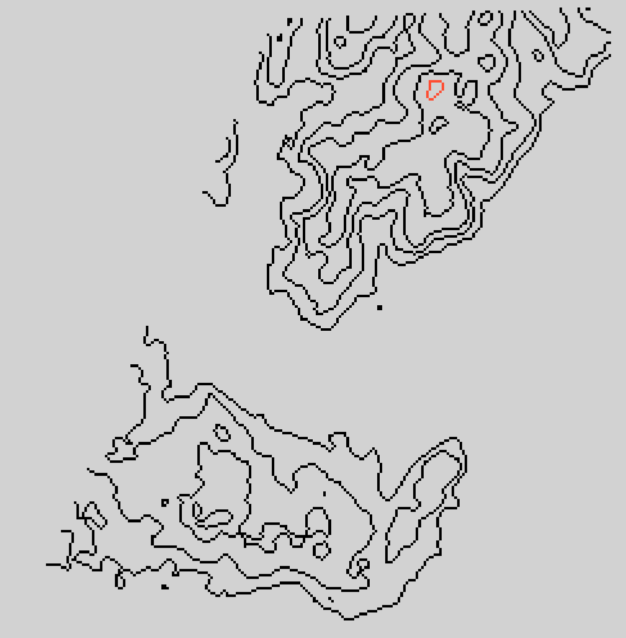

Figure 5.59 Contour lines of SPOT-5 HRS DSM in test field 2, 20m contour interval.

5.5.3 ASTER

Figure 5.60 represents the contour lines derived from ASTER 30m DSM.

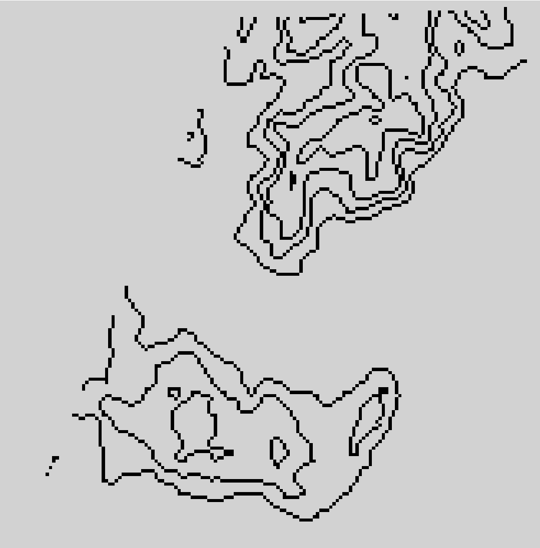

Figure 5.60 Contour lines of ASTER DSM in test field 2, 20m contour interval.

5.5.4 SRTM C-Band

Figure 5.61 shows the contour lines derived from SRTM C-band 70m DEM.

Figure 5.61 Contour lines of SRTM C-band DSM in test field 2, 20m contour interval.

5.5.5 TSX SM

Figure 5.62 shows the contour lines derived from TSX SM 10m DSM.

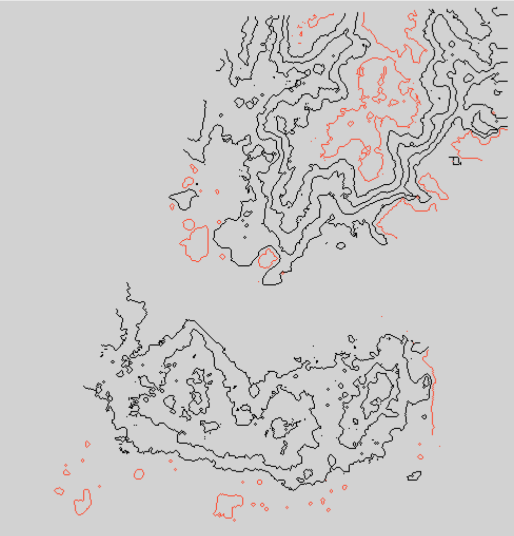

Figure 5.62 Contour lines of TSX SM DSM in test field 2, 20m contour interval.

5.5.6 TSX SL

Figure 5.63 shows the contour lines derived from TSX SL 3m DSM.

Figure 5.63 Contour lines of TSX SL DSM in test field 2, 20m contour interval.

The Figure 5.64 presents a general view to all evaluated models for better comparison.

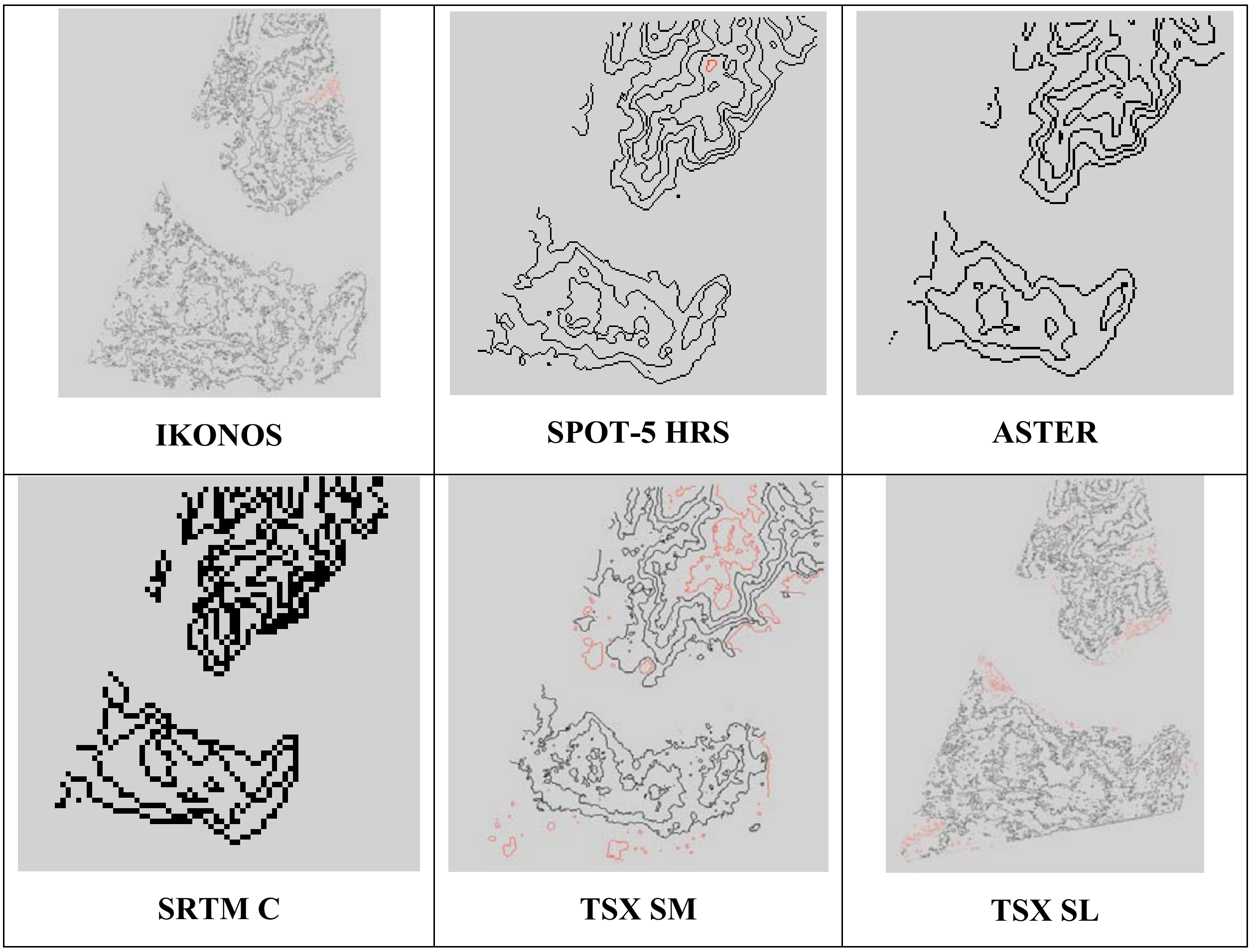
IKONOS SPOT-5 HRS ASTER

SRTM C TSX SM TSX SL

Figure 5.64 General results of morphologic analysis, 20m contour interval.

As a summary of Figure 5.64, the followings can be stated:

- Because of approximately 70m grid spacing, SRTM C-band does not include morphologic details.
- Contour lines are more detailed, but also noisy for TSX SL, IKONOS and TSX SM because of 3m and 10m grid spacing and the better relative accuracy.
- Beside included details and noisy structure of contour lines, TSX SL, TSX SM and IKONOS DSMs have several small contour islands. This may be caused by buildings, which cannot be included in the case of larger point spacing.
- SPOT-5 HRS has more details as ASTER, but ASTER which again can be explained by the different point spacing and the pixel size of the used sensor.

5.6 THE DIFFERENTIAL DEMs

Here differences between height models (DIFFDEMs) have been created for visualization. Differences of the DSMs to the reference DEM underline the character of the height models. It allows the interpretation of the error sources as forest, buildings, steep topography and may be the base for further applications of the height models. In following sections, the generated DIFFDEMs derived from the height differences between evaluated models and reference models can be seen for test field 1 for SPOT-5 HRS, ASTER, SRTM C-band, TSX SM and in test field 2 for IKONOS and TSX SL.

During the generation of three dimensional DIFFDEMs with program LISA, a view direction of 160º (0= North, 90= East) and an inclination angle of 35º was chosen for all DIFFDEMs. An exaggeration factor of 20 was used for test field 1 and 5 for test field 2 to provide an optimal visibility of the differences.

5.6.1 IKONOS

Figure 5.65 shows the DIFFDEM between IKONOS DSM and REFDEM 2.

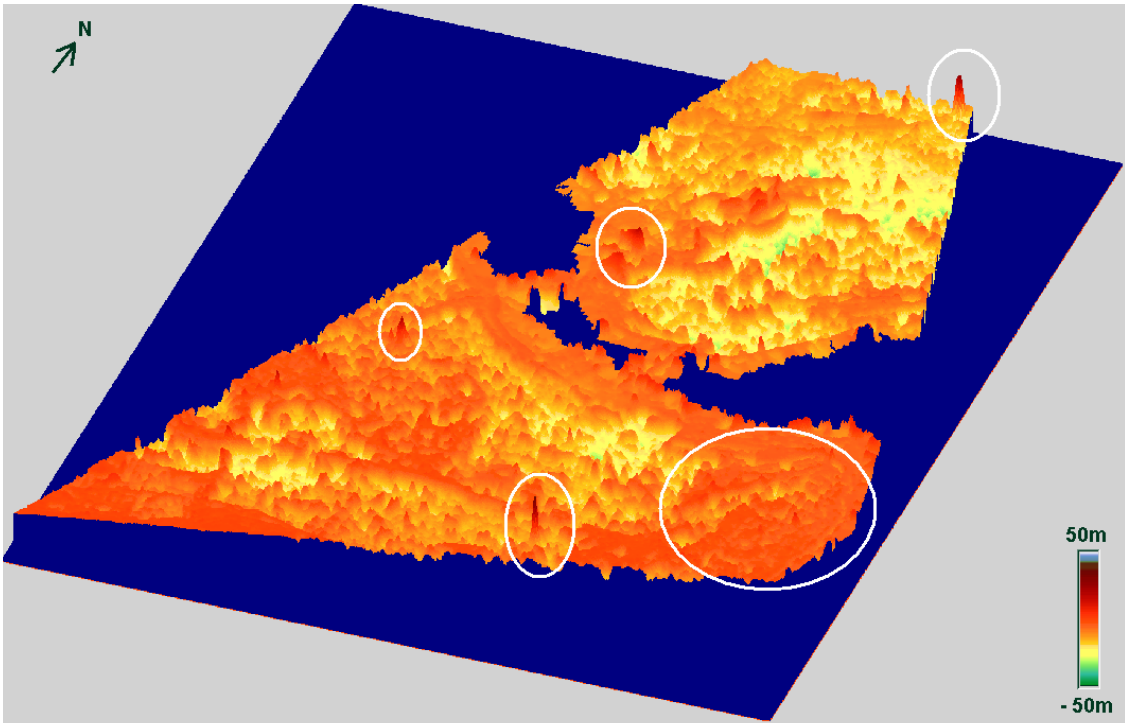

Figure 5.65 DIFFDEM between IKONOS DSM and REFDEM 2.

As can be seen in Figure 5.4 at the east tip of Historical Peninsula near the intersection of Golden Horn and Bosporus, there is a region with several trees highlighted by the large white circle in Figure 5.65. The forest regions are one of the main problems in DSM generation based on stereo optical imagery due to the lack of matching points. Especially in SPOT images, mainly limited to the visual spectrum, trees are always dark, while in the extended spectral range of IKONOS the reflection in the near infrared is included, as it is the case for ASTER, giving quite better image contrast. Test area 2 is dominated by densely building structures, causing differences of the DSMs against the reference DEM. With the exception of these problems, the IKONOS model is compatible with REFDEM 2. As mentioned before in section 4, while DEMs represent the bare ground, DSMs are defined by the top of the buildings and vegetation.

5.6.2 SPOT-5 HRS

Figure 5.66 shows the DIFFDEM between SPOT-5 HRS DSM and REFDEM 1.

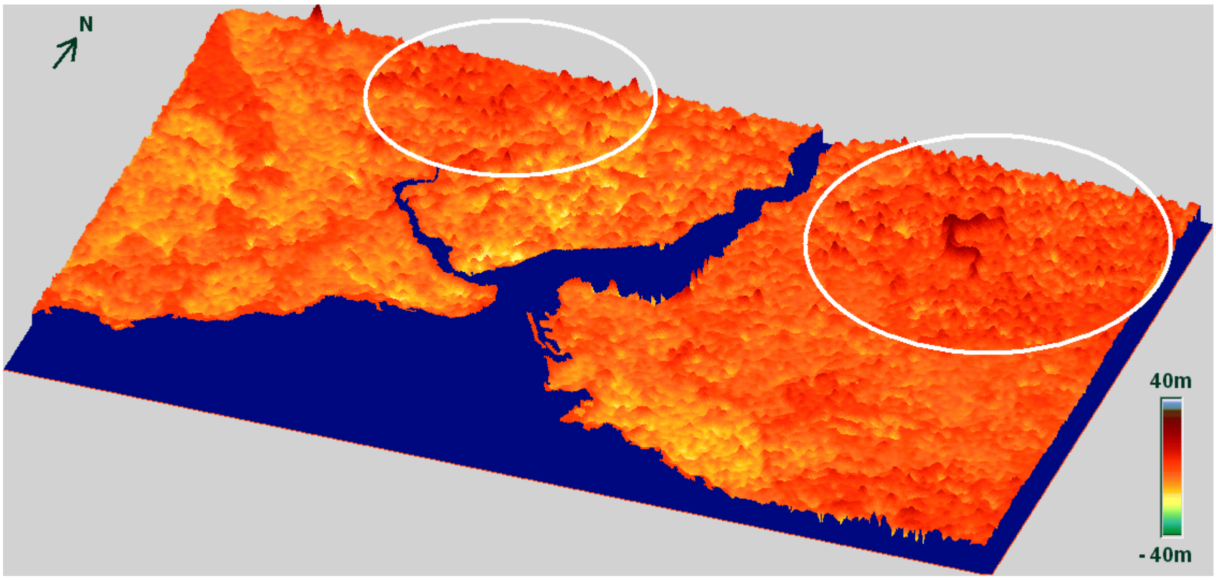

Figure 5.66 DIFFDEM between SPOT-5 HRS DSM and REFDEM 1.

As seen in Figure 5.66, larger height differences between SPOT-5 HRS DSM and REFDEM 1 are especially in forest areas but they are also caused in a smaller extend by buildings.

5.6.3 ASTER

Figure 5.67 shows the DIFFDEM between ASTER DSM and REFDEM 1.

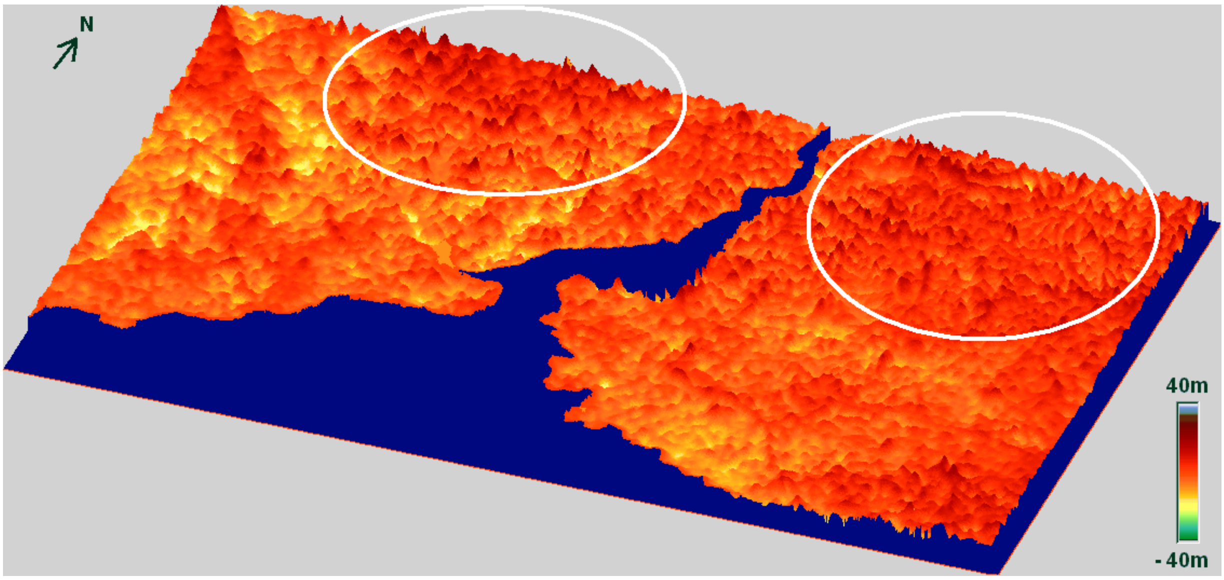

Figure 5.67 DIFFDEM between ASTER DSM and REFDEM 1.

As can been in the Figure 5.67, ASTER DSM has height differences against REFDEM 1 in similar areas as SPOT-5 HRS. Especially forest regions are influenced. With the exception of these regions, the height fits in a sufficient manner to REFDEM 1.

5.6.4 SRTM C-BAND

Figure 5.68 shows the DIFFDEM between SRTM C-band DSM and REFDEM 1.

As can be seen in Figure 5.68, SRTM C-band DEM has smaller height differences against the reference height model. The influence of the forest is not as obvious.

5.6.5 TSX SM

Figure 5.69 shows the DIFFDEM between TSX SM DSM and REFDEM 1.

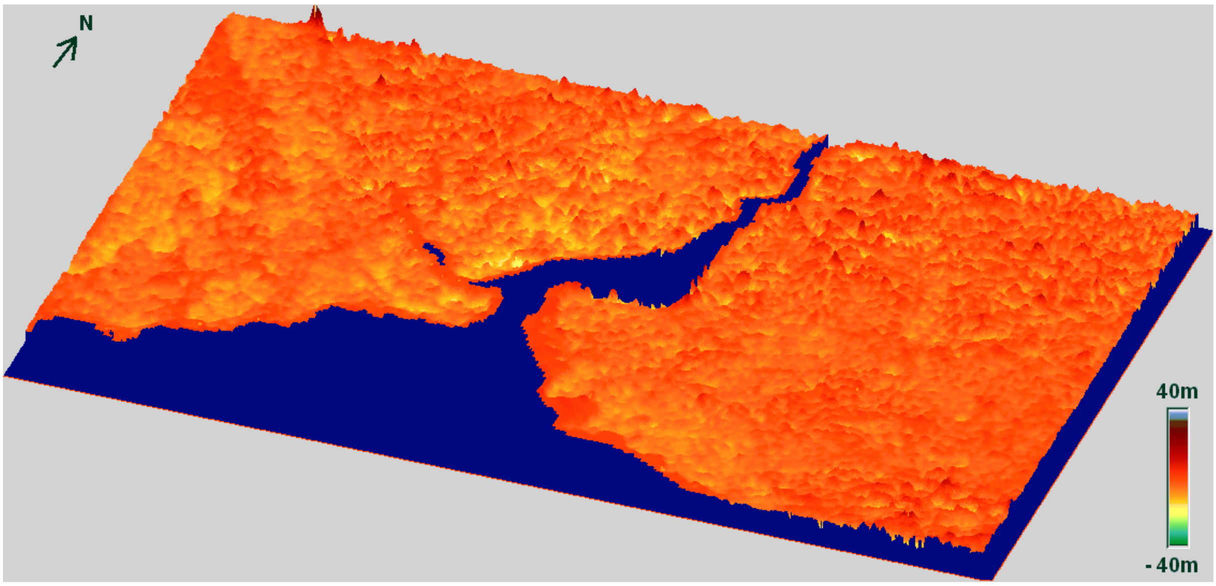

Figure 5.68 DIFFDEM between SRTM C-band DSM and REFDEM 1.

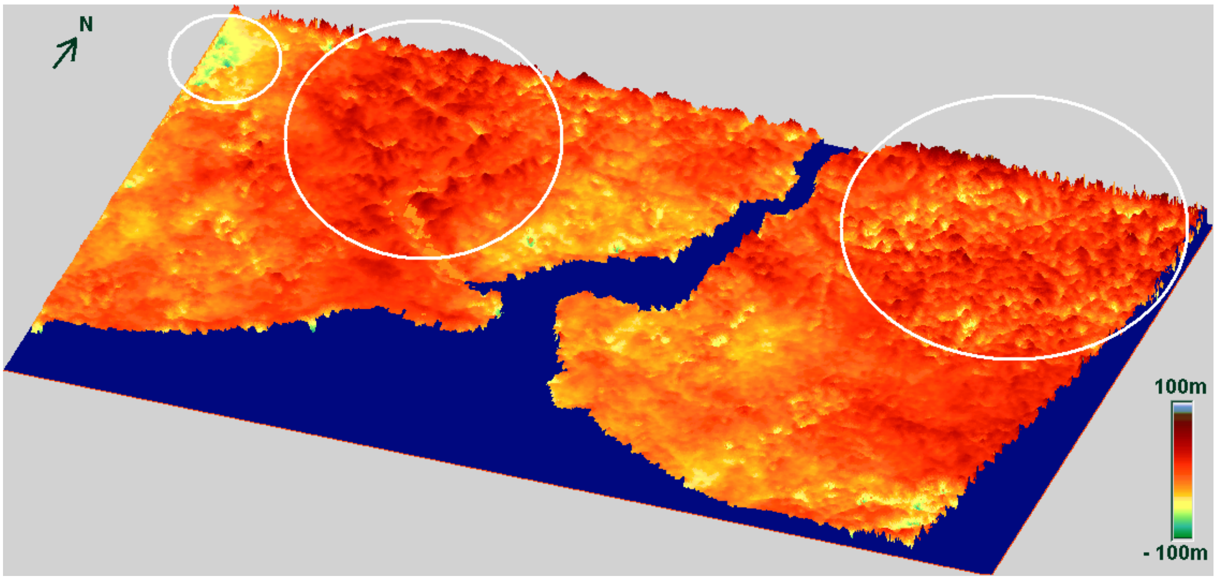

Figure 5.69 DIFFDEM between TSX SM DSM and REFDEM 1.

Similar as the other DIFFDEMs, TSX SM DSM has problems especially in steep and forest regions. Particularly, the areas highlighted by white circles have larger height differences against REFDEM 1 also caused by noise (seen also Figure 3.24).

5.6.6 TSX SL

Figure 5.70 shows the DIFFDEM between TSX SL DSM and REFDEM 2.

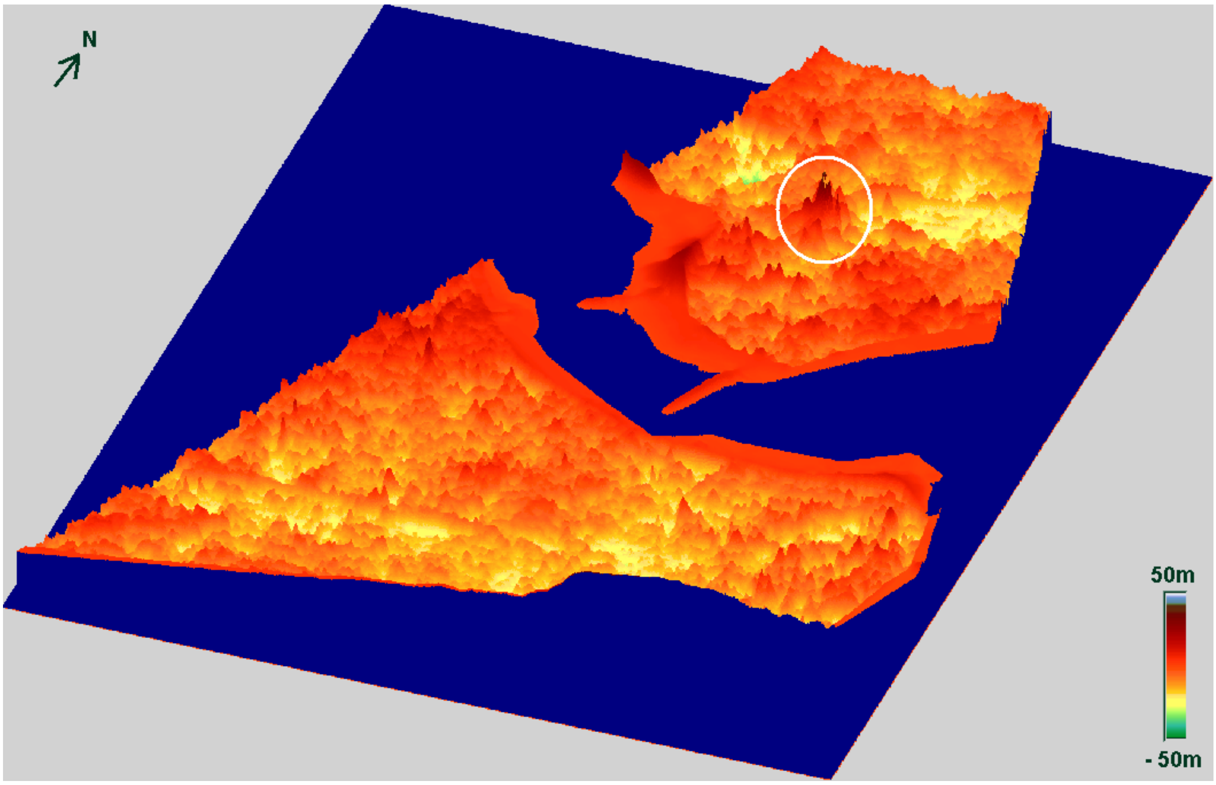

Figure 5.70 DIFFDEM between TSX SL DSM and REFDEM 2.

The influence of trees and buildings are obvious in the DIFFDEM between TSX SL DSM and REFDEM 2. As can be seen in Figure 5.70, except the encircled area, the DIFFDEM does not include large blunders against REFDEM 2. Similar with IKONOS, height differences exist in parts due to the comparison of a DSM with a DEM. In conclusion, it can be told that TSX SL DSM is reliable for several applications.

Figure 5.71 presents all DIFFDEMs between evaluated models and reference models for easier comparison.

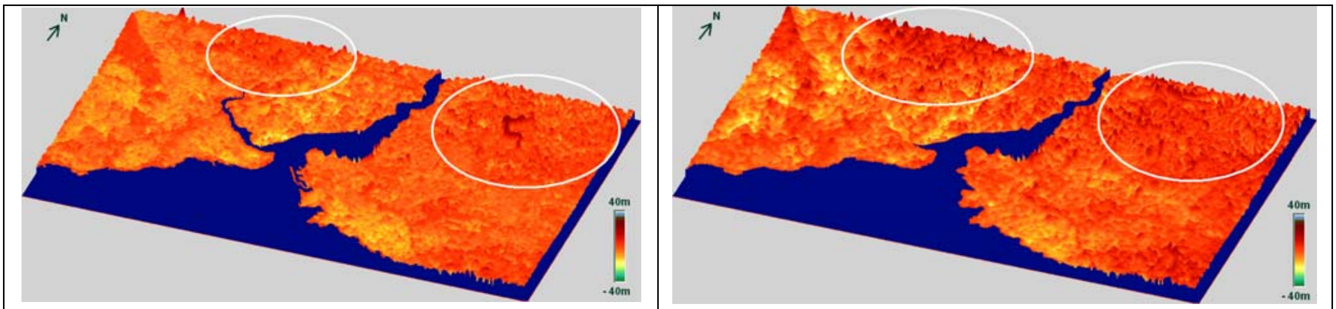

SPOT-5 HRS **ASTER**

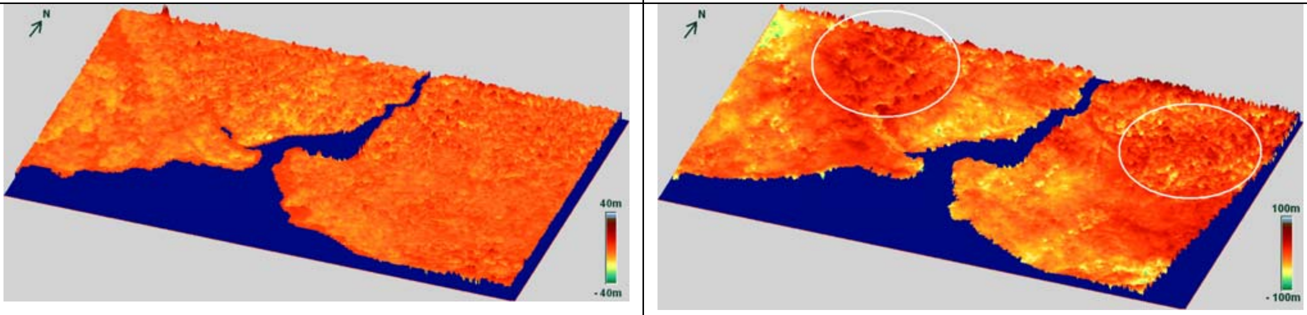

SRTM C-band **TSX SM**

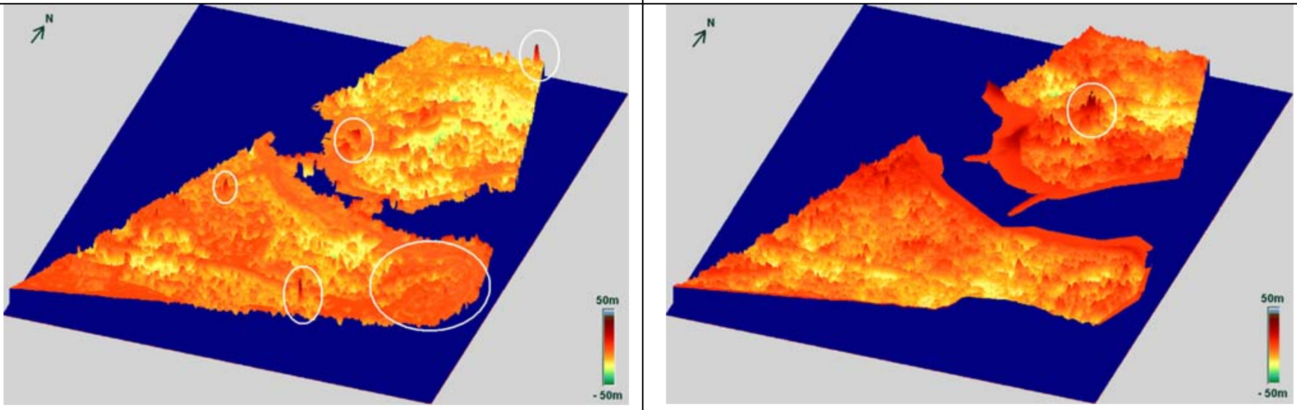

IKONOS **TSX SL**

Figure 5.71 DIFFDEMs between evaluated models and reference models.

5.7 SHADING

The shading is one of the best possibilities of visualizing a DSM. All buildings, vegetation and forest coverage in a DSM can be seen clearly. By this method, the shadings of IKONOS and TSX SL DSMs which have the same grid spacing (3m) have been generated and compared. At the three dimensional visualizations, shadings are generated using exaggeration factor 1 (no exaggeration).

5.7.1 IKONOS

Figures 5.72 and 5.73 show the shading of IKONOS DSM and three dimensional visualization.

Figure 5.72 Shading of IKONOS DSM.

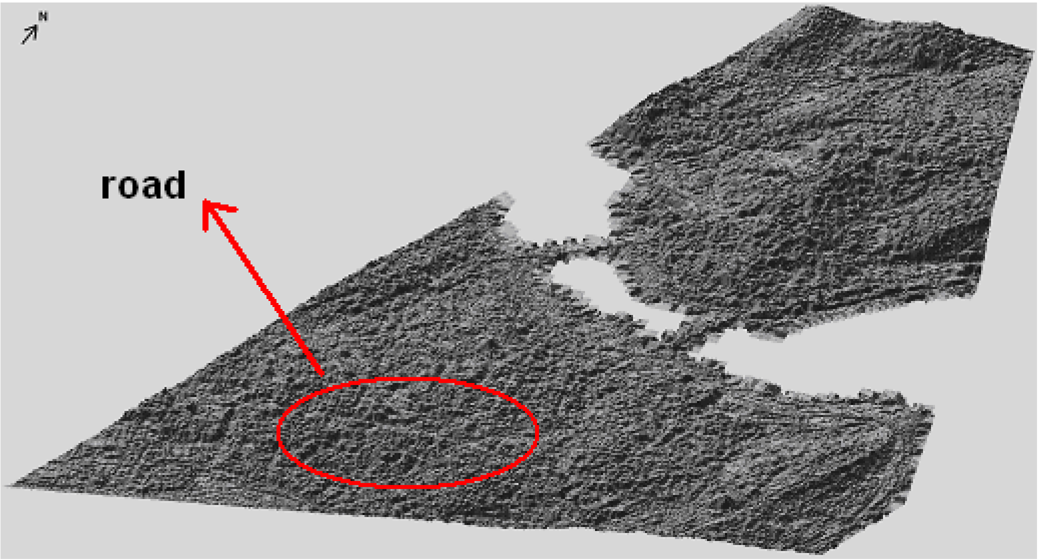

Figure 5.73 3D visualization of the shading (IKONOS DSM).

5.7.2 TSX SL

Figure 5.74 and 5.75 illustrate the shading of TSX SL DSM and three dimensional visualizations.

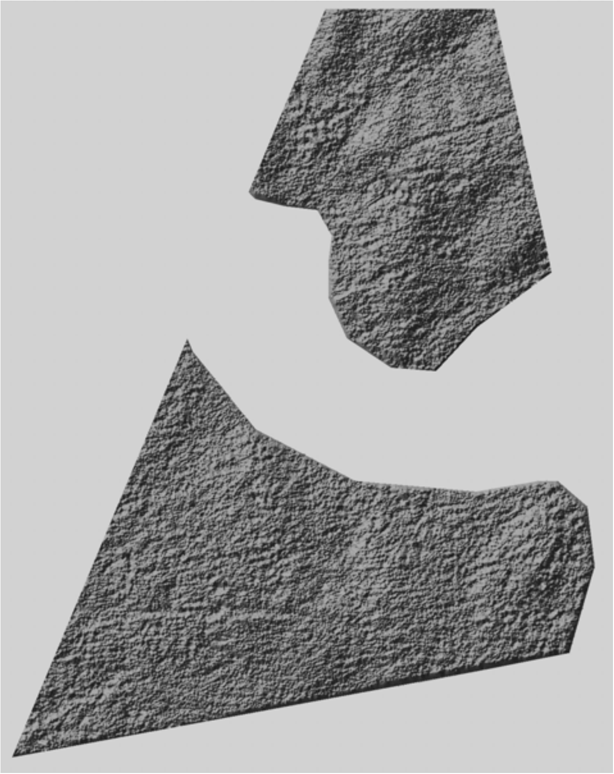

Figure 5.74 Shading of TSX SL DSM.

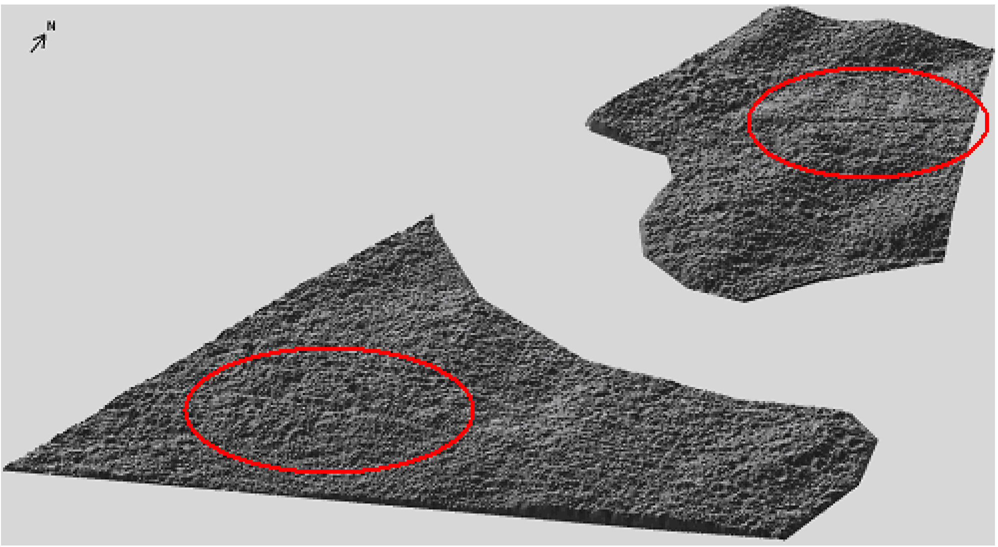

Figure 5.75 3D visualization of the shading (TSX SL DSM).

Looking at the results, it can be mentioned that the visualizations of both DSMs are pretty good. They clearly illustrate the ground objects like roads, buildings, vegetation and forest. In comparison with TSX SL DSM, the buildings are some more clearly in IKONOS DSM.

PART 6

CONCLUSION AND FUTURE TARGETS

In this investigation, two different modes SAR image-pairs of TerraSAR-X have been used for digital surface model generation in Istanbul test field, Turkey. These are Stripmap (3m) and the high resolution Spotlight (1m) mode image-pairs with respectively ~45m and ~135m baselines.

The length of baseline of the SAR-image-pair is the most important factor for TerraSAR-X digital surface models. A too short baseline is not leading to the required details and not enough to estimate the terrain topography. The digital surface model of TerraSAR-X Spotlight based on a longer baseline is 30% more accurate as TerraSAR-X Stripmap digital surface model. But also the resolution plays a significant role to the generation of height models by InSAR.

By InSAR and by matching optical images digital surface models are generated. In the densely build up area of Istanbul they are strongly influenced by buildings, partly also by trees and forest. The influence of the buildings and the vegetation cannot be filtered totally because of missing satisfying number of points on the ground. This is dominating the whole investigation, leading to quite higher values for the standard deviations of the height values as in open areas. Real open areas are more or less not available in both test fields, so the achieved accuracies are very pessimistic in relation to open areas.

InSAR height models have a clear dependency upon the aspects. Both surface models generated with TerraSAR-X InSAR images have a better relative accuracy as absolute accuracies, which may be explained by the influence of phase unwrapping, but also the case that digital surface models are compared with reference elevation models containing the height of the bare ground.

Loss of accuracy by the interpolation is in directly depending upon the grid spacing. TerraSAR-X Stripmap digital surface model is affected approximately three times more than TerraSAR-X Spotlight digital surface model because of three times larger grid spacing. It has been shown, that the not negligible influence of the interpolation enlarges nearly linear to the point spacing.

Morphologic details are available in both InSAR digital surface models.

It can be mentioned that the digital surface model, generated from the high resolution TerraSAR-X Spotlight image-pair which has suitable baseline length presents an absolute accuracy competitive to the height models based on the very high resolution optical images. A dominating effect of the accuracy is still the vegetation and buildings.

As a result of this study, it can be easily mentioned that digital surface models, derived by high resolution TerraSAR-X InSAR images are as useful as digital surface models, generated from high resolution optical images and they can be applied in several applications where high resolution optical digital elevation models are used.

Future investigations and development will be the digital elevation model fusion with optical digital elevation models based on space and/or aerial images. In this manner generation of best elevation models and support high resolution optical images for generation of maps 1/5000 scale and below. Another topic is the usage and analysis of TanDEM-X InSAR digital elevation models. And also the usage of these elevation models for disaster monitoring and management.

REFERENCES

Alobeid A, Jacobsen K and Heipke C (2009) Building Height Estimation in Urban Areas from Very High Resolution Satellite Stereo Images, *ISPRS Hannover Workshop,* 2-5 June, Hannover, Germany

Appiani E, Corvi M, Garibotto G and Coelho C (1996) Lecture Notes In Computer Science, Vol. 1124 archive, *Proceedings of the Second International Euro-Par Conference on Parallel Processing*-Volume II table of contents Pages: 139 – 146, 1996, ISBN 3-540-61627-6

Baldi A (2003) Phase Unwrapping by Region Growing, *Applied Optics*, Vol. 42, Issue 14, pp. 2498-2505

Baran I, Stewart M K, Kampes B M, Perski Z and Lilly P (2003) A Modification to the Goldstein Radar Interferogram Fitler, *IEEE Transactions on Geoscience and Remote Sensing*, Vol. 41, No. 9

Baudoin A, Schroeder M, Valorge C, Bernard M and Rudowski V (2003) The HRS SAP initiative: A scientific assessment of the High Resolution Stereoscopic instrument on board of SPOT 5 by ISPRS investigators, *ISPRS Hannover Workshop, High Resolution Mapping from Space,* Hannover, Germany

Colwell R N (1997) History and Place of Photographic Interpretation; in W.R. Philipson (ed.), *Manual of Photographic Interpretation 2nd ed.,* Bethesda, Maryland: American Society for Photogrammetry and Remote Sensing, pp. 3-47

Coulson S N (1993) SAR interferometry with ERS-1, *Earth Observation Quarterly*, no: 40, pp. 20-23

REFERENCES (continued)

Eineder M, Runge H, Boerner E, Bamler R, Adam N, Schättler B, Breit H and Suchandt S (2003) SAR Interferometry with TerraSAR-X, *Proceedings of the FRINGE 2003 Workshop* (ESA SP-550), 1-5 December, ESAESRIN, Frascati, Italy

Frei U, Graf K C and Meier E (1993) Cartographic reference systems, In Schreier, G. (ed.) *SAR Geocoding: Data and Systems*, (Karlsruhe:Wichmann), pp. 213-234

Gens R (1998) Quality Assessment of SAR Interferometric Data, *Ph.D Thesis (unpublished)* Hannover, ISSN 0174 1454

Guarnieri A M, Guccione P, Pasquali P and Desnos Y L (2003) Multi-mode ENVISAT ASAR Interferometry: Techniques and Preliminary Results, *IEE Proceedings: Radar, Sonar and Navigation,* vol. 150, no. 3, pp. 193–200

Hanssen R F (2001) *Radar Interferometry, Data Interpretation and Error Analysis*, Delft University of Technology, Delft, ISBN 0-7923-6945-9

Hofmann B and Moritz H (2006) *Physical Geodesy 2nd Revised edition*, Springer Verlag GmbH, Technical University Graz, Austria, ISBN-10: 3211335447

Jacobsen K (2003) DEM Generation from Satellite Data, *EARSeL Workshop*, 5-7 June, Ghent, Belgium, pp. 273-276

Jacobsen K (2004, 2005, 2006) *User Manual (unpublished)*, Program system BLUH, Institute of Photogrammetry and GeoInformation, Leibniz University Hannover, Germany

Jacobsen K (2008) 3D-Remote Sensing, Status Report 2008, 28th EARSeL Symposium: Remote Sensing for a Changing Europe, 2-5 June, Istanbul, Turkey

Leberl F W (1989) *Radargrammetric Image Processing*, Boulder Colorado, ISBN 0 89006-273-0

REFERENCES (continued)

Li Z, Zhu Q and Gold C (2005) *Digital Terrain Modelling: Principles and Methodology*, ISBN 0-415-32462-9

Lin Q, Vesecky J F and Zebker H A (1994) Comparison of elevation derived from InSAR data with DEM over large relief terrain, *International Journal of Remote Sensing*, 15, 1775-1790

Maune D F (2001) *Digital Elevation Model Technologies and Applications: The DEM Users Manual,* American Society for Photogrammetry and Remote Sensing, Bethesda, Maryland, America, ISBN 1-57083-064-9

Michalis P and Dowman I (2004) A Rigorous Model and DEM Generation for SPOT-5 RS, *ISPRS Congress*, Istanbul, Turkey

Parcharidis I, Foumelis M and Lekkas E (2005) Implication of Secondary Geodynamic Phenomena on Co-seismic Interferometric Coherence, Advances in SAR interferometry from ENVISAT and ERS missions, *ESA ESRIN*, 28 November-2 December, Frascati, Italy

Reigber A and Moreira J (1997) Phase Unwrapping by Fusion of Local and Global Methods, Geoscience and Remote Sensing, 1997, IGARSS '97 ,Singapur 3-8th August, pp. 869-871, Remote Sensing- *A Scientific Vision for Sustainable Development 1997 IEEE International*

Roth A (2003) TerraSAR-X: A new perspective for scientific use of high resolution spaceborne SAR data, *2nd GRSS/ISPRS Joint Workshop on "Data Fusion and Remote Sensing over Urban Areas*, 22-23 May, Berlin, Germany

Roth A (2004) TerraSAR-X Science Plan, *Doc.: TX-PGS-PL-4001*, Issue: 1.0, 25 November 2004, Germany

REFERENCES (continued)

Santitamnont P (1998) Interferometric SAR Processing for Topographic Mapping, *Master Thesis (unpublished),* Hannover, ISSN 0174-1454

Sarmap (2008) *The SAR Guidebook (unpublished),* SAR and SARscape, Sarmap, September

Schreier G (1993) *SAR Geocoding; Data and Systems*, Karlsruhe: Wichmann, ISBN 3 87907-247-7

Schwartz M L (2005) *Encyclopedia of Coastal Science,* Encyclopedia of Earth Sciences Series, Springer Netherlands, ISBN-13 978-1-4020-1903-6

Sefercik U G (2006) Accuracy Assessment of Digital Elevation Models Derived from Shuttle Radar Topography Mission (SRTM), Master Thesis (unpublished), Zonguldak, Turkey

Sefercik U G and Jacobsen K (2007) Quality Assessment of InSAR Digital Elevation Models, *27 EARSeL Symposium "Geoinformation in Europe"* 4-9 June, Bolzano, Italy

Soergel U (2010) *Review of Radar Remote Sensing on Urban Areas,* Springer Netherlands, ISBN 978-90-481-3750-3, ISSN 1567-3200, Volume 15, pp. 1-47

Sörgel U (2008) *Radar Remote Sensing Lecture Notes (unpublished),* Hannover, Germany

Torge W (1991) *Geodesy*, *2nd Edition*, pp. 264, Walter de Gruyter, Berlin New York

URL 1 (2009) http://sss.terrasar-x.dlr.de/, Proposals for TerraSAR-X, DLR, 10th February

URL 2 (2009) http://hyperphysics.phy-astr.gsu.edu , Electromagnetic Spectrum, Georgia State University, 15th February

URL 3 (2008) http://www.dlr.de/, German Aerospace Center (DLR), November

REFERENCES (continued)

URL 4 (2009) http://www.esa.int/esaCP/index.html, Europen Space Agency, 15th March

URL 5 (2009) http://mtp.jpl.nasa.gov/index.html, Microwave Temperature Profiler (MTP), NASA, 10th April

URL 6 (2009) http://www.noaa.gov/, National Oceanic and Atmospheric Administration (NOAA), 12nd April

URL 7 (2009) http://www.mdacorporation.com/corporate/index.cfm, Macdonald, Dettwiler and Associates Ltd. (MDA), 14th April

URL 8 (2009) http://www.jaxa.jp/projects/sat/jers1/index_e.html, Japan Aerospace Exploration Agency JAXA, Japan, 20th April

URL 9 (2009) http://www.itt.com/, International Telephone & Telegraph Visual Information Solutions (ITT-VIS), 5th May

URL 10 (2009) http://www.usgs.gov/, U.S. Geological Survey (USGS), 15th May

URL 11 (2009) http://www.cgrit.it/en/technology/lsa.html, Compagnia Generale Ripreseaeree S.p.A, 22nd May

URL 12 (2009) http://www.npagroup.com/, NPA Satellite Mapping, 15th June

URL 13 (2009) http://www.geoeye.com/CorpSite/, GeoEye, United States, 15th September

Wilson I J and Cocks T D (2003) Development of the Airborne Reflective Emissive Spectrometer (ARES) - a Progress Report, in Proc. of *3rd EARSeL Workshop on Imaging Spectroscopy* 13-16 May 2003, M. Habermeyer, A. Müller, and S. Holzwarth, eds., pp. 50–55, 2003.

Zebker H A, Werner C L, Rosen P A and Hensley S (1994b) Accuracy of topographic maps derived from ERS-1 interferometric radar, *IEEE Transactions on Geoscience and Remote Sensing*, 32, 823-836

APPENDICES A

LIST OF FORMULAS

LIST OF FORMULAS

LIST OF FORMULAS (continued)

LIST OF FORMULAS (continued)

LIST OF FORMULAS (continued)

LIST OF FORMULAS (continued)

AUTOBIOGRAPHY

Umut Güneş SEFERCİK was born in Zonguldak in 1981. He graduated from primary, secondary and high school in Zonguldak, Turkey. After graduating from Zonguldak Atatürk Science high school, he started to the Bachelor Science (B.Sc.) at Zonguldak Karaelmas University, Engineering Faculty, Department of Geodesy and Photogrammetry Engineering in 1999. He graduated from the department in 2003 and started to the Master Science Program at Zonguldak Karaelmas University Graduated School of Natural and Applied Sciences, Department of Geodesy and Photogrammetry Engineering in the same year. After lecture level he went to Leibniz University Hannover, Institute of Photogrammetry and GeoInformation, Hannover, Germany and prepared his M.Sc. Thesis with the supervision of –Ing. Dr. Karsten Jacobsen during 6 months. Then, he came back to Turkey and graduated from the department in 2006 and started to the PhD Program at the same department in the same year. After PhD lecture level, he went again to same Institute, Hannover, Germany and prepared his PhD Thesis with the supervision of –Ing. Prof. Dr. Uwe Sörgel during 9 months. Then, he came back again to Turkey and presently, he is still continuing his PhD at the same department.

INFORMATION OF ADDRESS

Address: Zonguldak Karaelmas University
Faculty of Engineering
Department of Geodesy and Photogrammetry Engineering
67100 ZONGULDAK / TURKEY

Tel: +90 (372) 2572996
Fax: +90 (372) 2574023
E-mail: ugsefercik@hotmail.com

Umut Güneş SEFERCİK